January 2015

THE EFFECT OF COMPACT OBJECT SPIN ON THE SEARCH FOR GRAVITATIONAL WAVES FROM BINARY NEUTRON STAR AND NEUTRON STAR-BLACK HOLE MERGERS

Alexander Harvey Nitz
Syracuse University

ABSTRACT

In this dissertation we study gravitational-wave searches for binary neutron star and neutron star - black hole coalescences. We determine the accuracy of post-Newtonian approximations as gravitational-wave templates in matched-filter based searches for NSBH mergers. We test a geometric method to generate template banks for BNS and NSBH mergers where the components have intrinsic spin, and estimate the sensitivity to astrophysical sources of searches that use these banks during Advanced LIGO. We explore simplifications and optimizations to the search pipeline used during S6/VSR2,3 gravitational-wave searches. We investigate methods for regenerating template banks as the noise behavior of a detector changes over time. We further investigate changes to the algorithm for determining coincidence between candidates from multiple-detectors. Finally, we develop a focused search for binary neutron stars, and test improvements to its configuration using LIGO detector data from the most recent science run.

THE EFFECT OF COMPACT OBJECT SPIN ON THE SEARCH FOR GRAVITATIONAL WAVES FROM BINARY NEUTRON STAR AND NEUTRON STAR–BLACK HOLE MERGERS

By

Alexander Harvey Nitz

Dissertation

Submitted in partial fulfillment of the requirements

for the degree of

Doctor of Philosophy in Physics

Syracuse University

August 2015

Acknowledgments

I've had the privilege over the past several years to work with numerous physicists, make friends, and build connections through my membership in the LIGO Scientific collaboration. To those that I fail to thank here, please know that I am appreciative, and that I intend no slight.

I would first like to express my deepest gratitude and thanks to my advisor, Duncan Brown. His broad knowledge of gravitational-wave astronomy and his exuberance have been an inspiration. I am indebted to him for his guidance, encouragement, and especially his patience.

I would also like to thank the members of my defense committee — Robert Moucha, Martin Forstner, Liviu Movilenau, Simon Catterall, and Mitchell Soderberg — for taking time out of their busy schedule to read and critique my work.

To the Syracuse University gravitational-wave faculty, Peter Saulson and Stefan Ballmer, I wold like to thank you both for allowing me to constantly pick your brains. Our conversations have been immensely valuable to me, and have broadened my understanding of the field.

For his mentorship, when I was a starting graduate student, I would also like to thank Ian Harry.

For always being willing to bounce ideas and putting up with me, I would like to thank my office mates Chris Biwer and Thomas Massinger.

I must all thank my parents for their guidance throughout my life.

I owe a special debt to Keith Riles for introducing me to LIGO, without whom, I would not have had the amazing experiences and challenges that come with working on the frontiers of gravitational-wave physics.

Contents

List of Tables

List of Figures

Preface

The work presented in this thesis is the result of my participation in the LIGO Scientific Collaboration (LSC) and does not reflect the scientific opinion of the LSC.

Chapter 4 is based on material from

D. A. Brown, I. Harry, A. Lundgren and A. H. Nitz, "Detecting binary neutron star systems with spin in advanced gravitational-wave detectors," *Phys. Rev. D* **86**, 084017 (2012)

Chapter 5 is based on material from

A. H. Nitz, A. Lundgren, D. A. Brown, E. Ochsner, D. Keppel and I. W. Harry, "Accuracy of gravitational waveform models for observing neutron-starblack-hole binaries in Advanced LIGO," *Phys. Rev. D* **88**, no. 12, 124039 (2013)

Chapter 6 is based on material from

I. W. Harry, A. H. Nitz, D. A. Brown, A. Lundgren, E. Ochsner and D. Keppel, "Investigating the effect of precession on searches for neutron-star-black-hole binaries with Advanced LIGO," *Phys. Rev. D* **89**, no. 2, 024010 (2014)

Chapter 7 is based on material from

D S. A. Usman *et al.*, "An improved pipeline to search for gravitational waves from compact binary coalescence," arXiv:1508.02357 [gr-qc]. (2015)

Chapter 1

Introduction

Proposed shortly after the discovery of General Relativity by Albert Einstein, gravitational-waves are ripples that propagate through the curvature of spacetime [1]. They travel at the speed of light and carry energy away from their source, however, since gravitational-waves only weakly couple with matter, their direct detection in the laboratory is challenging. The earliest indirect evidence for gravitational waves comes from the discovery by Hulse and Taylor of a pulsar in a binary system. Through the measurement of the pulsar's radio emissions, it was determined that the binary's orbit was decaying, and that the rate of decay was in agreement with energy being carried away by the emission of gravitational waves [2, 3].

As a gravitational-wave passes by, the distance measured between free falling objects changes. The first to suggest measuring this change in distance using light signals was Felix Pirani in 1956. By 1971 the first gravitational antenna using laser interferometry was developed and tested by Moss, Miller, and Forward [4]. The modern design of gravitational-wave interferometers is based on the work of Weiss and Drever in the 1970s [5, 6]. This has formed the basis for the construction of a world-wide network of ground-based gravitational-wave detectors. This includes the Laser Interferometer Gravitational-wave Observatory (LIGO), which has two independent detectors in Hanford, Washington and Livingston, Louisiana along with the Virgo detector in Cascina, Italy.

A prime target for these detectors is the detection of compact binary coalescences (CBCs). Compact objects such a neutron stars and black holes can spiral inwards to produce signals in the frequency band that ground-based interferometric

gravitational-wave detectors are most sensitive. Searches for gravitational waves from compact object binaries containing neutron stars and stellar-mass black holes have been performed using the first-generation LIGO and Virgo detectors in LIGO's six science runs (S1–S6) and three Virgo science runs (VSR1–VSR3) [7, 8, 9, 10, 11, 12, 13, 14, 15].

Construction of the Advanced LIGO (aLIGO) detectors [16] is now complete and the first aLIGO observing runs are scheduled for autumn 2015 [17]. The Advanced Virgo (AdV) detector [18] is scheduled to join this network in 2016. The second-generation gravitational-wave detectors Advanced LIGO (aLIGO) and Advanced Virgo (AdV) [19, 20] are expected to reach full sensitivity by 2018-19. These detectors will observe a volume of the universe more than a thousand times greater than first-generation detectors and establish the new field of gravitational-wave astronomy. Estimated detection rates for aLIGO and AdV suggest that binary neutron stars (BNS) will be the most numerous source detected, with plausible rates of $\sim 40/\mathrm{yr}$ [21]. Gravitational-wave observations of BNS systems will allow measurement of the properties of neutron stars and allow us to explore the processes of stellar evolution. Binaries containing a NSBH have a predicted coalescence rate of 0.2–300 yr^{-1} within the sensitive volume of aLIGO [21], making them another important source for these observatories. The observation of a NSBH by aLIGO would be the first conclusive detection of this class of compact-object binary. Gravitational-wave observations of NSBH binaries will allow us to explore the central engine of short, hard gamma-ray bursts, shed light on models of stellar evolution and core collapse, and investigate the dynamics of compact objects in the strong-field regime [22, 23, 24, 25, 26, 27, 28].

Gravitational waves from compact binary coalescence have three distinct phases: an *inspiral* consisting of a wave of slowly increasing amplitude and frequency, a *merger* which can be calculated using numerical simulations, and a *post-merger* signal as the binary stabilizes into a final state. If the total mass of the binary is lower than $M \lesssim 12\,M_\odot$ [29, 30] and the angular momenta of the compact objects (their *spin*) is small [31, 32] (as is the case for binary neutron stars), then the inspiral phase can be well modeled using the post-Newtonian approximations (see e.g. Ref. [33] for a review). For higher mass and higher-spin binaries, analytic models tuned to numerical relativity can provide accurate predictions for the gravitational waves from compact binaries [34, 35, 36, 37, 38].

The gravitational waves that advanced detectors will observe from inspiralling BNS systems are well described by post-Newtonian theory [39]. As the neutron stars orbit each other, they lose energy to gravitational waves causing them to spiral together and eventually merge. If the angular momentum (spin) of the component neutron stars is zero, the gravitational waveform emitted depends at leading order on the chirp mass of the binary $\mathcal{M} = (m_1 m_2)^{3/5} / (m_1 + m_2)^{1/5}$ [40], where m_1, m_2 are the component masses of the two neutron stars, and at higher order on the symmetric mass ratio $\eta = m_1 m_2/(m_1 + m_2)^2$ [41, 42, 43, 44, 45, 46].

Ground-based gravitational-wave detectors produce a calibrated strain signal $s(t)$, which is sensitive to gravitational waves incident on the detector's arms [47]. In addition to possible signals, the strain data contain two classes of noise: (i) a primarily stationary, Gaussian noise component from fundamental processes such as thermal noise, quantum noise, and seismic noise coupling into the detector; and (ii) non-Gaussian noise transients of instrumental and environmental origin. Since the gravitational-wave signal from compact binaries is well-modeled and the expected amplitude of astrophysical signals is comparable to the amplitude of the noise, matched filtering is used to search for signals in the detector data [48]. Since we do not *a priori* know the parameters of the compact binaries we may detect, a *bank* of template waveforms is constructed that spans the astrophysical signal space [49, 50, 51, 52, 53, 54, 55, 56, 57]. These banks are designed so that the loss in event rate caused by their discrete nature is typically no more than 10%. The exact placement of the templates depends on the noise power spectral density of the detector data. To mitigate the effect of the non-Gaussian noise transients in the search, we require that any signal be seen with consistent parameters (compact objects' spins and masses and the signal's time of arrival) in the detector network. Additional statistical tests are applied to mitigate the effect of non-Gaussian noise transients [58]; these are often called *signal-based vetoes*. The matched-filter signal-to-noise ratio and the additional statistical tests are used to create a numerical detection statistic for candidate signals. To assign a statistical significance to these detection candidates, the network's false-alarm rate is computed as a function of the detection statistic for the noise background.

We demonstrate in Ch. 4 that neglecting spin in matched-filter searches for binary neutron star mergers causes advanced detectors at final design sensitivity to lose more than 3% of the possible signal-to-noise ratio for 59% (6%) of sources, assuming that

neutron star dimensionless spins, $c\mathbf{J}/GM^2$, are uniformly distributed with magnitudes between 0 and 0.4 (0.05) and that the neutron stars have isotropically distributed spin orientations. We present a new method for constructing template banks for gravitational wave searches for systems with spin. We show that an aligned-spin BNS search using this bank loses only 3% of the maximium signal-to-noise for only 9% (0.2%) of BNS sources with dimensionless spins between 0 and 0.4 (0.05) and isotropic spin orientations. Use of this template bank will prevent selection bias in gravitational-wave searches and allow a more accurate exploration of the distribution of spins in binary neutron stars.

We investigate in Ch. 5 the ability of currently available post-Newtonian templates to model the gravitational waves emitted during the inspiral phase of neutron star–black hole binaries. We restrict to the case where the spin of the black hole is aligned with the orbital angular momentum and compare post-Newtonian approximants that differ in the expansion of energy and gravitational-wave flux. We examine restricted amplitude post-Newtonian waveforms that are accurate to third-and-a-half post-Newtonian order in the orbital dynamics and complete to second-and-a-half post-Newtonian order in the spin dynamics. We also consider post-Newtonian waveforms that include the recently derived third-and-a-half post-Newtonian order spin-orbit correction and the third post-Newtonian order spin-orbit tail correction. We compare these post-Newtonian approximants to the effective-one-body waveforms for spin-aligned binaries. For all of these waveform families, we find that there is a large disagreement between different waveform approximants starting at low to moderate black hole spins, particularly for binaries where the spin is anti-aligned with the orbital angular momentum. The match between the TaylorT4 and TaylorF2 approximants is ~ 0.8 for a binary with $m_{BH}/m_{NS} \sim 4$ and $\chi_{BH} = cJ_{BH}/Gm_{BH}^2 \sim 0.4$. We show that the divergence between the gravitational waveforms begins in the early inspiral at $v \sim 0.2$ for $\chi_{BH} \sim 0.4$. Post-Newtonian spin corrections beyond those currently known will be required for optimal detection searches and to measure the parameters of neutron star–black hole binaries. The strong dependence of the gravitational-wave signal on the spin dynamics will make it possible to extract significant astrophysical information from detected systems with Advanced LIGO and Advanced Virgo.

In Ch. 6 we demonstrate that if the effect of the black hole's angular momentum is neglected in the waveform models used in gravitational-wave searches, the detection

rate of $(10 + 1.4)M_\odot$ neutron-star–black-hole systems would be reduced by $33 - 37\%$. The error in this measurement is due to uncertainty in the Post-Newtonian approximations that are used to model the gravitational-wave signal of neutron-star–black-hole inspiralling binaries. We describe a new method for creating a bank of filter waveforms where the black hole has non-zero angular momentum that is aligned with the orbital angular momentum. With this bank we find that the detection rate of $(10+1.4)M_\odot$ neutron-star–black-hole systems would be reduced by $26-33\%$. Systems that will not be detected are ones where the precession of the orbital plane causes the gravitational-wave signal to match poorly with non-precessing filter waveforms. We identify the regions of parameter space where such systems occur and suggest methods for searching for highly precessing neutron-star–black-hole binaries.

In Ch. 7 we describe improvements made to the offline analysis pipeline searching for gravitational waves from stellar-mass compact binary coalescences, and assess how these improvements affect search sensitivity. Starting with the two-stage `ihope` pipeline used in S5, S6 and VSR1-3 and using two weeks of S6 data as test periods, we first demonstrate a pipeline with a simpler workflow. This *single-stage pipeline* performs matched filtering and coincidence testing only once. This simplification allows us to reach much lower false-alarm rates for loud candidate events. We then describe an optimized χ^2 test which minimizes computational cost. Next, we compare methods of generating template banks, demonstrating that a fixed bank may be used for extended stretches of time. Fixing the bank reduces the cost and complexity, compared to the previous method of regenerating a template bank every 2048 s of analyzed data. Creating a fixed bank shared by all detectors also allows us to apply a more stringent coincidence test, whose performance we quantify. With these improvements, we find a 10% increase in sensitive volume with a negligible change in computational cost. We describe additional computational improvements to the matched-filtering algorithm in Ch. 8.

Finally, in Ch. 9 we demonstrate an analysis pipeline that is focused on the detection of binary neutron star mergers. Using the improved single stage pipeline, we use three weeks of S6/VSR3 data to test further improvements to the pipeline. We describe a method for calculating the significance of candidate events, and measure probabilities under the assumption of both including and excluding foreground events

from a background. We investigate alternate configurations of the filtering process, including changes to the spectrum estimation and signal-consistency test. We find that the new configuration is able to achieve a 25% increase in sensitive volume over the single stage configuration proposed in Ch. 7. Lastly, we investigate using an aligned spin template bank, and show that for conservative estimates of BNS populations a non-spinning template bank has marginally superior sensitivity.

Chapter 2

Pipelines to Search for Gravitational-waves from Compact Binary Coalescences

2.1 Introduction

While the basic steps of a CBC gravitational-wave search pipeline remain the same, different choices can be made to create various configurations and topologies. The search pipelines used in the last joint LIGO-Virgo science run (S6/VSR2,3) used the `ihope` search pipeline to search for compact binaries [59]. The `ihope` pipeline, as well as the pipelines used in previous LIGO-Virgo searches [60, 61], are *offline* search pipelines. These pipelines analyze the data in a batch mode, processing of the order of one week of data from the network. Offline batch processing allows the pipeline to incorporate additional information about the quality of the detector data or search tuning that is not available in real time [62, 63], and to produces a systematic false-alarm rate estimation of candidates by using large samples of the noise background before and after the time of a signal. Batch processing also allows the pipeline to take advantage of the computationally efficient Fast Fourier Transform (FFT) when implementing matched filtering [48], and allows computational tasks to be parallelized over time and binary parameters for efficient implementation on large computing clusters [64].

2.2 Assessing Waveform and Template Bank Effectiveness

In the absence of non-Gaussian noise, we can create analytic measures of the faithfulness and effectiveness of the waveform models and template banks that will be used to search for gravitational waves. In this section we describe the methods and the terminology that we will use in the rest of this work.

The "overlap" between two gravitational waveforms h_1 and h_2 is defined as

$$\mathcal{O}(h_1, h_2) = (\hat{h}_1|\hat{h}_2) = \frac{(h_1|h_2)}{\sqrt{(h_1|h_1)(h_2|h_2)}}, \tag{2.1}$$

where (h_1, h_2) denotes the noise-weighted inner product

$$(h_1|h_2) = 4\,\mathrm{Re}\int_{f_{\min}}^{\infty} \frac{\tilde{h}_1(f)\tilde{h}_2^*(f)}{S_n(f)} df. \tag{2.2}$$

Here, $S_n(f)$ denotes the one sided power spectral density (PSD) of the noise in the interferometer, and f_min is a lower frequency cutoff determined by the characteristics of the noise [65].

Gravitational wave searches for binary mergers maximize over an overall phase and time shift, we define the "match" between two waveforms to be the overlap maximized over the phase and time shift

$$\mathcal{M}(h_1, h_2) = \max_{\phi_c, t_c}(\hat{h}_1|\hat{h}_2(\phi_c, t_c)). \tag{2.3}$$

One can understand this match as the fraction of the optimal signal-to-noise ratio (SNR) that would be recovered if a template h_1 was used to search for a signal h_2.

We define the "fitting-factor" between a waveform h_s with unknown parameters and a bank of templates h_b to be the maximum match between h_s and all the waveforms in the template bank [65],

$$\mathrm{FF}(h_s) = \max_{h \in \{h_b\}} \mathcal{M}(h_s, h). \tag{2.4}$$

The "mismatch"

$$\mathrm{MM} = 1 - \mathrm{FF}(h_s) \tag{2.5}$$

describes the fraction of SNR that is lost due to the fact that the template in the bank that best matches h_s will not match it exactly due to the discreteness of the bank and due to any disagreement between the waveform families used to model the templates and the signals.

2.3 Coincident Matched-Filter Search for Compact Binaries

To search for coalescing compact binaries with LIGO and Virgo, the offline search pipeline implements a coincident matched-filter search. If the detector noise was stationary and Gaussian, matched filtering alone would be sufficient to determine the statistical significance of a signal. For such stationary noise, demanding that the signal is present in two or more detectors in the network (coincidence) would provide a sufficiently low false-alarm rate to claim a detection at a matched-filter network signal-to-noise ratio of 8; the signal strength used to estimate aLIGO's event rate in Ref. [21]. However, the presence of non-stationary and non-Gaussian noise transients (*glitches*) in the detector noise increases the false-alarm rate at a given signal-to-noise ratio and additional statistical tests must be used to separate signals from noise. The output of the matched filter is combined with these additional tests to create a new detection statistic for coincident detection candidates. To determine the significance of these candidates, the noise background must be estimated to create a map between the numeric value of the detection statistic and the false-alarm rate (or, equivalently, false-alarm probability). Background noise is estimated by performing coincidence tests on detector data which has been time-shifted such that coincident candidates no longer represents a coincident detection. The search pipeline consists of several stages which are applied to the data to construct coincident detection candidates and measure their significance.

To search for gravitational waves from compact binaries, the search pipeline first locates the data from the detectors, which is stored on disk. Analysis over a period of data can be parallelized over time and over detector allowing the search to execute multiple search programs simultaneously that process small blocks of data for each detector. In the S6/VSR2,3 search, the analysis block size is set to 2048 seconds. The data is first used to construct the template bank that will be used to matched filter the data [49, 50, 51, 52, 53]. The bank is constructed by specifying the boundaries

of the target astrophysical space and the desired *minimal match*, the fractional loss in matched-filter signal-to-noise ratio caused by the discrete nature of the bank. The minimal match is chosen so that the bank is dense enough that any gravitational wave in the target space can be recovered with a loss of signal-to-noise ratio no greater than a chosen maximum, usually set to 3% [66]. A metric is constructed on the signal space that locally measures the fractional loss in signal-to-noise ratio for varying mass parameters of the templates [52]. This metric (and hence the template placement) depends on the power spectral density of the detector noise. Since inspiral signals have more cycles at lower frequencies, a detector with better low-frequency sensitivity relative to high frequencies will have more discriminating power and thus require a denser bank to maintain the desired minimal match.

The pipeline then matched filters the template waveforms against the data. The matched filter consists of a weighted inner product in the frequency domain used to construct the (squared) signal-to-noise ratio, given by

$$\rho^2(t) = \frac{(s|h_c)^2 + (s|h_s)^2}{(h_c|h_c)}\,, \tag{2.6}$$

where h_c and h_s are the two orthogonal phases of the template.

$$(s|h)(t) = 4\int_{f_{min}}^{f_{nyquist}} \frac{\tilde{s}(f)\tilde{h}^*(f)}{S_n(f)} e^{2\pi i f t}\,\mathrm{d}f. \tag{2.7}$$

Here $\tilde{s}$ denotes the Fourier-transformed detector data and $\tilde{h}$ denotes the Fourier-transformed template waveform. As in the S6/VSR2,3 search, each 2048 second block of data is sub-divided into fifteen 256 second segments, each overlapped by 128 seconds. The noise power spectral density $S_n(f)$ is computed by taking the bin-by-bin median of each of the power spectral density of each of the fifteen segments. The fifteen segments are then each matched filtered, with the first and last 64 seconds of each segment ignored, due to corruption of the filter by FFT wrap-around [48]

Times when the signal-to-noise ratio exceeds a pre-defined threshold are considered gravitational-wave candidates, called *triggers* [48]. This threshold was set to a signal-to-noise ratio of 5.5 in S6/VSER2,3. Since the signal-to-noise ratio can exceed this threshold for many sample points around the time of a signal, clustering is performed on these triggers in time, so that one trigger can be associated with

a signal. Template-length based clustering of Ref. [48] was used in the S6/VSR2,3 search. For a sufficiently loud event, several nearby templates in the bank may also produce triggers associated with the same signal and so clustering over the template bank can also be used to limit the number of triggers produced by the search. The S6/VSR2,3 search used a 30 ms time window to cluster over the bank.

Since non-Gaussian noise transients in the data can also produce excursions in the signal-to-noise ratio, an additional signal-based veto is then constructed to ensure that the matched filter signal-to-noise ratio is consistent with an inspiral signal. To construct this test, the template is split into p bins of equal power, and a matched filter ρ_l constructed for each of these bins. Triggers are then subject to the χ^2 test, given by

$$\chi^2 = p\sum_{l=1}^{p}\left[\left(\frac{\rho_c}{p} - \rho_c^l\right)^2 + \left(\frac{\rho_s}{p} - \rho_s^l\right)^2\right], \tag{2.8}$$

where ρ_c and ρ_s are the two orthogonal filter phases. Real gravitational-wave signals would return a low number for the χ^2 test, while candidates caused by noise transients will return a high number for the χ^2 test [58]. In the S6/VSR2,3 analysis, we set $p = 16$. The value of the χ^2 test is used to calculate a new detection statistic, called the *reweighted signal-to-noise ratio*, given by

$$\hat{\rho} = \begin{cases} \rho & \text{for } \chi^2 \leq n_{\rm dof} \\ \rho[\frac{1}{2}(1 + (\frac{\chi^2}{n_{dof}})^3)]^{-\frac{1}{6}} & \text{for } \chi^2 > n_{\rm dof}, \end{cases} \tag{2.9}$$

where $n_{\rm dof} = 2p - 2$ is the number of degrees of freedom in the χ^2 test [59]. Since candidates caused by noise transients generally return a high χ^2 statistic, the new detection statistic down weights the signal-to-noise ratio of candidates by dividing with the χ^2 statistic [15].

The quality of the data generated by the LIGO and Virgo detectors is scrutinized to mitigate noise and to improve the reach of the detectors [62, 63]. Data quality investigations characterize times of poor detector performance according to three broad classifications: (i) the data quality is sufficiently poor that the data should be discarded; (ii) an instrumental artifact with a known physical coupling to the recorded strain is observed by monitoring environmental or auxillary control channels; (iii) a statistical correlation is observed between a high trigger rate from the search and

excess noise power in environmental or auxillary control channels. The first class of data is removed before searching for signals. For the second two classes, a *data quality veto* is created. Vetoes are time intervals during which the pipeline removes all candidate events from the search. Improved methods for tuning and applying vetoes in compact object binary searches have been investigated [67], however these methods were not used in S6/VSR2,3. Investigation of these new approaches is outside the scope of this work and we apply the same data-quality vetoes as they were tuned for the S6 search.

A true gravitational-wave signal would be incident on all detectors in the network at approximately the same time. The maximum time-of-arrival difference between detectors is given by the light-travel time between observatories. Noise, however, will be independent between detectors since the interferometers are far apart. For this reason, we require the candidates to be coincident between detectors: they must arrive within the light-travel time between detectors, approximately 11 milliseconds for the two LIGO detectors, with a few milliseconds of padding to account for timing errors. The pipeline also requires that the mass parameters of the signal are consistent between all detectors, as would be expected for a true gravitational wave.

To claim a detection of gravitational waves, it is necessary to calculate the false-alarm rate of the candidate and demonstrate that it is very unlikely to occur due to noise in the detectors. To measure the noise background in the search, the pipeline shifts the triggers generated by filtering each detector's strain data by an amount greater than the light-travel time between detectors, and applies the coincidence test again. Coincident triggers that occur in the shifted data cannot be due to gravitational waves and thus represent background noise. By repeating this test with many different time lags, we can obtain a good estimate of the rate of background triggers as a function of the combined reweighted signal-to-noise ratio detection statistic. For a two-detector network, the combined statistic is given by

$$\hat{\rho}^c = \sqrt{\hat{\rho}^2_{\mathrm{L1}} + \hat{\rho}^2_{\mathrm{H1}}}, \tag{2.10}$$

where H1 is the LIGO Hanford detector and L1 is the LIGO Livingston detector. The map between $\hat{\rho}^c$ and false-alarm rate allows us to estimate the significance of gravitational-wave candidates in the search. Since the rate of background triggers

can depend strongly on the mass of the template, the search computes different maps between $\hat{\rho}^c$ and false-alarm rate for different regions of the mass parameter space independently.

2.4 Measuring the performance of a Search Pipeline

As the primary metric of search sensitivity in the presence of real detector data that contains non-Gaussian transient noise sources, we measure the sensitivity of a pipeline by finding the *sensitive volume*, which is proportional to the number of detections a pipeline will make per unit time at a given false-alarm rate. This is given by:

$$V(F) = \int \epsilon(F; r, \Omega, \mathbf{\Lambda}) p(r, \Omega, \mathbf{\Lambda}) r^2 \mathrm{d}r \mathrm{d}\Omega \mathrm{d}\mathbf{\Lambda}. \tag{2.11}$$

Here, $\mathbf{\Lambda}$ are the physical parameters of a signal (in this study, $\{m_1, m_2, \vec{s_1}, \vec{s_2}\}$), $p(r, \Omega, \mathbf{\Lambda})$ is the distribution of signals in the universe, and ϵ is the efficiency of the pipeline at detecting signals at a distance r, sky location Ω, and false-alarm rate F.

We estimate the sensitive volume by adding to the data a large number of simulated signals (*injections*) that are randomly drawn from a distribution $q(r, \Omega, \mathbf{\Lambda})$. We re-analyze the data with these simulated signals added and, for each injection, determine if a coincident trigger is present within 1 second of the time of the injection. If a trigger is present, we use the combined reweighted signal-to-noise ratio to compute its false-alarm rate. If no trigger is present, the injection is *missed*, i.e., the signal cannot be distinguished from noise at any false-alarm rate threshold. At some distance $r_{\max}$ we expect that any signal with $r > r_{\max}$ will be missed. Likewise, within some distance $r_{\min}$ we expect that nearly every signal will be found, even at an extremely small ($\lesssim 10^{-4}$/yr) false-alarm rate threshold. These bounds depend on the physical parameters of a signal. Gravitational waves from more massive systems have larger amplitudes, and thus can be detected at greater distances than less massive systems. To first order, if a binary with a reference *chirp mass* $\mathcal{M}_0 = (m_1 m_2)^{3/5}/(m_1+m_2)^{1/5}$ is detected at a distance r_0, then a binary with arbitrary chirp mass $\mathcal{M}$ will be detected with approximately the same reweighted signal-to-noise ratio at a distance:

$$r = r_0 (\mathcal{M}/\mathcal{M}_0)^{5/6}. \tag{2.12}$$

For each injection, we scale these bounds using Eq. (2.12), then draw the distance uniformly between them. The sensitive volume is then simply an average over the total number of injections N:

$$V(F) \approx \frac{1}{N}\sum_{i=1}^{N} g_i(F) \equiv \langle g(F) \rangle \,, \tag{2.13}$$

where:

$$g_i(F) = \frac{4\pi}{3}\left[r_{\mathrm{min},i}^3 + 3r_i^2(r_{\mathrm{max},i} - r_{\mathrm{min},i})\hat{\epsilon}(F; F_i, r_i, \Omega_i, \mathbf{\Lambda}_i)\right] . \tag{2.14}$$

Here, $\hat{\epsilon} = 1$ if $F_i \leq F$, and 0 otherwise. The error in the estimate is:

$$\delta V = \sqrt{\frac{\langle g^2 \rangle - \langle g \rangle^2}{N}}. \tag{2.15}$$

Chapter 3

Binary Neutron Star and Neutron star – Black Hole Sources

3.1 Population of BNS Sources

Electromagnetic observations suggest that the neutron star (NS) mass distribution in binary neutron star (BNS) peaks at $1.35M_\odot - 1.5M_\odot$ with a narrow width [68], although NSs in globular clusters seem to have a considerably wider mass distribution [68]. There is also evidence that a neutron star in one system has a mass as high as $\sim 3M_\odot$ [69].

If the neutron stars are rotating, coupling between the neutron stars' spin $\boldsymbol{S}_{1,2}$ and the orbital angular momentum $\boldsymbol{L}$ of the binary will affect the dynamics of BNS mergers [70, 71, 72, 73]. We measure the neutron stars' spin using the dimensionless parameter $\boldsymbol{\chi}_{1,2} = \boldsymbol{S}_{1,2}/m_{1,2}^2$. The maximum spin value for a wide class of neutron star equations of state is $\chi \equiv |\boldsymbol{\chi}| \sim 0.7$ [74]. However, the spins of neutron stars in BNS systems is likely to be smaller than this limit. The spin period at the birth of a neutron star is thought to be in the range 10–140 ms [75, 76]. During the evolution of the binary, accretion may increase the spin of one of the stars [77], however neutron stars are unlikely to have periods less than 1 ms [78], corresponding to a dimensionless spin of $\chi \sim 0.4$. The period of the fastest known pulsar in a double neutron star system, J0737–3039A, is 22.70 ms [79], corresponding to a spin of only $\chi \sim 0.05$.

3.2 Population of NSBH Sources

Although no NSBH binaries have been directly observed, both NSs and black holes (BHs) have been observed in other binary systems, and these observations can be used to make inferences about the mass and spin distributions that might be expected in NSBH binaries. Several BNS systems and neutron star-white dwarf (NSWD) systems have been observed by detecting their electromagnetic signatures. The observational data for BHs is more limited than for NSs.

Black holes observed in X-ray binaries can be used to estimate the BH mass distribution, though it is difficult to disentangle the individual masses and inclination angle with only electromagnetic observations [80]. Using a population of ~ 20 low-mass X-ray binary systems with estimated masses, two separate works found that a BH mass distribution of $7.8 \pm 1.2 M_{\odot}$ fits the observed data well [80, 81]. There is evidence that there is a "mass gap" between $3M_{\odot}$ and $5M_{\odot}$ where BHs will not form [80, 81], although this may be due to observational bias [82]. When high-mass X-ray binary systems are considered the mass distribution increases to $9.2012 \pm 3 M_{\odot}$, although a Gaussian model is a poor fit for these systems [81]. Evidence exists for a stellar mass black hole with mass $> 20 M_{\odot}$ in the IC 10 X-1 x-ray binary [83, 84]. Observations of black hole spin have found spin values that span the minimum and maximum possible values for Kerr black holes [85], therefore we conservatively assume a uniform black-hole spin distribution between 0 and 1.

3.3 Modelling Gravitational Waveforms

Achieving aLIGO's optimal sensitivity to NSBH binaries and exploring their physics requires accurate modeling of the gravitational waves emitted over many hundreds of orbits as the signal sweeps through the detector's sensitive band. For BNS systems the mass ratio between the two neutron stars is small and the angular momenta of the neutron stars (the neutron stars' spins) is low. In this case, the emitted waves are well modeled by PN theory [39, 29, 55]. However, NSBH binaries can have significantly larger mass ratios and the spin of the black hole can be much larger than that of a neutron star. The combined effects of mass ratio and spin present challenges in constructing accurate gravitational waveform models for NSBH systems, compared

to BNS systems. For the studies in this paper, we choose to use a uniform range of 3 to 15 solar masses for the black holes in our NSBH signal population. This is partly motivated by the considerations above, and partly by our concern of the validity of inspiral-only, point particle waveform models for high-mass NSBH systems.

3.3.1 Constructing post-Newtonian Waveforms

One way we can model the gravitational waveforms of BNS and NSBH binaries is by constructing waveforms using the PN approximations of the binary's equation of motion and gravitational radiation. To obtain the gravitational-wave phase from these quantities, we assume that the binary evolves adiabatically through a series of quasi-circular orbits. This is a reasonable approximation as gravitational radiation is expected to circularize the orbits of isolated binaries [86]. In this limit, the equations of motion reduce to series expansions of the center-of-mass energy $E(v)$ and gravitational-wave flux $\mathcal{F}(v)$, which are expanded as a power series in the orbital velocity v around $v = 0$. They are given as

$$E(v) = E_{\rm N} v^2 \left(1 + \sum_{n=2}^{6} E_i v^i\right), \tag{3.1}$$

$$F(v) = F_{\rm N} v^{10} \left(1 + \sum_{n=2}^{7} F_i v^i\right), \tag{3.2}$$

where the coefficients $\{E_{\rm N}, E_i, F_{\rm N}, F_i\}$ are defined in Appendix A.1. For terms not involving the spin of the objects, the energy is known to order v^6, while the flux is known to v^7, referred to as 3.0PN and 3.5PN, respectively. At order 3.0PN, the flux contains terms proportional to both v^6 and $v^6 \log v$; which are regarded to be of the same order. Complete terms involving the spins of the objects first appear as spin-orbit couplings at 1.5PN order, with spin-spin couplings entering at 2PN order, and next-to-leading order spin-orbit couplings known at 2.5PN order.

We use the assumption that these systems are evolving independently to relate the PN energy and gravitational-wave flux equations, i.e. the loss of energy of the system is given by the gravitational-wave flux

$$\frac{dE}{dt} = -\mathcal{F}. \tag{3.3}$$

This can be re-arranged to give an expression for the time evolution of the orbital velocity,

$$\frac{dv}{dt} = -\frac{\mathcal{F}(v)}{E'(v)}, \tag{3.4}$$

where $E'(v) = dE/dv$. The orbital evolution can be transformed to the gravitational waveform by matching the near-zone gravitational potentials to the wave zone. The amplitude of gravitational waves approximated in this way are given by the PN expansion of the amplitude. This gives different amplitudes for different modes of the orbital frequency. The dominant gravitational-wave frequency f is given by twice the orbital frequency, which is related to the orbital velocity by $v = (\pi M f)^{1/3}$. The orbital phase is therefore given by

$$\frac{d\phi}{dt} = \frac{v^3}{M}, \tag{3.5}$$

and the phase of the dominant gravitational-wave mode is twice the orbital phase. Here, we will only expand the gravitational-wave amplitude to Newtonian order (0PN), which, when combined with the phase, is referred to as a restricted PN waveform.

Solutions $v(t)$ and $\phi(t)$ to Eqs. (3.4) and (3.5) can be used to construct the plus and cross polarizations and the observed gravitational waveform. For restricted waveforms, these are:

$$h_+(t) = -\frac{2\,M\,\eta}{D_L}\,v^2\,(1+\cos^2\theta)\,\cos 2\phi(t)\ , \tag{3.6}$$

$$h_\times(t) = -\frac{2\,M\,\eta}{D_L}\,v^2\,2\cos\theta\,\sin 2\phi(t)\ , \tag{3.7}$$

$$h(t) = F_+\,h_+(t) + F_\times\,h_\times(t)\ . \tag{3.8}$$

Here F_+ and $F_\times$ are the antenna pattern functions of the detector, D_L is the luminosity distance between the binary and observer, and θ is the inclination angle between the orbital angular momentum of the binary and the direction of gravitational-wave propagation: $\cos\theta = \hat{L}\cdot\hat{N}$. Thus, a non-precessing, restricted PN waveform is fully specified by $v(t)$ and $\phi(t)$ (or equivalently $t(v)$ and $\phi(v)$).

We now have the ingredients necessary to produce the TaylorT2 and TaylorT4 families of approximants, which we describe in the following sections.

3.3.2 TaylorT4

The TaylorT4 approximant, introduced in [87], is formed by numerically solving the differential equation

$$\frac{dv}{dt} = \left[\frac{-\mathcal{F}(v)}{E'(v)}\right]_k = A_k(v). \tag{3.9}$$

The notation $[Q]_k$ indicates that the quantity Q is to be truncated at v^k order. Terms containing pieces logarithmic in v are considered to contribute at the order given by the non-logarithmic part. Thus waveforms expanded to 3.5PN order in the phase would be truncated at $k = 7$. We use A_k as shorthand for the truncated quantity that is used as the expression for dv/dt.

The resulting differential equation, given explicitly in Appendix A.2.1, is non-linear and therefore must be solved numerically. The result is a function $v(t)$. The phase can then be calculated by

$$\frac{d\phi}{dt} = \frac{v(t)^3}{M}. \tag{3.10}$$

The phase is integrated from a fiducial starting frequency up to the minimum energy condition (MECO), which is defined by

$$\frac{dE(v)}{dv} = 0. \tag{3.11}$$

The MECO frequency is where we consider the adiabatic approximation to have broken down. Note that the MECO frequency is dependent on not only the masses but also the spins of the objects; specifically, systems where the objects' spins are aligned with the orbital angular momentum will have a higher MECO frequency. When the partial spin-related terms at 3.0PN and 3.5PN are included, however, there are regions of the NSBH parameter space for which the MECO condition is never satisfied. For these cases, we impose that the rate of increase in frequency must not decrease (i.e. we stop if $dv/dt \leq 0$), and that the characteristic velocity of the binary is less than c (i.e. we stop if $v \geq 1$). We terminate the waveforms as soon as any of these stopping conditions are met.

3.3.3 TaylorT2

In contrast to the TaylorT4 approximant, the TaylorT2 approximant is constructed by expanding t in terms of v and truncating the expression to consistent PN order. We first construct the quantity

$$\frac{dt}{dv} = \left[\frac{E'(v)}{-\mathcal{F}(v)}\right]_k = B_k(v). \tag{3.12}$$

This can be combined with the integral of Eq. (3.5) and solved in closed form as a perturbative expansion in v,

$$\phi(v) = \int \frac{v^3}{M} B_k(v) dv. \tag{3.13}$$

The explicit result of this integral is given in Ap. A.2.2. Similar to TaylorT4, the phase is generally calculated up to the MECO frequency. However, for some points of parameter space, this formulation can result in a frequency that is not monotonic below the MECO frequency. As with TaylorT4, we stop the waveform evolution with $dv/dt \leq 0$ or $v \geq 1$.

A related approximant can be computed directly in the frequency domain by using the stationary phase approximation [88, 39]. This approximant is called TaylorF2 and can be expressed as an analytic expression of the form

$$\phi(f) = A(f) e^{i\psi(f)}, \tag{3.14}$$

where the phase takes the form

$$\psi(f) = \sum_{i=0}^{7} \sum_{j=0}^{1} \lambda_{i,j} f^{(i-5)/3} \log^j f. \tag{3.15}$$

The full expressions for the amplitude and phase are given in Ap. A.2.3. Because the stationary phase approximation is generally valid, the TaylorT2 and TaylorF2 approximants are nearly indistinguishable [88]. An advantage of the TaylorF2 approximant comes from the fact that it can be analytically calculated in the frequency domain. In practice, waveforms that are generated in the frequency domain without the use of integration are less computationally costly, and so searches for gravitational

waves from inspiraling binary systems have been performed using the TaylorF2 approximant [89, 88, 39, 7, 90, 8, 91, 10, 92, 13, 14, 15, 93, 94, 95].

3.3.4 SEOBNRv1

An additional approximant we use in this work is the spinning effective one-body model (SEOBNRv1), presented in Ref. [96]. This approximant incorporates the results of black hole perturbation theory, the self-force formalism and PN results. The model has been calibrated to numerical relativity simulations, including simulations where the objects' spins were (anti-) aligned with the orbital angular momentum and had magnitudes of $\chi \pm 0.4$. In order to compare these waveforms more fairly with the PN approximants that only model the inspiral, we truncate this model before the merger section of the waveform. Although SEOBNRv1 is limited to $\chi \leq 0.6$, further models have been developed since this work was completed that extend the model to allow generic spins [37].

Chapter 4

Effects of Spin on Binary Neutron Star Searches

4.1 Introduction

The effect of spin-orbit and spin-spin interactions were neglected in previous BNS searches [15], as they do not have a significant effect on the $\sim$ 1600 gravitational wave cycles in the 40–2000 Hz sensitive band of first-generation detectors [97]. However, aLIGO and AdV will be sensitive to gravitational-wave frequencies between 10–2000Hz, increasing the number of cycles in band by an order of magnitude. Initial studies have demonstrated that over this band, the small secular effects produced by spin-orbit and spin-spin coupling will have a significant effect on the detectability of BNS systems with non-trivial component spins [98]. However, the current geometric method for placing BNS templates [99] does not incorporate spin. While numerical (stochastic) methods could be used to include spin, these require substantially more templates than a comparable geometric approach [100].

We consider two populations of neutron star binaries: the first has spins uniformly distributed from $\chi = 0$ to 0.4, the second, a sub-set of this, has spins between 0 and 0.05. This extended spin distribution allows for the possibility of serendipitous discovery of BNS systems in globular clusters, where the evolutionary paths may be different than that in field binaries [101]. Since supernova kicks may cause the direction of the neutron star's angular momentum to be misaligned with the orbital angular momentum of the binary [102], or the binaries may be formed by direct

capture, we consider a population of binaries with an isotropic spin distribution.

We evaluate a new geometric algorithm for placing templates for BNS systems with spin, presented in [55], which has a significantly higher sensitivity than previous searches. The algorithm constructs a metric on the parameter space using the various coefficients of the TaylorF2 expansion of the orbital phase as coordinates. In such a coordinate system the parameter space metric is globally flat, therefore we can transform into a Euclidean coordinate system. Finally, our method uses a Principal Coordinate Analysis to identify a two dimensional manifold that can be used to cover the aligned spin BNS parameter space using existing two dimensional lattice placement algorithms.

We perform a systematic evaluation of the ability of a search that neglects spin to detect gravitational waves for BNS in aLIGO and AdV. We show that this search will lose more than 3% of the matched filter signal-to-noise ratio for 59% (6%) of signals if it is used to search for BNS systems with spins uniformly distributed between $0 \leq \chi_{1,2} \leq 0.4(0.05)$; this is unsatisfactory over a large region of the signal parameter space. We show that by considering BNS systems where the spin of the neutron stars are aligned with the orbital angular momentum (i.e. the binary is not precessing), we can create a two-dimensional template bank that is efficient at detecting spin-aligned BNS signals. Finally we demonstrate that this bank is sufficient to detect signals from generic spinning, precessing binaries in aLIGO and AdV. The spin-aligned bank loses more than 3% of the signal-to-noise ratio for only 9% (0.2%) of signals, sufficient to construct a sensitive and unbiased search for BNS systems in aLIGO and AdV.

4.2 BNS Search Sensitivity

We quantify the performance of templated matched-filter searches by the fitting factor (FF) of the search [65]. The fitting factor is the fraction of the signal-to-noise ratio that would be recovered when matching a given signal with the best matching waveform in the template bank. When searching for BNSs, we do not know the exact physical parameters of the system. We assume that the masses of the neutron stars lie between 1 and 3 $M_{\odot}$ and construct a bank of waveform templates to span this region of the mass parameter space. We measure the sensitivity of this bank using the fitting factor.

In searches for gravitational waves using LIGO and Virgo, the bank is constructed such that the fitting factor for any signal in the target parameter space will never be less than 0.97. At least one of the templates in the bank must have a maximized overlap of 0.97 (or more) with the signal. This value is chosen to correspond to an event rate loss of no more than 10% of possible sources within the range of the detectors [103]. In this chapter, we use a fitting factor of 0.97 to construct search template banks.

We now test whether a bank of templates that does not model the effect of spin is sufficient to detect generic, spinning BNS sources in aLIGO and AdV. We create a bank of non-spinning templates that would recover any non-spinning BNS system with a fitting factor greater than 0.97. This bank is constructed using TaylorF2 waveforms, which are constructed using the stationary phase approximation to the gravitational-wave phasing accurate to 3.5 post-Newtonian (PN) order [104, 39]. To create a bank of these waveforms we use the hexagonal-placement method defined in [54], which was used in the majority of previous searches in LIGO and Virgo [12, 13, 14]. This template bank is placed using the metric given in [105], which is valid, by construction, for templates at 2PN order. Our signal waveforms are constructed using the SpinTaylorT4 waveform [106], a time-domain waveform accurate to 3.5PN order in the orbital phase which includes the leading order spin-orbit, spin-spin, and precessional modulation effects and implemented in the LSC Algorithm Library Suite [107]. We first confirm that although the bank is constructed at 2PN order, it yields fitting factors greater than 0.97 for both the TaylorF2 and SpinTaylorT4 non-spinning waveforms at 3.5PN order. To simulate a population of spinning BNS sources, we generate 100,000 signals with component masses uniformly distributed between 1 and 3 $M_{\odot}$ and dimensionless spin magnitudes uniformly distributed between 0 and 0.4. The orientation of the spin, the orientation of the orbital angular momentum, and the sky location are isotropically distributed. To model the sensitivity of a second generation gravitational wave interferometer, we use the aLIGO zero-detuned, high-power sensitivity curve [108]. For our simulations, we use a lower frequency cutoff of 15Hz.

We note that for non-precessing systems the fitting factor is independent of the detector alignment and location; however this statement is not true for precessing

systems. For such systems, however, the distribution of fitting factors over a population of sources will be independent of the detector alignment and location. Therefore, for this study we calculate the fitting-factor for a single detector with an arbitrary location and position.

In Fig. 1 we show the distribution of fitting factors obtained when searching for our population of BNS sources with the non-spinning template bank. We see that 59% of signals were recovered with a fitting factor less than 0.97. If the maximum spin magnitude is restricted to 0.05, we find that 6% of signals are recovered with a FF less than 0.97. If BNS systems do exist with spin magnitudes up to 0.4, a template bank that captures the effects of spin will be required to maximize the number of BNS detections. Detection efficiency will be greatly reduced by using a template bank that only contains waveforms with no spin effects. Even under the assumption that component spins in BNS systems will be no greater than 0.05, detection efficiency will be decreased if the effect of spin on the signal waveform is ignored.

4.3 A template placement algorithm for aligned-spin BNS templates

As we have demonstrated in the previous section, there is a substantial region of the BNS parameter space where a significant loss in signal-to-noise ratio would be encountered when searching for astrophysically plausible, spinning BNS systems with non-spinning templates. It has been suggested that using BNS templates where the spins of the system are aligned with the orbital angular momentum is sufficient for detecting generic BNS systems with second-generation detectors [98] using TaylorF2 templates that incorporate the leading order spin-orbit and spin-spin corrections [109].

In this section we use these spin-aligned waveforms to construct a template bank that attempts to cover the full space of astrophysically plausible BNS spin configurations. This template bank should contain as few templates as possible, while still being able to detect any BNS system that might be observed with aLIGO and AdV. We use TaylorF2 waveforms accurate to 3.5PN order in orbital phase and including the leading order spin-orbit and spin-spin terms given by [109, 29] Since BNS systems coalesce at ~ 1500 Hz, significantly higher than the most sensitive band of the detectors, the waveform will be dominated by the inspiral part of the signal [29]. The effect

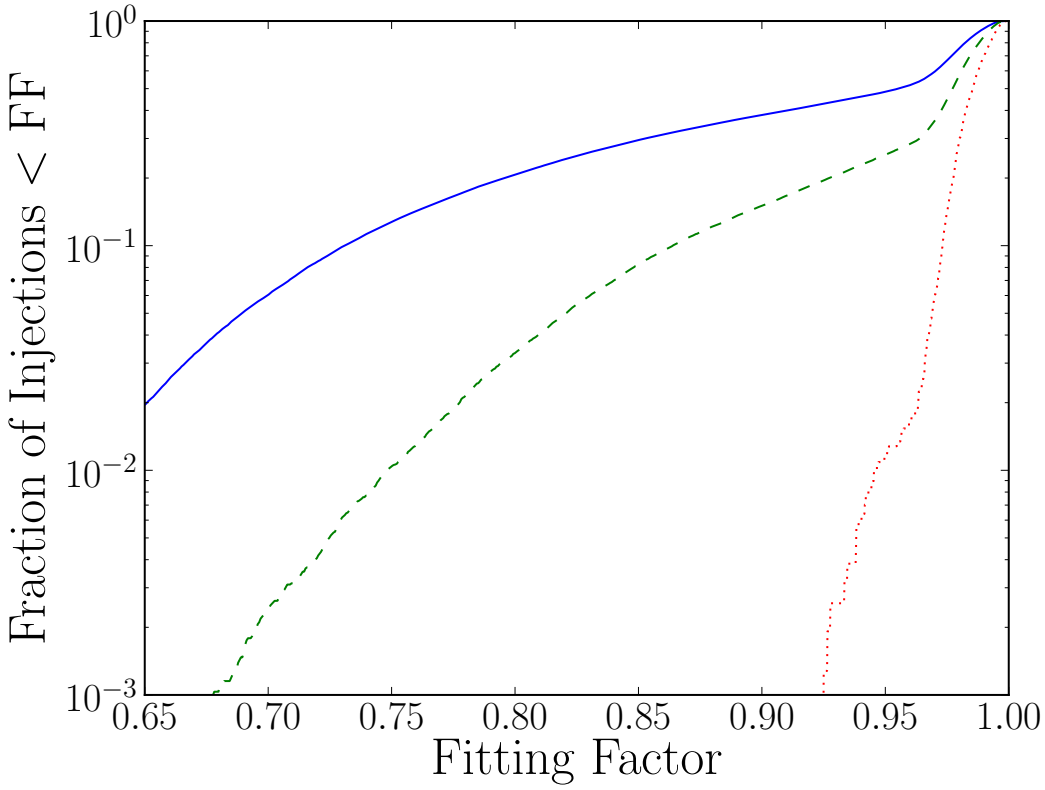

Figure 1: The distribution of fitting factors obtained by searching for the precessing BNS systems described in Sec. 4.2 with component spins up to 0.4 (blue solid line), 0.2 (green dashed line), and 0.05 (red dotted line) using the non-spinning BNS template bank described in Sec. 4.2 and the advanced LIGO, zero-detuned, high-power PSD with a 15Hz lower frequency cutoff.

of component spin on BNS inspiral waveforms has been well explored in the literature [71, 70, 72, 106]). For spin-aligned (i.e. non-precessing) waveforms, the dominant effects of component spin are spin-orbit coupling, which enters the waveform phasing at 1.5PN order, and spin1-spin2 coupling, which enters the waveform phasing at 2PN order. Other spin-related corrections to the PN phasing have been computed [110, 111], however, in this work we mainly restrict to only the two dominant terms.

Based on the results of [55], where we derive a metric for aligned-spin TaylorF2 waveforms, we can use a geometric algorithm for template bank placment. We place a hexagonal grid of templates in the two dominant coordinates ξ_1, ξ_2, which are derived in [55]. For BNS systems in aLIGO and AdV the extent of the physical parameter space in the remaining directions is smaller than the coverage radius of a template and can be neglected in nearly the entire parameter space. As the effective dimension of the space is two-dimensional, a hexagonal placement algorithm, similar to that used in previous searches of LIGO and Virgo data, can be employed to cover the space. This allows the method to be incorporated into existing search pipelines in a straightforward way. Where the third dimension, ξ_3, cannot be neglected, we stack the templates to ensure that the maximum mismatch due to the depth than 0.25%. For an aligned-spin template bank where the spin of each component is restricted to 0.4, using the advanced LIGO, zero-detuned high-power noise curve with a lower frequency cut-off of 15Hz, we find that approximately 520,000 templates are required. Roughly 100,000 of these templates were added by the stacking process.

We can verify that the template bank algorithm is working correctly by repeating the simulation described in Sec. 4.2, but evaluating the fitting factor between our bank of aligned-spin template waveforms and a set of signals that is restricted to having spins that are (anti-)aligned with the orbital angular momentum. The results of this simulation are shown in Fig. 2 and one can see that with our bank we do not observe fitting factors lower than 0.97 when searching for aligned spin BNS systems.

In the previous paragraphs we have restricted attention to the aLIGO zero-detuned, high-power predicted sensitivity with a 15Hz lower frequency cut off. However, we should verify that the conclusions we have drawn are valid for AdV, whose PSD is different from that of aLIGO, as shown in Fig. 3. Additionally we should also show that the choice to use a 15Hz cut off in the aLIGO PSD does not affect the

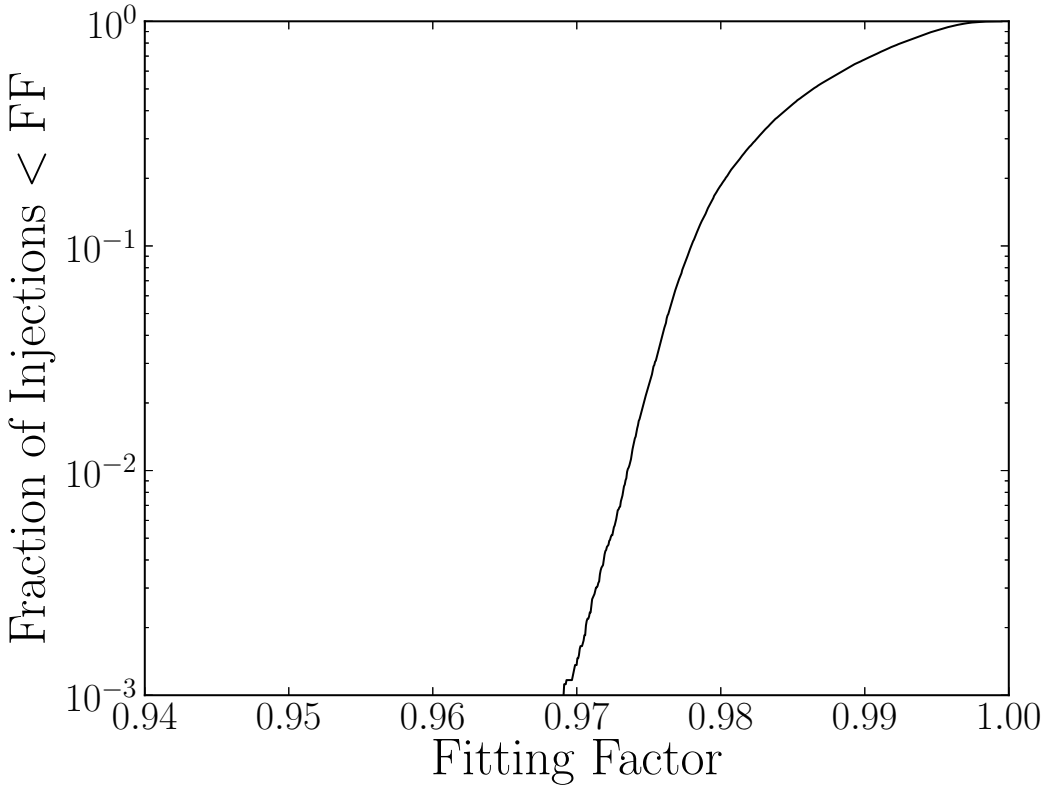

Figure 2: The distribution of fitting factors obtained by searching for aligned spin, binary neutron star systems, with spin magnitudes restricted to 0.4 using the aligned-spin BNS template bank described in Sec. 4.3 and the aLIGO, zero-detuned, high-power PSD with a 15Hz lower frequency cutoff.

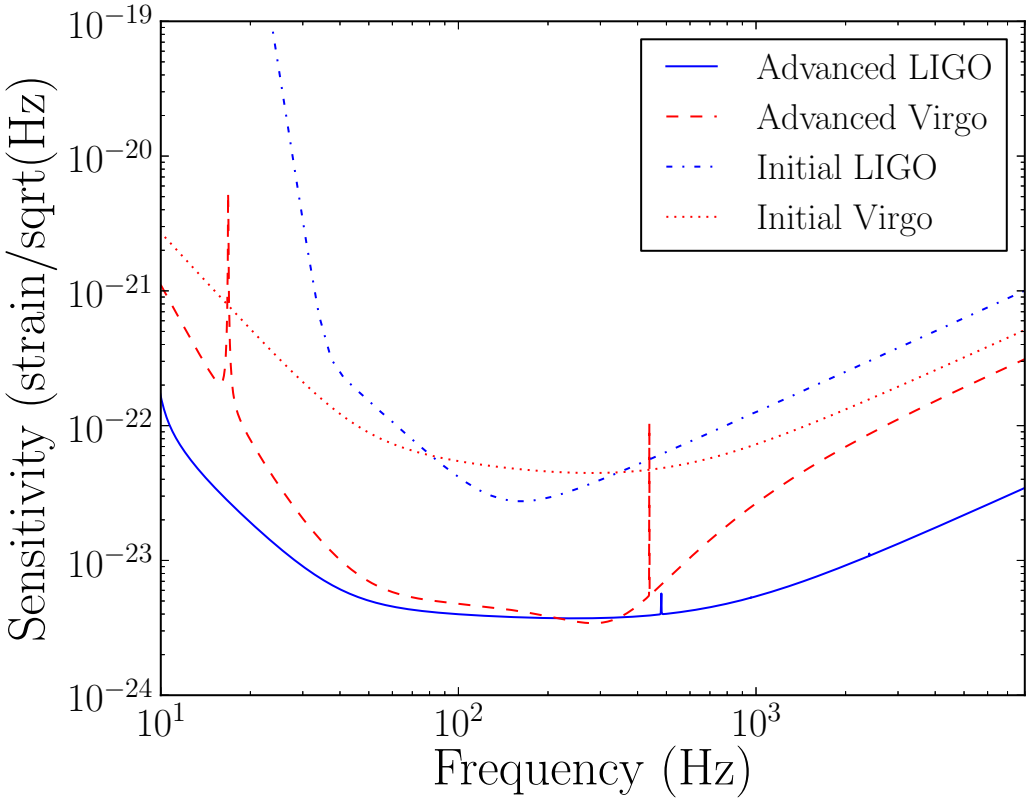

Figure 3: The amplitude spectral density for the aLIGO zero-detuned high-power design sensitivity (blue solid curve), AdV design sensitivity (red dashed curve), initial LIGO design sensitivity (blue bot-dash curve) and initial Virgo design sensitivity (red dotted curve).

conclusions made in this section. Using our method we find that we require approximately 120,000 templates to cover the parameter space for AdV, in comparison to approximately 520,000 templates for aLIGO. By comparing the results when using the aLIGO PSD with a 10Hz and 15Hz lower cut off we observe that using a 10Hz lower frequency cut off will increase the number of necessary templates from ~ 520000 to ~ 860000.

4.4 Comparison to alternative placement methods

An alternative approach to template placement for aligned spin systems is to use templates with "unphysical" values of the symmetric mass ratio, η. That is, to use non-spinning templates, with the desired range of chirp mass but where the range of η values is extended to include both values of η that are much lower than the relevant parameter space and values of η that are much higher, including templates with η greater than the physically possible limit of 0.25.

While unphysical η templates will produce an increase in efficiency when compared with non-spinning templates, the method is not as efficient as the aligned spin geometrical placement we have described. In addition, both methods require the same number of templates to cover the parameter space. Therefore, we would recommend using aligned spin templates placed using our metric algorithm as opposed to unphysical η templates.

Finally, we wish to compare the performance of the geometrical algorithm with the stochastic bank proposed in [100, 112]. The stochastic placement works by randomly placing points within the parameter space and rejecting points that are too "close" to points already in the bank. This has the advantage that it is valid for any parameter space metric, so we could use any of the metrics discussed above.

The disadvantage to a stochastic bank, when compared to a geometrically placed bank, is that it will require more templates to achieve the same level of coverage [100, 113]. For our parameter space, consisting of BNS signals with component spins up to 0.4 and using the advanced LIGO zero-detuned high-power design curve with a 15Hz lower frequency cut-off, we found that the stochastic placement produced a bank containing ~ 750000 templates, which is 44% more than with the geometrical placement. However, stochastic placement can still be used to place templates when no analytical metric is known, such as when the merger becomes important. In such regions of parameter space, the stochastic placement may still be the best algorithm to use to place a template bank.

4.5 Performance of the aligned spin template bank

In this section we would like to investigate the improvement in the detection of generic BNS systems that results from using a template bank that includes the dominant, non-precessing, spin effects. To do this we use the aligned spinning bank that we detail in Sec. 4.3 and compare this to the results of using a nonspinning bank as shown in Sec. 4.2.

Using our aligned spin template bank, we repeat the investigation from Sec. 4.2. We create a population of source BNS signals identical to those used in Fig. 4.2, and compute the fitting factor between these signals and the aligned spin template bank. The results of this are shown in FIG.4. To decrease the computational cost of this test, we only calculated the overlaps between a signal and templates that were within a range of $\pm 0.1 M_{\odot}$ in chirp mass. This is reasonable because the overlap will decrease rapidly with small changes in chirp mass, therefore we expect templates with very different values of chirp mass to have low overlaps with each other. We verified that this approach did not cause us to underestimate the fitting-factor of our banks.

We can now compare the results obtained in this section, using our aligned-spin template bank, with the results obtained in section 4.2, using a non-spinning template bank. One can clearly see an improvement in the distribution of fitting factors when using the aligned spin template bank. The fraction of signals that fall below a fitting factor of 0.97, when the spin magnitudes are restricted to 0.4, falls from 59% to 9%. We also see an improvement for signals that have spin magnitudes restricted to 0.05, where the fraction of signals falling below a fitting factor of 0.97 drops from 6% to 0.2%. We can also compare the performance of the aligned-spin bank to that of the non-spinning bank as a function of the maximum spin magnitude, as shown in Fig. 5. We can see that regardless of the maximum component spin, the aligned spin bank will greatly reduce the number of signals recovered with fitting factors less than 0.97.

A small fraction of signals fall below a FF of 0.97, even when using the new aligned-spin template bank. We expect that these poor matches with the aligned template bank are due to precession. In general, precessional effects will not be important in BNS systems as the orbital angular momentum is significantly larger than the component spins. In such cases there is only a small angle between the total and orbital angular momenta and precession has only a small effect on the waveform.

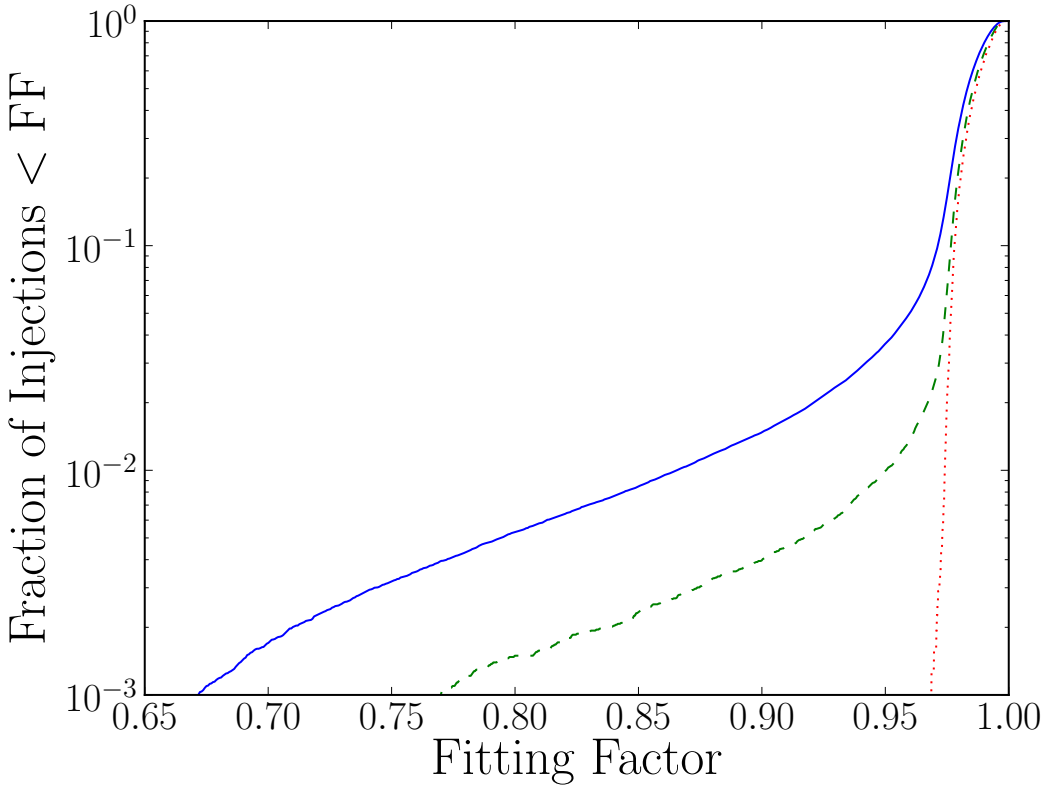

Figure 4: The distribution of fitting factors obtained by searching for the precessing signals described in Sec. 4.2 with component spins up to 0.4 (blue solid line), 0.2 (green dashed line), and 0.05 (red dotted line) using the aligned spin BNS template bank described in Sec. 4.3 and the advanced LIGO, zero-detuned, high-power PSD with a 15Hz lower frequency cutoff.

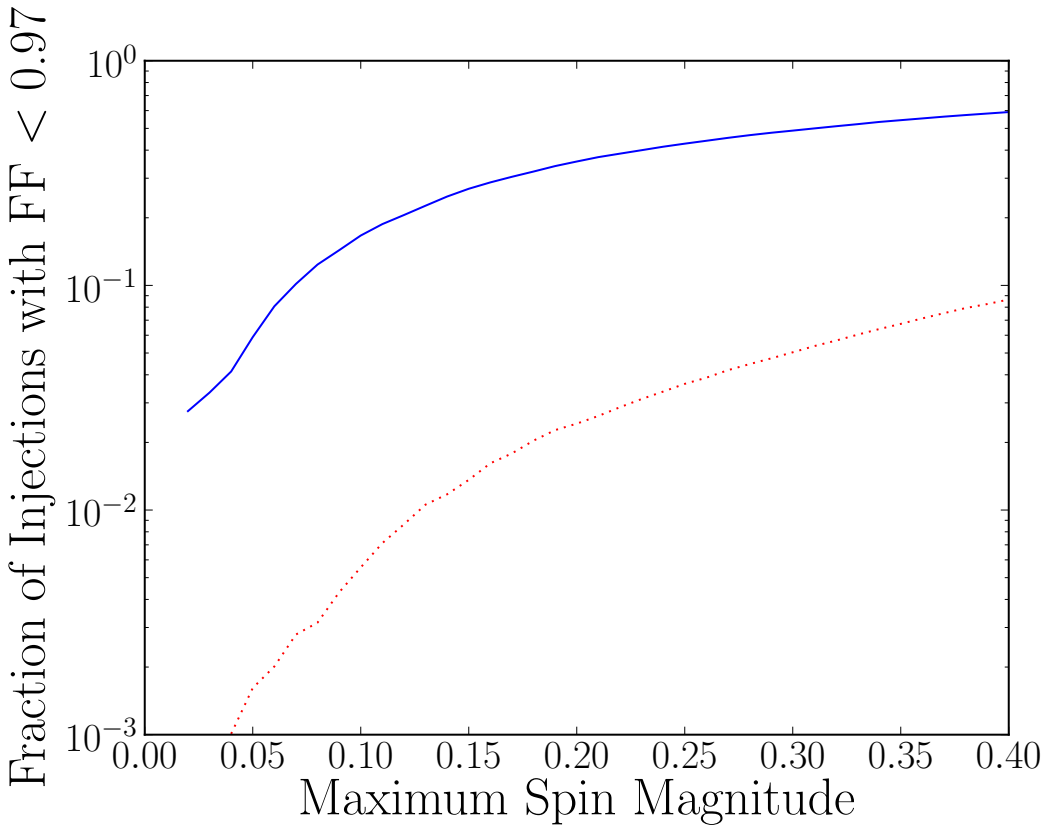

Figure 5: The fraction of the precessing signals described in Sec. 4.2 recovered with a fitting factor less than 0.97 as a function of the maximum component spin. Shown for the non-spinning BNS template bank described in Sec. 4.2 (blue solid line), and the aligned spin BNS template bank described in Sec. 4.3 (red dotted line). The advanced LIGO, zero-detuned, high-power PSD with a 15Hz lower frequency cutoff was used when computing the fitting factors.

However, there is a small region of parameter space where precessional effects *will* have an effect for BNS systems. Using the model of Ref. [114], applied to the small precession angles in BNS systems, we can predict for which systems precession will be most important. The orientation of a precessing binary must be defined using the total angular momentum rather than the orbital angular momentum as done with non-precessing binaries. The orientations with the worst matches should be those where the system is edge-on (angular momentum perpendicular to the viewing direction) and where the detector is nearly insensitive to the plus polarization and only sees the cross polarization (a binary overhead of the detector would have its angular momentum oriented 45° between the arms of the detector). We find that this is indeed the case; in fact, all cases with fitting factors less than 0.95 are close to this configuration. All of these cases also have biases in the recovered mass and spin parameters due to the secular effects of precession on the phasing of the waveform.

4.6 Conclusions

In this work we have investigated the effects of neglecting spin when searching for binary neutron star systems in aLIGO and AdV. We have found that, if component spins in binary neutron star systems are as large as 0.4, then neutron star spin cannot be neglected, and there is a non-trivial loss in signal-to-noise ratio even if the maximum spin is restricted to be less than 0.05. We have shown that the geometric algorithm for placing and aligned spin template bank works for aligned spin systems and have demonstrated that it does significantly better for generic, precessing BNS systems than the traditional non-spinning bank. However, for the BNS aligned spin $\chi_i < 0.4$ parameter space the aligned spin bank requires approximately five times as many templates as the non-spinning bank. This increased number of templates will increase the computational cost of the search and increase the number of background events, so needs to be balanced against the potential gain in being able to cover a larger region of parameter space. A further advantage of this method is the ease with which it can be incorporated into existing or future search pipelines, which include the use of signal-based vetoes [58] and coincidence algorithms [115]. In future work we will investigate how this template bank performs in data from the aLIGO and

AdV detectors which includes non-Gaussian and non-stationary noise features. Finally we note that the method proposed in this work should be applicable wherever the TaylorF2 waveforms closely represent actual gravitational waveforms. In a future work we will investigate how well this method performs in the binary black hole and neutron-star, black-hole regions of the parameter space. Wherever the TaylorF2 approximation begins to break down, a stochastic bank placement may still be the most viable option.

Chapter 5

Accuracy of Post-Newtonian Waveforms for Neutron Star – Black Hole Searches

5.1 Introduction

In this chapter we investigate if the currently available post-Newtonian models are sufficient for use in searches for gravitational-waves from the coalescence of a neutron star and a black hole. Given the uncertainties in the masses and spins of NSBH binaries, we consider a fairly broad mass and spin distribution when investigating the accuracy of NSBH waveforms. In this chapter, we consider NSBH binaries with the NS mass between 1 and 3 $M_\odot$, the BH mass between 3 and 15 $M_\odot$, the NS spin between 0 and 0.05 and the BH spin between 0 and 1. Between these limits, the distributions of mass and spin are all assumed to be uniform.

As described in Ch. 3, there are several different ways in which to solve the energy balance equation to obtain the gravitational-wave phase measurable by aLIGO; these different methods are known as PN *approximants*. While the convergence of the full PN series is not guaranteed, for BNS systems in Advanced LIGO, the available PN approximants produce waveforms that are indistinguishable for a given binary and are reliable for use in detection searches and parameter measurement [116, 29, 55]. However, for NSBH binaries the total mass, and hence the PN expansion parameter v, is larger. The mass ratio and spin corrections are also more significant. We investigate

the accuracy of waveforms generated by different PN approximants for observing NSBH binaries with aLIGO. To do this, one could compare subsequent terms in the PN expansion and determine the effect of neglecting them. However, in the case of systems whose component objects are spinning, only terms up to 2.5PN order are completely known [70, 72, 111]. This represents the leading order (1.5PN) and next-to-leading order (2.5PN) spin-orbit, along with the leading order (2.0PN) spin-spin contributions to the phasing [70, 72, 111]. We choose to compare approximants that are constructed with terms up to the same PN order, but that use inversely related differential equations to solve for the orbital dynamics, in addition to comparing to approximants that include higher order spin-related corrections at partially derived orders [117, 118]. These methods both have the effect of testing how well the PN series has converged. We also present a comparison between waveforms from these PN approximants where we fix the mass and spin parameters of the objects in order to understand when in the inspiral the waveforms diverge.

We consider two families of PN approximants for binaries where the spin of the black hole is aligned with the orbital angular momentum: TaylorT2 [89, 88, 39] and TaylorT4 [87]. In these models, we include all the completely known orbital evolution terms (up to 3.5PN order) [119, 41, 42, 89, 120, 46] and all the completely known spin-related terms (up to 2.5PN order) [121, 73, 70, 110, 122]. Restricting to systems where the spin angular momenta are aligned (or anti-aligned) with the orbital angular momentum means that the plane of the binary does not precess, simplifying our comparisons. However, this study captures the dominant effect of spin on the waveforms [114]. In Ch. 6, we investigate the effect of precession on detection searches [123]. We also consider the effective-one-body model as described in Ref. [96]. We restrict to comparing the inspiral portion of approximants. Even at the upper range of masses we consider, $(3 + 15)M_{\odot}$, it has been shown in the case of numerically modelled binary black hole waveforms that inspiral-only template banks recover $> 95\%$ of the signal power [30, 124]. We separately consider models that include spin-related terms up to 3.5PN order [117, 118]. Spin-orbit tail (3.0PN) and next-to-next-to-leading order spin-orbit (3.5PN) contributions to the phasing are known. However, these orders are incomplete as there are also unknown spin corrections at 3.0PN and 3.5PN, including spin-spin and (spin-induced) octupole-monopole couplings.

In Fig. 6 we show the distance an optimally oriented system would be observed at SNR 8 (the horizon distance), for a $1.4M_{\odot} - 10M_{\odot}$ NSBH system, as a function of the spin of the black hole, for both the aLIGO zero-detuned, high-power sensitivity curve and a plausible range of early aLIGO sensitivities [17]. Systems where the spin of the black hole is large in magnitude and aligned with the orbital angular momentum can be seen from a greater distance than systems where the spin is small or anti-aligned. Achieving this sensitivity requires NSBH waveforms that do not incur a significant loss in SNR when used as search templates [97]. Furthermore, extracting the physics from observed signals requires faithful templates for parameter measurement.

We find that no presently available waveform model is sufficiently accurate for use in aLIGO NSBH searches or parameter measurement. Our key results, Figs. 7-11, show the match between the various waveform families considered here. There is a significant disagreement between the PN approximants we have examined, even at at low ($\chi \sim 0.4$) spins and small ($m_{BH}/m_{NS} \sim 4$) mass ratios for TaylorF2 and TaylorT4. The match decreases as these increase with matches as low as ~ 0.1 observed. This motivates the need to compute higher order PN spin corrections.

Our present knowledge of NSBH waveforms will limit the ability of gravitational-wave observatories to accurately determine source parameters from the detected signals and may hinder their detection. Further analytical and numerical modeling of NSBH systems will be needed before aLIGO comes online in 2015 and reaches full sensitivity in $\sim$ 2019 [17].

The remainder of this chapter is organized as follows. In Sec. 3.3.1, we describe the construction of the PN approximants used and Sec. 2.2 describes our method of comparing them. In Sec. 5.2 we show the results of comparing different PN approximants, and show that there is a large discrepancy between the waveforms for NSBH binaries at relatively low black hole spins. In Sec. 5.3 we construct a new frequency domain approximant that is designed to agree with TaylorT4. This is followed by a comparison of the time domain approximants to their frequency domain counterparts in Sec. 5.4, where we demonstrate that they largely agree. Finally, in Sec. 5.5 and Sec. 5.6 we investigate where in the inspiral the disagreement between the waveform families becomes important. We demonstrate that the divergence occurs at surprisingly low velocities for even modest black hole spins. Finally in Sec. 5.7 we investigate whether maximizing over the mass and spin parameters of the waveform

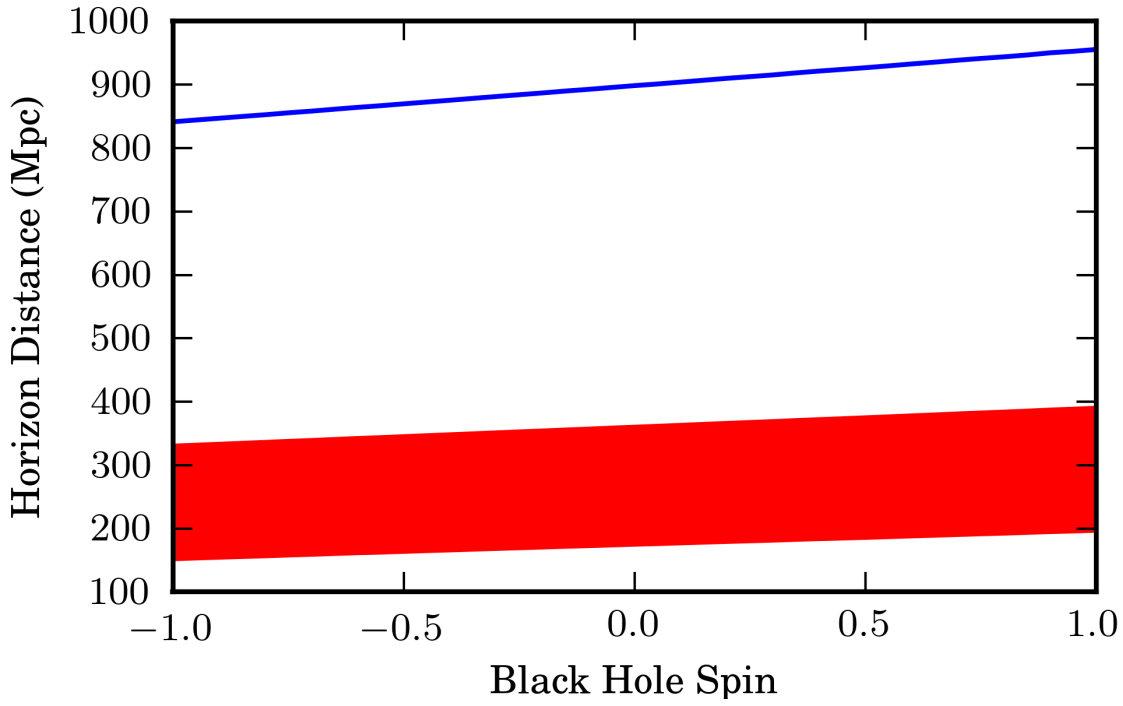

Figure 6: The horizon distance as a function of the spin of the black hole for a $1.4M_\odot - 10M_\odot$ NSBH system, for both the aLIGO zero-detuned, high-power aLIGO sensitivity curve (blue) and plausible early aLIGO detector sensitivities (red), with a 15 Hz lower frequency cutoff. Results are obtained using the TaylorT4 approximant including only the complete spin terms up to 2.5PN. Note that aLIGO will be sensitive to NSBH systems out to ~ 900 Mpc, and there will be increased sensitivity for systems with aligned black hole spins with large magnitudes.

can improve present models, and investigate the accuracy of the waveforms for early aLIGO observations when the detectors will have reduced low-frequency sensitivity when compared to the ultimate sensitivity.

5.2 Post-Newtonian approximant faithfulness comparison

Searches for gravitational waves from compact binary coalescences utilize matched-filtering [125, 48], in which the signal model is correlated with the detector output to construct a signal-to-noise ratio. If the signal model does not accurately capture the true gravitational waveform, then the signal-to-noise ratio, and hence the distance to

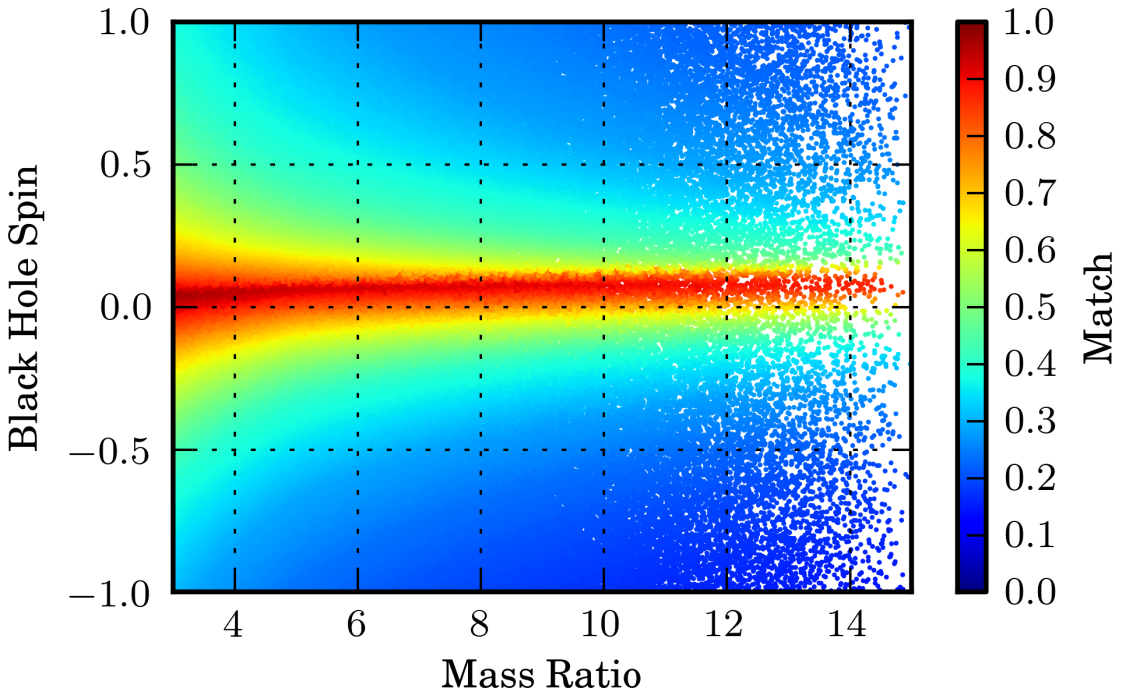

Figure 7: The match between the TaylorF2 and TaylorT4 approximants as a function of the spin of the black hole and the mass ratio of the system. Only the completely known spin-related corrections up to 2.5PN are included. Matches are calculated using the the aLIGO zero-detuned, high-power sensitivity curve and a 15Hz lower frequency cutoff. A significant reduction in match is seen for even moderate spins $\chi \sim 0.3$ and low mass ratios $m_{bh}/m_{ns} \sim 4$. The approximants also begin to disagree for non-spinning systems as the mass ratio increases.

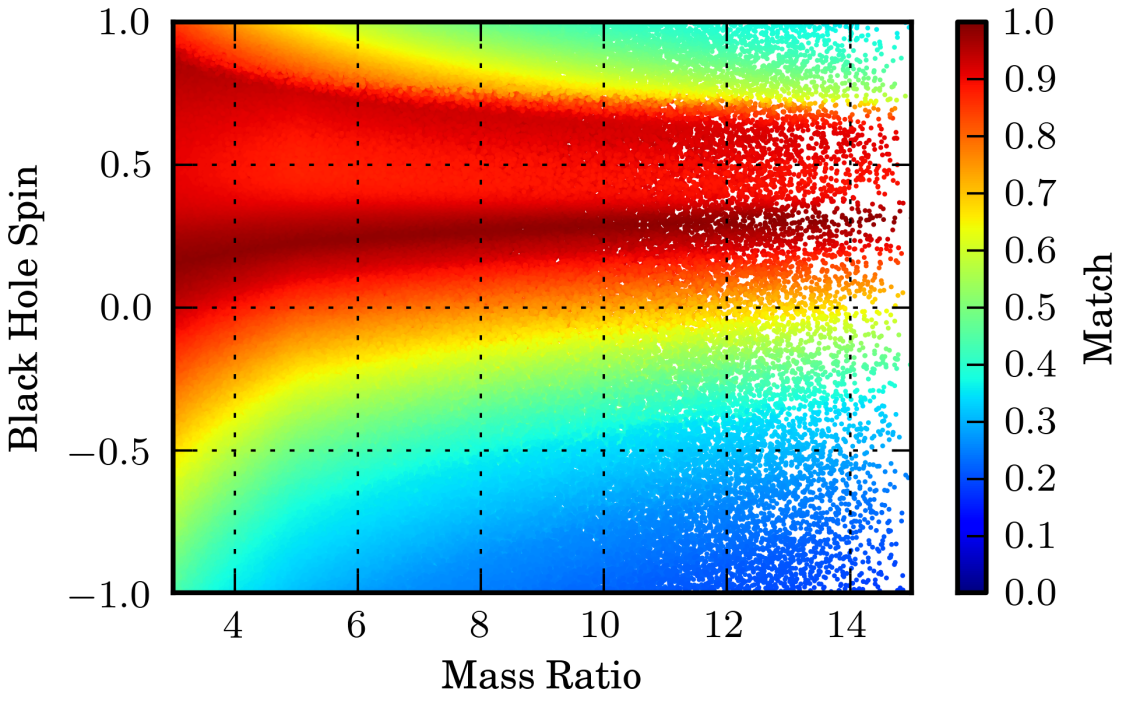

Figure 8: The match between the TaylorF2 and TaylorT4 approximants as a function of black hole spin and mass ratio. Both models include the next-to-next-to-leading spin-orbit (3.5PN) and spin-orbit tail terms (3.0PN). In comparison to Fig. 7, the additional terms have improved the agreement for moderately spinning aligned spin systems, however, the match is still ~ 0.8 for $\chi \sim 0.5$ at all mass ratios.

which the detector can see signals at a given false alarm rate, will decrease. Matched-filtering therefore relies on the accuracy of the models. We quantify the agreement between waveform families by computing the match, or *faithfulness* of the waveforms.

The *faithfulness* of representing a waveform from a given PN family with that of another is described by the match between the two waveforms when the same physical parameters are used as input to the models. As both models describe the same physical source, the match should be unity. Any deviation is due to the variation between models and the match gives the fractional loss in signal-to-noise ratio that will result.

In this section we compare the faithfulness between waveforms from different PN approximants where we choose the physical parameters to be consistent with NSBH sources. We also consider how the waveforms from the PN approximants compare to the waveforms from the SEOBNRv1 effective-one-body model [96]. Lastly, we consider the effect of including the spin-related terms at only partially derived orders. We model the sensitivity of second generation gravitational-wave detectors with the aLIGO zero-detuned, high-power sensitivity curve [108]. For this study we use a lower frequency cutoff of 15Hz since it is not expected that detectors will have significant sensitivity below this frequency. We consider the effect of increasing this low-frequency cutoff to simulate early aLIGO sensitivities in Sec. 5.7.

In Fig. 7, we examine the faithfulness of NSBH waveforms by computing the match between the TaylorF2 and TaylorT4 PN approximants. The TaylorT4 approximant was used to simulate NSBH binaries in LIGO's previous gravitational-wave searches, and the TaylorF2 family is used as the templates for detection [15]. In order to focus on the mismatches primarily due to phase differences between the models, the frequency cutoff of the TaylorF2 waveform is made to agree with the ending frequency of the TaylorT4 waveform. We see that the agreement between the two models is primarily influenced by the magnitude of the black hole's spin, and secondarily by the mass ratio. There is a noticeable drop in match at higher mass ratios, even when the spin of the black hole is zero. As expected, the best agreement is seen when the black hole's spin is small and the black hole and neutron star have comparable masses. However, this plot shows that there is a *substantial* disagreement between these approximants for even moderately low black hole spins ($\chi \sim 0.3$), which increases as the spin of the black hole increases. We note that the effect on the match due to the

spin of the neutron star is negligible in all areas. In Fig. 8 we compare the TaylorF2 and TaylorT4 models, with the inclusion of the spin-orbit tail (3.0PN) and next-to-next-to-leading spin-orbit (3.5PN) corrections recently computed in Refs. [126, 127]. In comparison to Fig. 7, the agreement is improved for aligned spins with moderate magnitudes. However, these approximants maintain a poor level of overall agreement, with matches of only ~ 0.8 at $\chi \sim 0.5$ for all mass ratios, and even lower matches for anti-aligned systems. Figs. 9 and 10 compare the TaylorT2 and TaylorT4 approximants with and without these additional spin terms. We see that TaylorT4 is especially sensitive to the additional corrections. In both cases, however, we note that the additional terms have caused a significant change in the waveforms, as indicated by the low matches, demonstrating that the expansion has not yet sufficiently converged to produce reliable waveforms for parameter estimation.

In Fig. 11 we compare the SEOBNRv1 model to the PN models TaylorF2 and TaylorT4. Since the SEOBNRv1 model is not valid for large values of χ [96] we restrict $\chi < 0.6$ and only report matches below this limit. We see that, similar to the comparison between TaylorF2 and TaylorT4, these models also have large mismatches when the spin of the black hole is nonzero. The large discrepancy between the waveform families indicates that higher order PN correction terms are required. This may also pose significant problems for parameter estimation of NSBH sources.

5.3 The TaylorR2F4 approximant

In the previous section, we found a surprisingly large disagreement between the TaylorF2 and TaylorT4 PN approximants when compared with waveform parameters appropriate for NSBH systems. We would like to distinguish how much of this is due to differences between time domain and frequency domain approximants, and how much of this is due to differences between the formulation of the two PN families. This can easily be performed for the TaylorF2 and TaylorT2 approximants, however we need to construct an equivalent frequency domain version of TaylorT4 to complete the comparison.

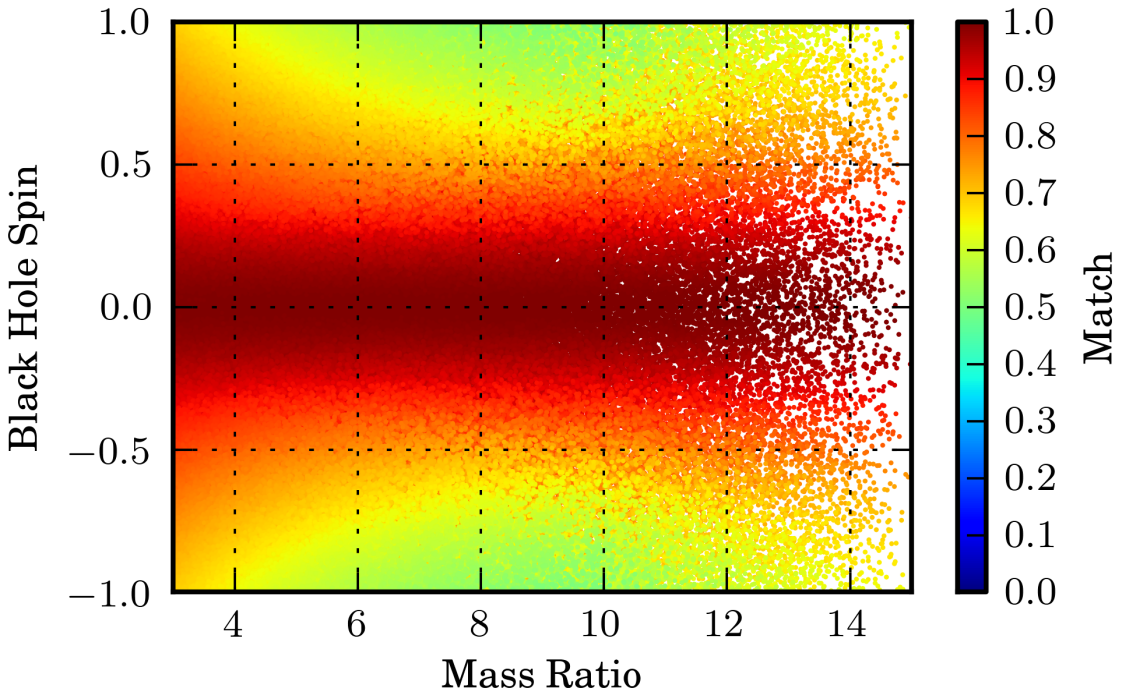

Figure 9: The match between TaylorF2 with 2.5PN spin corrections and TaylorF2 including the next-to-next-to-leading spin-orbit (3.5PN) and spin-orbit tail terms (3.0PN), as a function of the spin of the black hole and the mass ratio of the system. Matches are calculated using the the aLIGO zero-detuned, high-power sensitivity curve and a 15Hz lower frequency cutoff. Although there is agreement where the spins are low $\chi < 0.2$, the match quickly drops as the spin of the black hole increases, so that the match is already ~ 0.7 for $\chi \sim 0.5$.

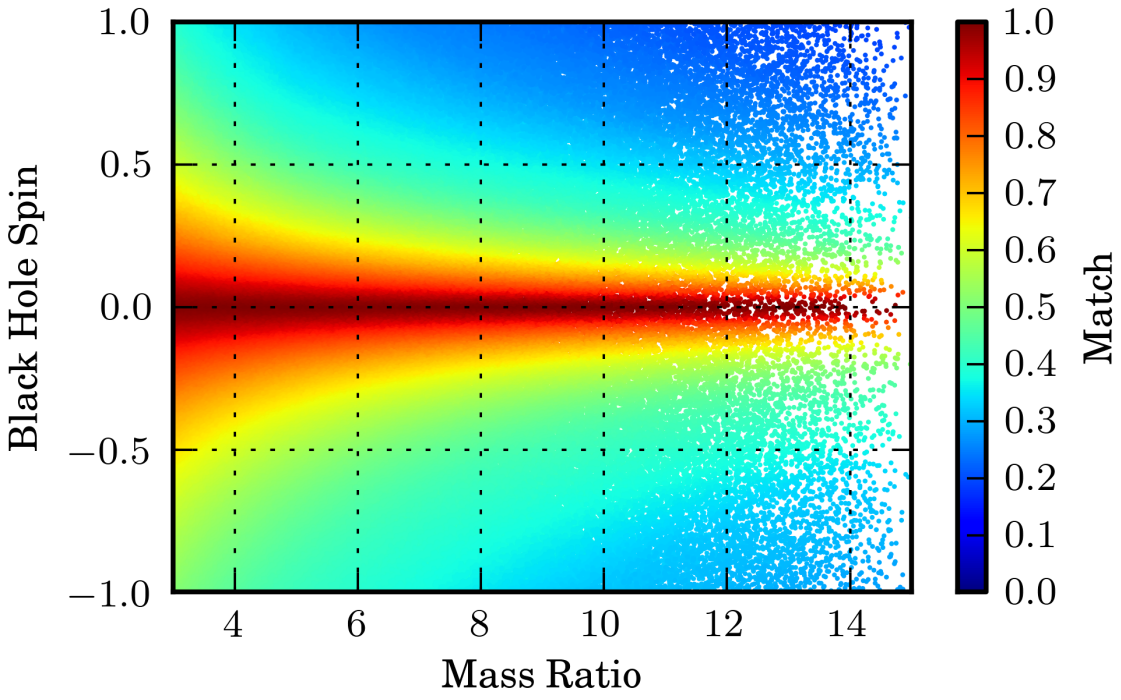

Figure 10: The match between TaylorT4 with 2.5PN spin corrections and TaylorT4 including the next-to-next-to-leading spin-orbit (3.5PN) and spin-orbit tail terms (3.0PN), as a function of the spin of the black hole and the mass ratio of the system. Matches are calculated using the the aLIGO zero-detuned, high-power sensitivity curve and a 15Hz lower frequency cutoff. In comparison to Fig. 9, the approximant is more noticeably changed by the additional terms. For a mass ratio of 8, the match has already fallen to ~ 0.7 for $\chi \sim 0.15$.

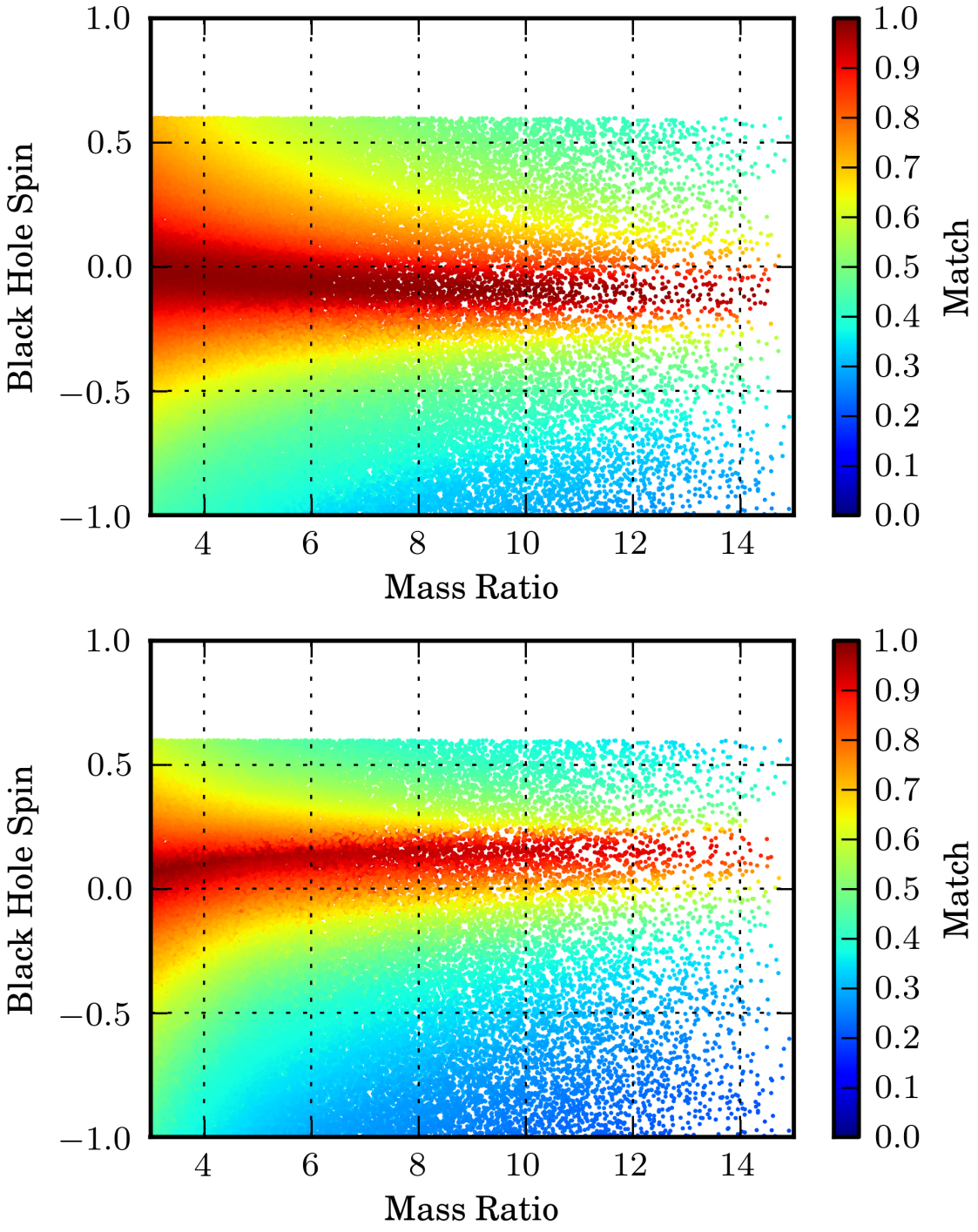

Figure 11: The match between the TaylorF2 (left) or TaylorT4 (right) and SEOBNRv1 approximants. Spin corrections for the PN approximants are included up to 2.5PN. Matches are calculated using the the aLIGO zero-detuned, high-power sensitivity curve with a 15 Hz lower frequency cutoff. As in Fig. 7, there is a significant reduction in match where spin of the black hole is only moderate. Note, however, that the PN approximants have marginally better agreement with SEOBNRv1 than with each other.

By analogy with TaylorF1 and TaylorF2 [128, 29], TaylorF4 is obtained by numerically integrating the reciprocal of Eq. (3.9) in the frequency domain,

$$dt/dv = 1/A_k(v). \tag{5.1}$$

However, this does not elucidate the differences between the TaylorT4 and TaylorF2 approximants. Instead, we construct an analytical approximation to the TaylorF4 approximant, which we call TaylorR2F4, by expanding Eq. (5.1) in powers of v. In order to make this series finite, we truncate these additional terms at an order in v higher than the order where the PN expansion of the energy and flux were truncated,

$$\frac{dt}{dv} = \left[\frac{1}{A_k(v)}\right]_l = B_k(v) + R_{kl}(v) = C_{kl}(v). \tag{5.2}$$

Here $B_k(v)$ is the same as in the TaylorT2 approximant and $R_{kl}(v)$ are the terms from order v^{k+1} up to order v^l. It is important to note that this produces a power series that is identical to the TaylorF2 approximant up to the point where Eq. (3.12) was truncated. Thus, terms of higher order in v account for the differences between the TaylorT2 and TaylorT4 approximants.

In Sec. 5.4 we show that TaylorR2F4 agrees well with the TaylorT4 approximant when expanded to v^9 or v^{12}, which we shall see in the next section. As noted above, the second expansion in the TaylorR2F4 approximant is a different expansion than the PN expansion of the energy and flux. The Fourier phase for the TaylorR2F4 approximant can be obtained from Eq. (3.13) where $B_k(v)$ is replaced by $C_{kl}(v)$. This is given up to order v^N as

$$\psi_{\rm R2F4}(f) = \psi_{F2}(f) + \sum_{i=6}^{N}\sum_{j=0}^{N} \lambda_{i,j} f^{(i-5)/3} \log^j f, \tag{5.3}$$

where the form of these expressions up to $N = 12$ can be found in Appendix A.2.4. Because this approximant can be analytically expressed in the frequency domain, it can be generated relatively cheaply compared to TaylorT4. This means that it has the potential to be used where computational efficiency and a higher degree of agreement with TaylorT4 is desired. We note that the frequency-domain approximants are much faster than their time-domain counterparts, which must integrate differential

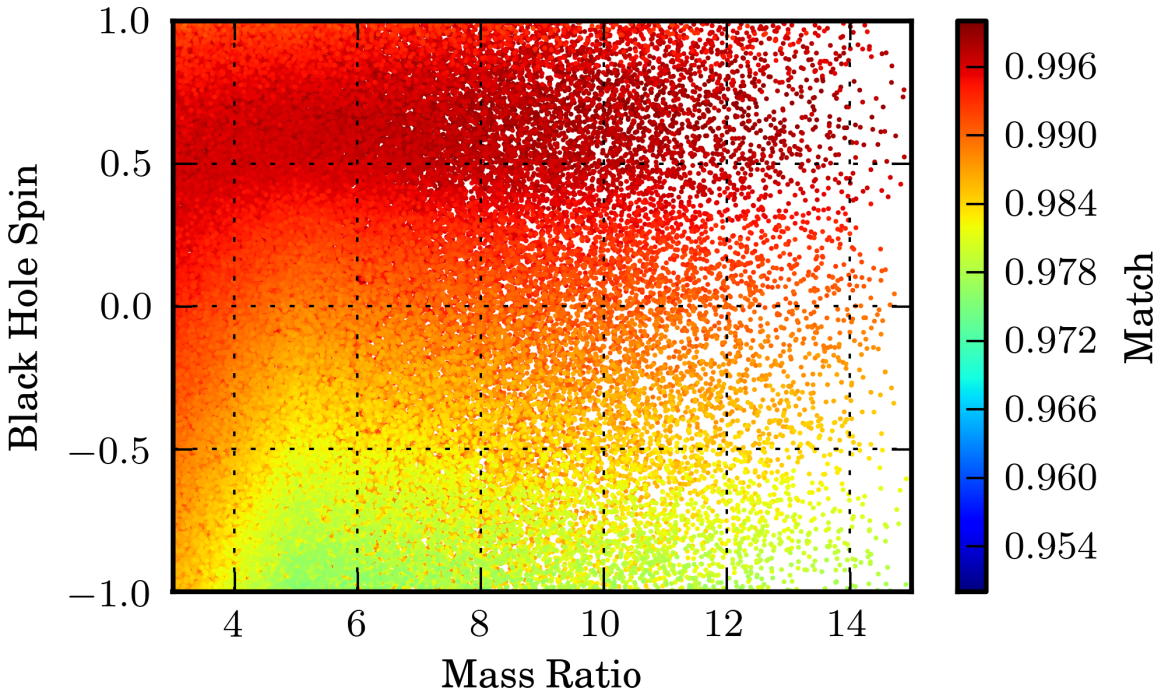

Figure 12: The match between TaylorF2 and TaylorT2. Both include spin corrections up to 2.5PN order. Matches are calculated using the the aLIGO zero-detuned, high-power sensitivity curve and a 15Hz lower frequency cutoff. We see that the F2 and T2 approximants largely agree. The discrepancy between the two approixmants can be reduced by expanding the frequency sweep of the TaylorF2 approximant's amplitude to higher PN orders. However, there is different Gibbs phenomena between the two approximants that will cause a discrepancy.

equations and perform a Fourier transform. Therefore, they are especially useful in computational problems which are waveform-generation limited, such as parameter estimation of signals [129].

5.4 Comparison of Frequency to Time Domain Approximants

In this section, we investigate to what extent the discrepancy between the waveform families that was demonstrated in Sec. 5.2 is due to the difference between expressing approximants in the frequency and time domain alone. We compare the new TaylorR2F4 approximant from Sec. 5.3, and TaylorF2, to their time domain equivalents.

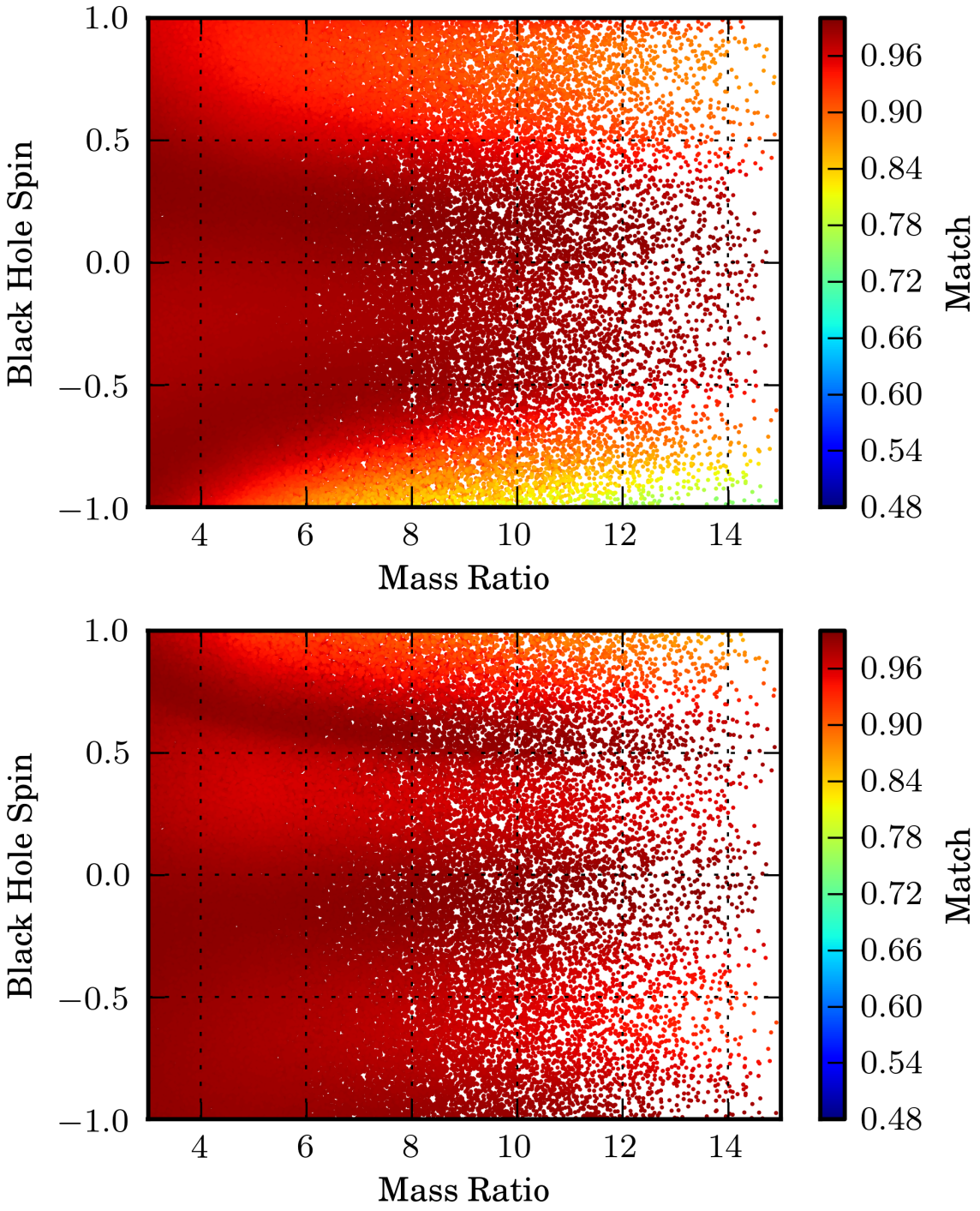

Figure 13: The match between TaylorT4 and TaylorR2F4. Both models include spin corrections up to 2.5 PN. TaylorR2F4 is re-expanded up to order v^9 (top) and v^{12} (bottom). Matches are calculated using the the aLIGO zero-detuned, high-power sensitivity curve and a 15Hz lower frequency cutoff. R2F4 and T4 have high agreement over a broad range of parameters, with some visible exceptions. Expanding up to order v^{12} has generally increased agreement with TaylorT4.

We find that TaylorF2 waveforms are a good representation of TaylorT2 waveforms, even when we consider waveforms from NSBH systems where the component objects are spinning. This can be seen in Fig. 12, which shows the match between the TaylorF2 and TaylorT2 models. In that figure, the ending frequency of both models is made to be the same, which is accomplished by terminating the TaylorF2 waveforms at the frequency where the generation of the equivalent TaylorT2 waveforms terminated. We find that the TaylorF2 and TaylorT2 waveforms agree to better than $\gtrsim 95.7\%$ for the entire region investigated. For systems where the black hole spin was positively aligned with the orbital angular momentum, the match is $\gtrsim 97.9\%$. The discrepancy between these two models is in part due to expanding to only Newtonian order the frequency sweep associated with the stationary phase approximation of the TaylorF2 approximant. In addition, part of the discrepancy results from Gibbs phenomena differences between the approximants. It is important to note that neither of these waveforms have termination conditions that are determined by the physical behavior of the inspiralling binary. The termination frequency only indicates the point at which the approximant is certainly no longer valid. The increased match for aligned spin waveforms is due to the higher frequency cutoff, which pushes the termination frequency out of the most sensitive part of the zero-detuned, high-power aLIGO sensitivity curve.

Fig. 13 shows a comparison between the TaylorR2F4 and TaylorT4 models. In that figure, the second expansion associated with the TaylorR2F4 model is extended to order v^9 (left) and v^{12} (right), and the ending frequency of both is that corresponding to the MECO. We show that the TaylorR2F4 model is adequate for a large range of parameters as a computationally inexpensive substitute for TaylorT4.

Since the mismatch between the TaylorF2 and TaylorT4 models is not due to differences between the time domain and frequency domain approximants, this indicates that the effective higher order PN terms used in the construction of TaylorR2F4, which are also intrinsically present in TaylorT4, are still significant. To obtain better agreement between the different PN approximants we consider, it is necessary to extend the PN expansions of the energy and flux equations to include unknown higher order terms, particularly ones that involve the spin of the objects.

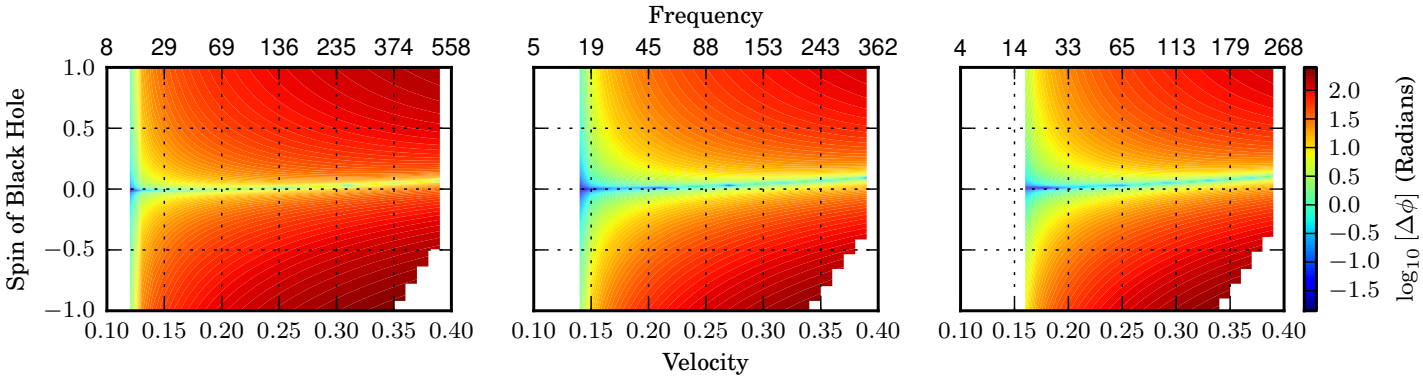

Figure 14: The accumulation of phase differences between TaylorT2 and TaylorT4, for systems with component masses (m_1, m_2) of $(1.4M_\odot, 6M_\odot)$ (left), $(1.4M_\odot, 10M_\odot)$ (center), and $(1.4M_\odot, 14M_\odot)$ (right). The approximants include spin terms up to 2.5PN. The calculation starts from the velocity corresponding to a gravitational-wave frequency of 15Hz, continues to the velocity on the horizontal axis, and reports the difference in accumulated gravitational-wave phase between the waveforms. The feature in the bottom right corner of each plot arises because the TaylorT2 approximant is no longer monotonic. Note that large phase differences accumulate at very low velocities $v \sim 0.2$ for even small black hole spins.

5.5 Accumulation of Phase Discrepancy

In the previous sections, we demonstrated that the two PN approximants, TaylorF2 and TaylorT4, and the SEOBNRv1 model are not faithful to each other. We also showed that this is not due to the differences between frequency and time domain waveforms. From the construction of the TaylorR2F4 approximant, we also demonstrated that the two PN families can be written in a way that is consistent up to the chosen PN order, but where TaylorR2F4 contains higher order in v corrections that account for the differences between the models. Since these are higher order corrections, they should start to become important to the orbital phasing only at high velocities, and thus high gravitational-wave frequencies. In this section we investigate where, for systems with parameters corresponding to NSBH binaries, the approximants diverge. We do this by examining the accumulation of phase as a function of orbital velocity and reporting the difference in the number of gravitational-wave cycles between different approximants.

In Fig. 14, we examine the difference in the accumulated phase between TaylorT2 and TaylorT4 for three example systems with component masses (m_1, m_2) of

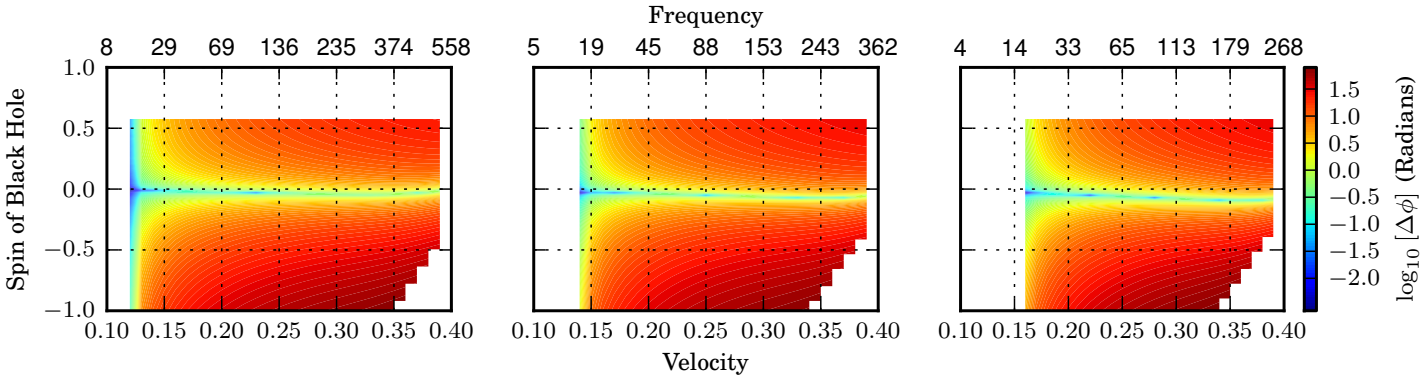

Figure 15: The accumulation of phase difference between TaylorT2 and SEOBNRv1, for systems with component masses (m_1, m_2) of $(6M_\odot, 1.4M_\odot)$ (left), $(10M_\odot, 1.4M_\odot)$ (center), and $(14M_\odot, 1.4M_\odot)$ (right). TaylorT2 includes spin terms up to 2.5PN. The calculation starts from the velocity corresponding to a gravitational-wave frequency of 15Hz, continues to the velocity on the horizontal axis, and reports the difference in accumulated gravitational-wave phase between the waveforms. The feature in the bottom right corner of each plot arises because the TaylorT2 approximant is no longer monotonic. As in Fig. 14, a large phase difference is accumulated at low velocities and small black hole spins.

$(6M_\odot, 1.4M_\odot)$, $(10M_\odot, 1.4M_\odot)$, and $(14M_\odot, 1.4M_\odot)$. We see that the phase difference between the two models quickly grows to tens of radians, even when the black hole spin magnitude is small. This is also true when comparing TaylorT2 and SEOBNRv1, as can be seen in Fig. 15. In the latter case, there is also a noticeable deviation away from the line of zero spin where for unknown reasons the two models diverge and subsequently converge.

5.6 Accumulation of mismatch

As gravitational-wave detectors are not directly sensitive to phase differences alone, it is useful to compute how the match, which incorporates the sensitivity of a gravitational-wave detector, changes as a function of the upper frequency cutoff used for the calculation. In this section we demonstrate at which frequencies and corresponding velocities the match between waveform families drops. To do so, we define an inner product between waveforms that is a function of the upper frequency cutoff. This inner product is then used in the match calculation of Eq. (2.3).

In Fig. 16, we examine the match between TaylorF2 and TaylorT4, integrated from

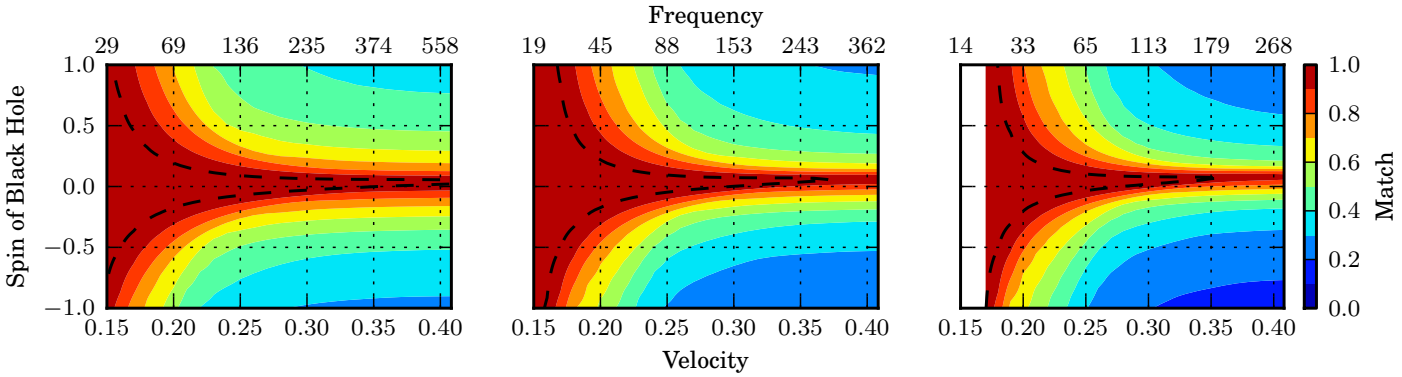

Figure 16: The match between TaylorF2 and TaylorT4 integrated from 15 Hz up to the designated frequency for systems with component masses (m_1, m_2) of $(1.4M_\odot, 6M_\odot)$ (top), $(1.4M_\odot, 10M_\odot)$ (center), and $(1.4M_\odot, 14M_\odot)$ (bottom). Both approximants include spin corrections up to 2.5PN. Matches are calculated using the the aLIGO zero-detuned, high-power sensitivity curve. A contour at a match of 0.97 is indicated by the dotted line. The match follows the general features seen in the phase difference comparison of Fig. 14 and drops significantly, even at relatively low velocities. For the $(1.4M_\odot, 6M_\odot)$ system with a black hole spin $\chi = 0.5$, the match has already dropped to ~ 0.5 at a velocity of only ~ 0.25.

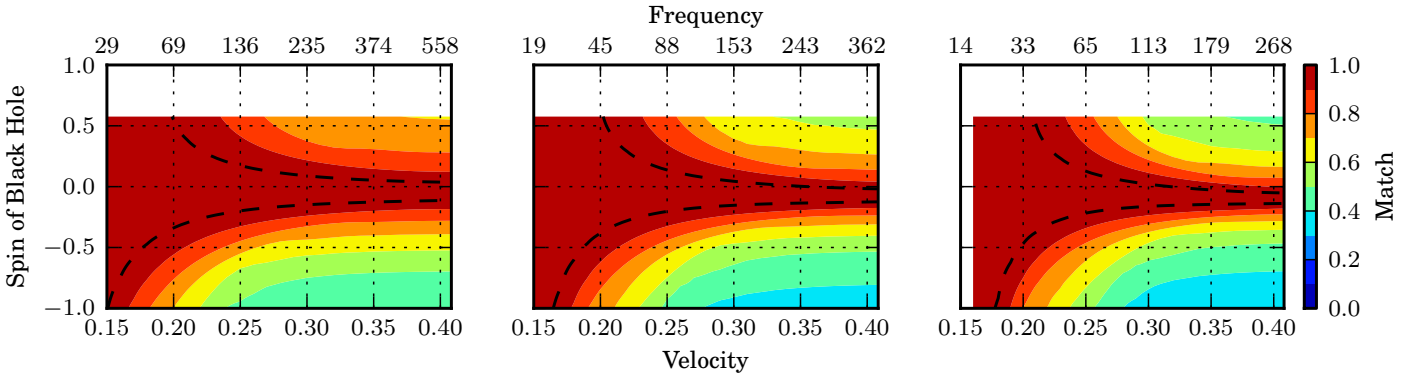

Figure 17: The match between the TaylorF2 and SEOBNRv1 models integrated from 15 Hz up to the designated frequency for systems with component masses (m_1, m_2) of $(6M_\odot, 1.4M_\odot)$ (left), $(10M_\odot, 1.4M_\odot)$ (center), and $(14M_\odot, 1.4M_\odot)$ (right). TaylorF2 includes spin corrections up to 2.5PN. Matches are calculated using the the aLIGO zero-detuned, high-power sensitivity curve. A contour at a match of 0.97 is indicated by the dotted line. We note that, although the match is marginally improved compared to Fig. 16, there are still large disagreements at velocities as low as 0.25.

a lower frequency cutoff of 15 Hz up to the upper frequency cutoff indicated on the horizontal axis. This is compared for the same three example systems as in Sec. 5.5. The match is shown across the range of allowable values of the black hole spin and the neutron star spin is set to zero. We see that the match drops precipitously even at low velocities and relatively modest spin magnitudes. For example, for a system with $m_1 = 6M_\odot$, $m_2 = 1.4M_\odot$, and a dimensionless spin of 0.5 for the black hole, the match drops below 0.7 at a velocity of only 0.23. The loss in match is more pronounced with increasing mass ratio.

In Fig. 17, we examine the match between TaylorF2 and SEOBNRv1, integrated from a lower frequency cutoff of 15Hz up to the upper frequency cutoff indicated on the horizontal axis. Again, the match drops for large spin magnitudes at relatively low velocities, although, just as the TaylorF2 approximant has shown better matches with the SEOBNRv1 approximant than with the TaylorT4 approximant, this occurs at somewhat higher velocities. This shows clearly that significant portions of the loss in match seen in Sec. 5.2 occurs at unexpectedly low velocities.

5.7 Detection searches and Early aLIGO

In the previous sections, we have demonstrated a substantial loss in match between different PN and EOB models of NSBH binaries. These discrepancies will cause substantial biases in attempts to measure the parameters of detected systems with aLIGO. However, when detecting systems the *fitting factor*, rather than the match, is the quantity that is used to assess the effectualness of a search [97]. The fitting factor maximizes the match between a signal and a bank of templates designed to capture e.g. 97% of the optimal signal-to-noise ratio. The template bank is constructed to be valid for the same range of masses and spins used throughout this chapter and detailed in Sec 5.1. Discrepancies in match due to differing approximants may be compensated for by allowing a waveform to match to a template with shifted parameters. Figs. 18 and 19 show the fitting factor of a TaylorF2 aligned spin template bank when used to detect TaylorT4 waveforms. Fig. 18 shows the distribution of fittings factors for approximants that include up to the 2.5PN spin corrections. Fig. 19 demonstrates the effect of adding the higher order 3.0PN spin-orbit tail and 3.5PN

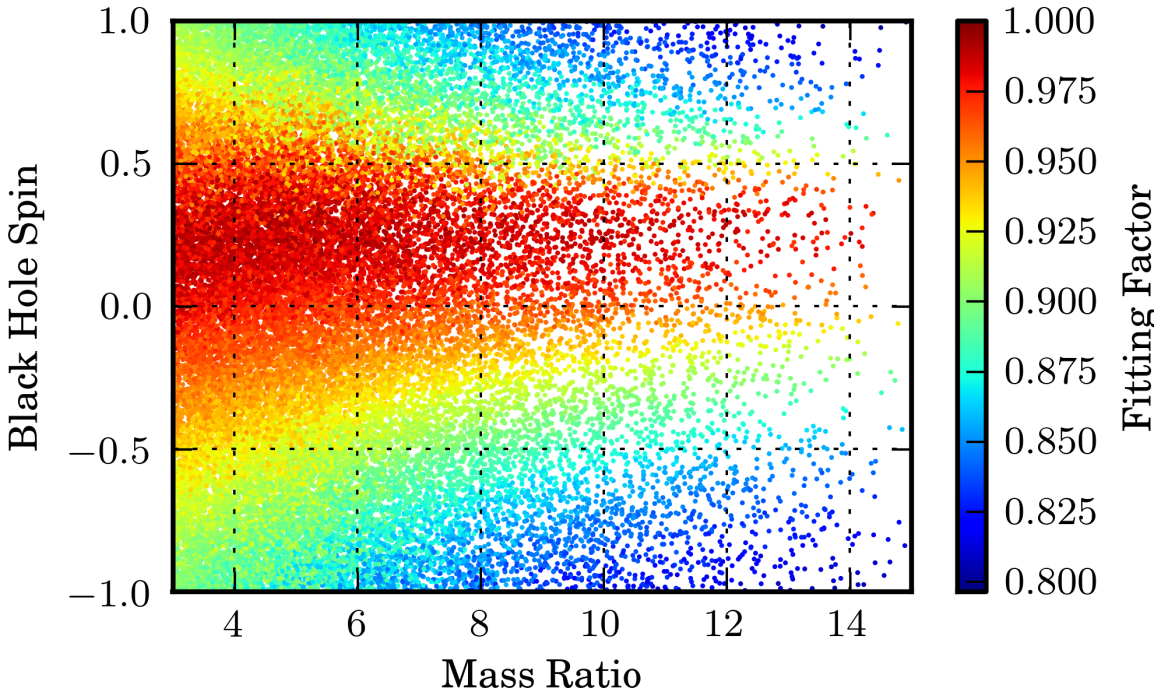

Figure 18: The fitting factor between the TaylorF2 and TaylorT4 approximants as a function of the spin of the black hole and the mass ratio of the system, when maximizing the match over a bank of TaylorF2 waveforms. All approximants include spin corrections up to 2.5PN. Matches are calculated using the the aLIGO zero-detuned, high-power sensitivity curve and a 15Hz lower frequency cutoff. In comparison to the match of these approximants shown in Fig. 7, we see that while allowing for the maximization over a bank of templates has improved the overall agreement, it is unable to entirely make up for the poor match.

spin-orbit corrections. Construction of these aligned spin banks use the method introduced in Ref. [55] and is described in more detail in Ref. [123]. There is substantial improvement in the fitting factors of aligned spin systems when adding the higher order spin corrections, but no improvement for anti-aligned spin systems. Although the loss in fitting factor is not as significant as the loss in match shown in Figs. 7 and 8, aLIGO NSBH searches will isncur a substantial loss in signal-to-noise ratio for anti-aligned spins, if the accuracy of NSBH waveforms is not improved.

In the previous sections we have modeled the sensitivity of aLIGO with the zero-detuned, high-power sensitivity curve [108]. Early commissioning scenarios for aLIGO indicate that observations will begin with less sensitivity in the 10–40 Hz region [17].

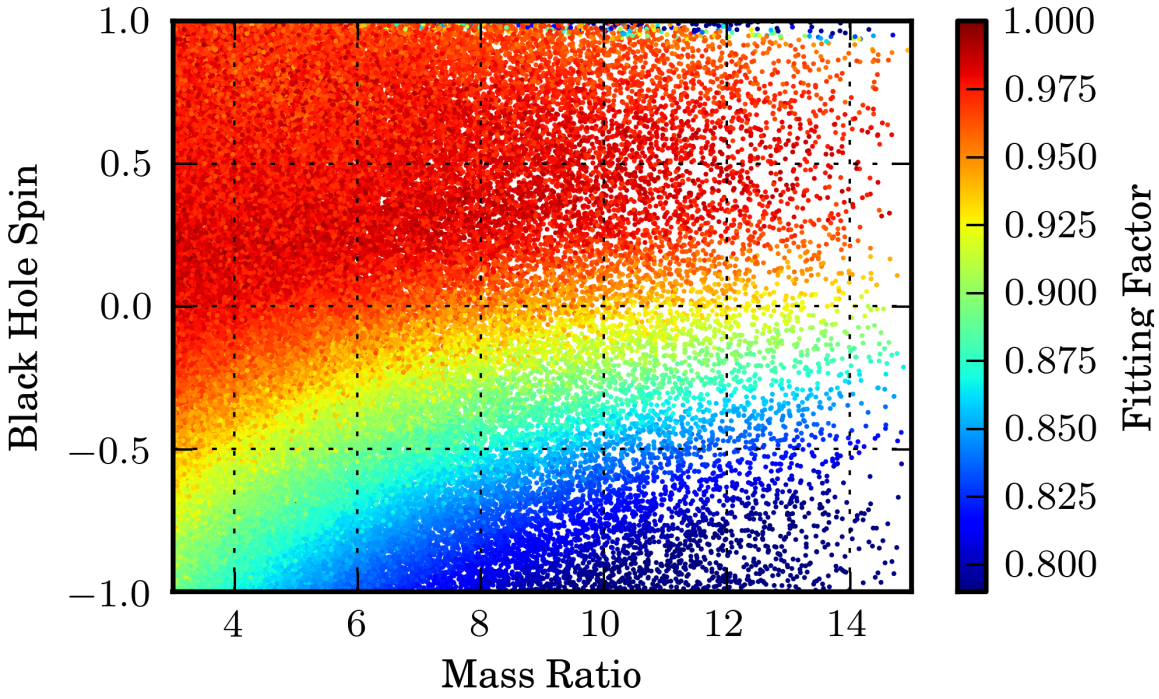

Figure 19: The fitting factor between the TaylorF2 and TaylorT4 approximants as a function of the spin of the black hole and the mass ratio of the system, when maximizing the match over a bank of TaylorF2 waveforms. All approximants include the 3.5PN spin-orbit and 3.0PN spin-orbit tail corrections. Matches are calculated using the the aLIGO zero-detuned, high-power sensitivity curve and a 15Hz lower frequency cutoff. In comparison to the fitting factors shown in Fig. 18, we see that adding the higher order spin corrections has resulted in substantially improved fitting factors for systems where the spin is aligned with the orbital angular momentum. There is no improvement for anti-aligned systems.

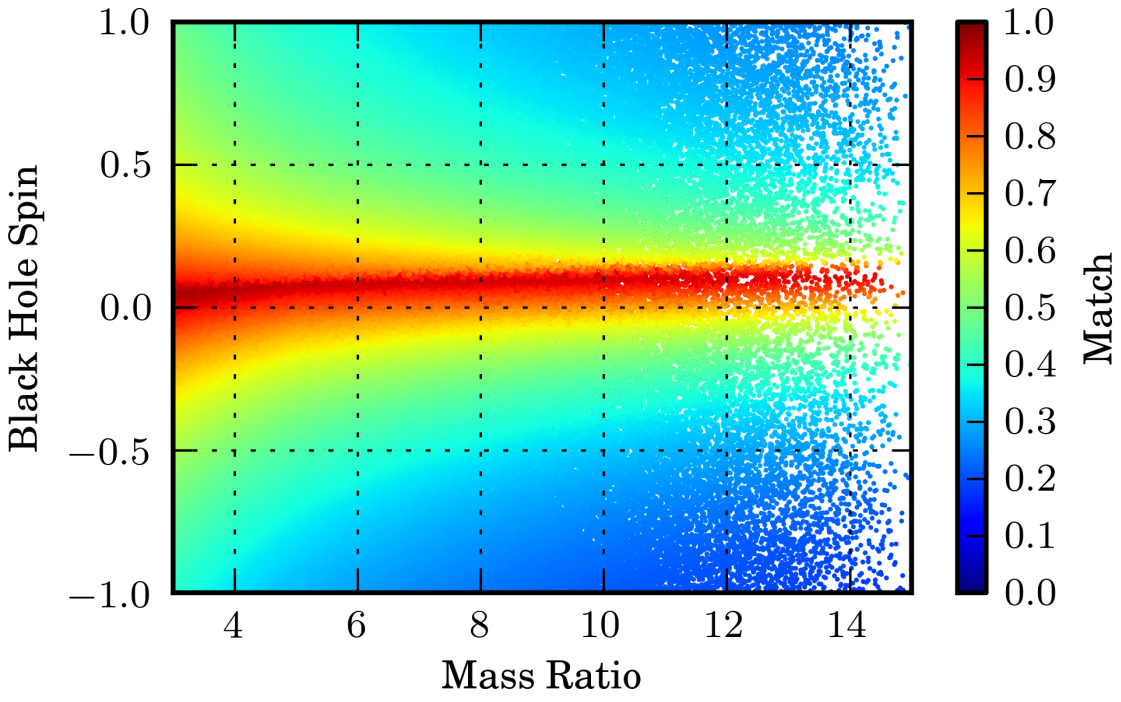

Figure 20: The match between TaylorF2 and TaylorT4 as a function of the spin of the black hole and the mass ratio of the system. The approximants include spin corrections up to 2.5PN. Matches are calculated using a 30Hz lower frequency cutoff to approximate the sensitivity of an early aLIGO detector. In comparison to Fig. 7, which uses a 15Hz lower frequency cutoff, there is only a negligible improvement in match. Matches remain low at moderate black hole spins $\chi \sim 0.3$.

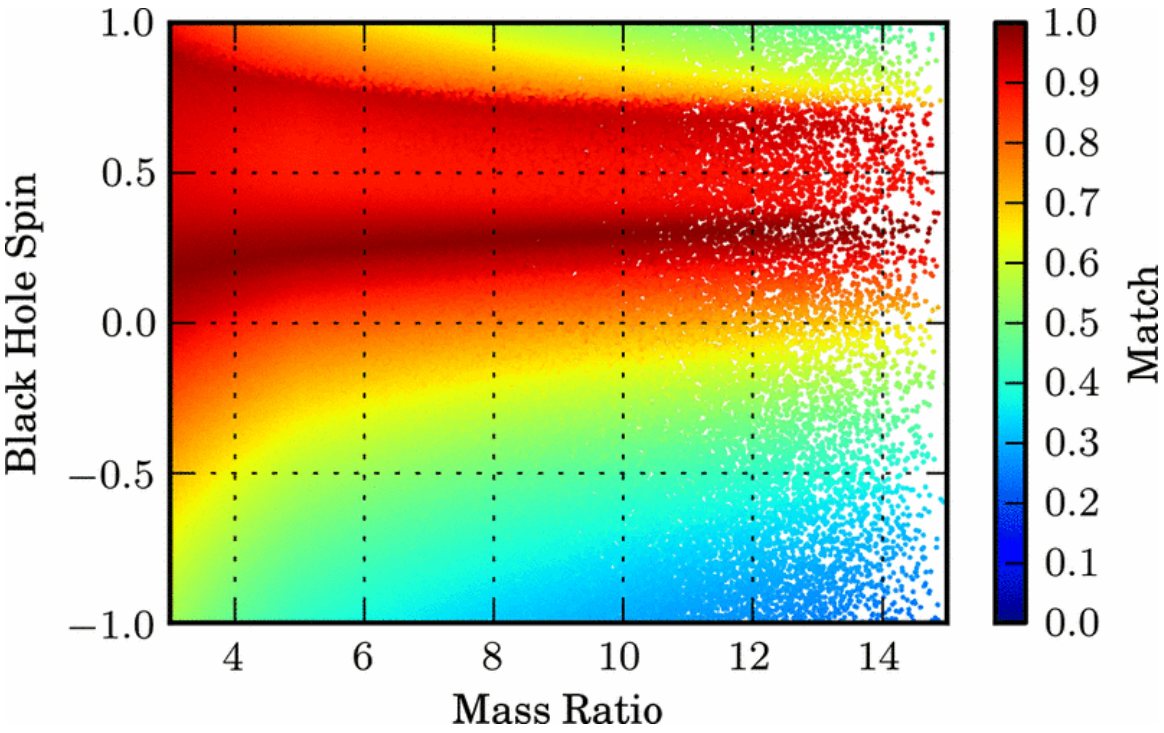

Figure 21: The match TaylorF2 and TaylorT4 approximants, with the 3.5PN spin-orbit and 3.0PN spin-orbit tail corrections included, as a function of the spin of the black hole and the mass ratio of the system. The approximants include only the nown spin terms up to 2.5PN. Matches are calculated using a 30Hz lower frequency cutoff to approximate the sensitivity of the early aLIGO detector. In comparison to Fig. 8, which uses a 15Hz lower frequency cutoff, there is only a negligible improvement in match.

We investigate if the substantial disagreement found between TaylorF2 and TaylorT4 is still present for early detector sensitives by a instead using a lower frequency cutoff of 30 Hz.

In Fig. 20 and 21, we show the faithfulness between the TaylorF2 and TaylorT4 approximants that include only the complete 2.5 PN and partial 3.5PN spin-related corrections, respectively. We see that there is no significant improvement in the faithfulness of the approximants, and so additional spin corrections are desirable even for early detector scenarios.

5.8 Conclusions

We have found that there is significant disagreement between NSBH waveforms modelled with the TaylorT2, TaylorT4, and SEOBNRv1 approximants. This will pose problems for the construction of optimal NSBH detection searches, potentially reducing the event rate, and may cause significant biases in the parameter measurement of detected signals.

The discrepancies are not accounted for by the differences between frequency and time domain waveforms and start at fairly low ($v \sim 0.2$) orbital velocities. Since the discrepancies in the approximants result from how the PN expansions of the energy and flux are combined and truncated, we conclude that the calculation of higher order PN terms is required to increase the faithfulness of these approximants, and more importantly, to improve the ability to detect NSBH coalescences. The discrepancies between approximants are significantly smaller when the spin of the black hole is close to zero, which further motivates the calculation of the PN terms associated with the spin of the objects beyond those known completely up to 2.5PN order and partially up to 3.5PN. Therefore, additional work is needed to verify the validity of waveform models used for NSBH searches. We also note that we have only compared different waveform families under the assumption that the spins of the component objects are (anti-)aligned with the orbital angular momentum of the system. It is expected that generic NSBH systems will not be limited to aligned spins, but may instead be more isotropically oriented. This could lead to an additional source of discrepancy between our models and the true signal, which would result in an additional loss in the detection rate of sources.

Chapter 6

Effects of Spin on Neutron Star – Black Hole Searches

6.1 Introduction

In this chapter we investigate the effect of ignoring spin on optimal (matched-filter) searches for NSBH binaries with aLIGO. The gravitational waves radiated by NSBH binaries are expected to be significantly affected by the black hole's angular momentum (spin), which is expected to be comparable to the orbital angular momentum of the binary [103, 71, 70, 72]. Spin-orbit coupling changes the gravitational waveform of the binary's inspiral and merger and can cause the orbital plane of the binary to precess [71]. Coupling between the black hole spin and the neutron star spin [72], the quadrupole-monopole interaction due to the spheroidal deformation of spinning black holes and neutron stars [130] and the "self-spin" interaction [110] will also effect the gravitational waveform emitted during a NSBH binary inspiral. The resulting changes in the waveform observed by aLIGO carry a great deal of information about the dynamics of the binary. However, optimal searches of aLIGO data must incorporate this dynamics into their waveform models to avoid a reduction in sensitivity and hence the rate of detected events.

Compact binary mergers in quasi-circular orbit are described by 15 parameters; the masses, spin magnitude, spin orientations, source orientation, sky location, distance and time and phase of coalescence [40, 131]. Matched-filter searches must be capable of detecting binary mergers regardless of the parameters of the system. For

non-precessing systems and restricting to the dominant gravitational wave mode, the extrinsic parameters - source orientation, sky location, distance and coalescence phase - only effect the overall phase and amplitude of the observed gravitational wave system. Therefore, it is possible to analytically maximize over these extrinsic parameters [48].

When precessing systems are considered as template waveforms, the matched-filter search becomes more complex. In this case the extrinsic parameters no longer enter as overall phase and amplitude shifts in the waveform [71]. Previous work has been conducted to explore the affect of precession on gravitational-wave searches and to develop methods to detect precessing systems [97, 87, 132, 133, 134, 135, 136, 137, 11, 138, 139, 140, 141, 114, 142]. However, these searches, when applied to Initial LIGO and Virgo data, have not shown an increase in efficiency with respect to non-precessing searches [138]. This is because the filtering codes allow for increased, and unphysical, freedom when maximizing over extrinsic parameters and because no suitable method to distinguish gravitational wave signals from non-Gaussian instrumental noise has been developed for these searches. Therefore, searches for NSBH binaries in data from LIGO and Virgo's most recent science runs ignored spin affects and used quasi-circular templates to search for NSBH binaries [12, 13, 14, 15].

The majority of previous work considered the Initial LIGO detectors. aLIGO will have a substantially different noise curve than Initial LIGO [17]. Conclusions drawn using the Initial LIGO sensitivity curve may not hold when considering aLIGO. A previous study considering aLIGO sensitivity curves has suggested that it may be possible to detect generic, precessing NSBH binaries using aligned-spin waveforms [141]. However, other studies have suggested that precession may significantly change the gravitational waveform seen by aLIGO, requiring templates that explicitly capture this effect [114].

We demonstrate that the quasi-circular templates used in Initial LIGO will reduce the detection rate by $33-37\%$ for NSBH systems with masses uniformly distributed between $(10 \pm 0.5, 1.4 \pm 0.05) M_{\odot}$, an isotropic black hole spin distribution and spin magnitude uniformly distributed between 0 and 1. Over a wider range of uniformly distributed masses, $(3-15, 1-3) M_{\odot}$, we find that the detection rate would be reduced by $31-36\%$. In both cases this loss in detection rate is compared against a template bank where every signal is matched exactly by the bank of filters. The loss in event

rate is greatest for NSBH binaries with large black-hole spins and large mass ratios. The range quoted in both measurements is due to uncertainty in the waveform models used to simulate NSBH gravitational-wave signals. These values also strongly depend on the signal distributions that we selected. If nature does not provide a uniform distribution of masses and an isotropic distribution of masses then these averaged values will change. To account for this, we explore the ability to recover NSBH signals as a function of their spins and masses in section 6.7.

We expand upon the method we introduced in [55] and construct a bank of templates for aligned-spin NSBH binaries. We demonstrate that this template bank is effectual for recovering the population of aligned-spin NSBH systems that it is designed to detect. We assess the ability of an aligned-spin template bank to detect a population of generic NSBH binaries where the black hole spin is not constrained to be parallel to the orbital angular momentum. We find using the aligned-spin bank will reduce the detection rate by $17-23\%$ compared to using a bank where every signal matches exactly with one of the filter waveforms when searching for NSBH waveforms with masses $(3-15, 1-3)M_{\odot}$. When restricting the mass range to $(10 \pm 0.5, 1.4 \pm 0.05)M_{\odot}$ we find that the detection rate is reduced by $26-33\%$. We find that there are regions of the NSBH signal parameter space where precession effects cause a significant reduction in signal-to-noise ratio. These regions are those where the black hole's angular momentum is large in comparison to the orbital angular momentum. We suggest possible methods for constructing searches that recover these systems. By considering several NSBH waveform models, we demonstrate that our results are robust against possible errors in the post-Newtonian phasing for NSBH binaries.

There has been a great deal of recent work focused on numerically modelling the merger of a black hole and a neutron star [143, 144, 145, 146, 147]. However, there is not currently any widely available waveform model that includes both the full evolution of a NSBH coalescence *and* includes precessional effects over the full parameter space that we consider. Therefore, in this work we have restricted ourselves to considering post-Newtonian, inspiral-only signal waveforms and consider only the case of two point particles. If a full inspiral-merger-ringdown, precessing NSBH waveform model becomes available, it would be informative to compare results with that model against those presented here. However, in this work the black hole mass is restricted

to be less than $15M_\odot$. It has been demonstrated that inspiral-only template banks recover $> 95\%$ of the signal power of numerically modelled $(3+15)M_\odot$ binary black hole waveforms [30, 124]. It has also been demonstrated that non-spinning NSBH mergers with total mass $\sim 10M_\odot$ are indistinguishable from binary black holes (BBH) mergers with the same masses [147]. With these observations we expect that our results are qualitatively valid in the parameter space we study.

The layout of this work is as follows. In Sec. 6.2 we describe the set of NSBH systems that we use to assess the performance of our template banks. In Sec. 6.3 we discuss the waveform models that we use in our simulations. In Sec. 6.4 we discuss the methods we use to test the template banks. In Sec. 6.5 we describe the method to create banks of aligned-spin filter waveforms. In Sec. 6.6 we validate our template banks against the aligned-spin signal models they are constructed to detect. In Sec. 6.7 we assess the performance of non-spinning template banks to search for generic NSBH signals and assess the performance of aligned-spin template banks to detect the same signals.

6.2 A population of NSBH binaries

In this section, we describe our large simulated set of NSBH binaries. This is used to assess the loss in detection rate when using non-spinning and aligned-spin template banks to search for generic NSBH binaries. To construct this set we incorporate current astrophysical knowledge to choose the distribution of masses and spins. However, this astrophysical knowledge is limited due to the fact that no NSBH binaries have been directly observed. Nevertheless, both NSs and BHs have been observed in other binary systems, and these observations can be used to make inferences about the mass and spin distributions that might be expected in NSBH binaries. We begin by giving the distributions that we use in this work, before describing the astrophysical knowledge that motivated these choices.

We simulate 100,000 NSBH binaries with parameters drawn from the following distribution. We choose to use a uniform range of 3 to 15 solar masses for the black holes in our NSBH signal population. This is partly motivated by the considerations of the observed populations, and partly by our concern of the validity of inspiral-only, point particle waveform models for high-mass NSBH systems. Observations of

black hole spin have found spin values that span the minimum and maximum possible values for Kerr black holes [85], therefore we use a uniform black-hole spin distribution between 0 and 1. While a conservative choice, we choose to use a uniform mass distribution between 1 and 3 solar masses for the NSs in our NSBH signal population. The black hole dimensionless spin magnitude is chosen uniformly between 0 and 1 and the neutron star dimensionless spin magnitude is chosen uniformly between 0 and 0.05. The initial spin orientation for both bodies, the source orientation and the sky location are all chosen from an isotropic distribution.

6.3 Waveform models

Matched-filter searches require an accurate model of compact binary mergers. In this work we wish to investigate the effects of spin, especially spin-induced precession, while understanding and mitigating any bias in our results due to the choice of waveform approximant. We therefore run all our simulations using two waveform approximants; TaylorT2 [128] and TaylorT4 [87].

PN waveforms, such as TaylorT2 and TaylorT4 are constructed by solving the PN equations of motion to obtain the binary orbits. For terms involving the orbital contribution, the center-of-mass energy and gravitational wave flux are known to 3.5PN order.[119, 41, 42, 89, 120, 46]. For terms involving the spin of the objects, the expansions of the energy and flux are complete to 2.5 PN order.[70, 72, 111]. In recent work, terms relating to the coupling between the component spins and the orbit have also been computed to 3.5 PN order [127, 117]. We choose not to use these terms in this work because terms relating to the spin(1)-spin(2), quadrupole-monopole and self-spin contributions are not yet known at 3 PN order, so we restrict the spin-related terms to 2.5 PN where these terms are fully known. We do not expect these terms to change the main conclusions of the work as these additional phase evolution terms will have little effect on the precessional evolution of a system.

6.4 Method for assessing the performance of NSBH searches

In this section we describe the methods we use to assess the efficiency of template banks and the terminology that we will use in the rest of this work. In previous

searches of LIGO and Virgo data using non-spinning template banks, the banks of signals were constructed so that the fitting factor would be greater than 0.97 for any non-spinning signal within the parameter space [59]. This was chosen as a balance between detection efficiency and computational cost. We also construct our aligned-spinning banks with this criterion.

When a set of fitting factors have been calculated one can quote an "average fitting factor" by taking the mean over all the values

$$\mathrm{FF}_{\mathrm{av}} = \langle \mathrm{FF} \rangle \,, \tag{6.1}$$

where $\langle X \rangle$ denotes the mean average of X. However, this measure can often be misleading. The aLIGO detectors have a direction-dependent and orientation-dependent sensitivity. Systems that are poorly aligned with respect to the detector may not have sufficient SNR to be detected, regardless of the fitting factor. To account for this we make use of the "effective fitting factor", first defined in [87] as

$$\mathrm{FF}_{\mathrm{eff}} = \left(\frac{\langle \mathrm{FF}^3 \sigma_i^3 \rangle}{\langle \sigma_i^3 \rangle} \right)^{1/3} . \tag{6.2}$$

Here $\sigma_i = \sqrt{(h_i|h_i)}$, which describes the optimal SNR of h_i. The cube of the effective fitting factor gives, above an arbitrary SNR threshold, the ratio between the fraction of NSBH signals that would be recovered with the discrete template bank that was used and a theoretical continuous template bank that would recover 100% of signal power for *any* NSBH waveform. We therefore define the "signal recovery fraction" as $\mathrm{FF}^3_{\mathrm{eff}}$.

6.5 Algorithm for constructing template banks of aligned-spin NSBH waveforms

In [55] we proposed a method for generating a geometrically-placed bank of aligned-spin systems that can be used to search for BNS systems in the advanced detector era. In this section we adapt the methods presented in that work to the case of NSBH systems and describe how to generate template banks that can recover aligned-spin NSBH waveforms. These banks are applicable for waveforms modeled using either

the TaylorT2 approximant or the TaylorT4 approximant.

Our geometrical placement method is not specific to the BNS area of the parameter space. However, some modifications to the method were necessary when placing a template bank of NSBH waveforms. Our BNS aligned-spin template bank, as described in [55], was given in terms of the positions of the points in the 8-dimensional Euclidean parameter space, ξ_i. These points do not correspond directly to physical masses and spins. For this study we want to use time domain template families and therefore we must translate the bank into physical parameters. However, if a set of ξ_i values is given it will, in general, not be possible to find a set of masses and spins that give the exact ξ_i values. As templates are normally placed in a 2-dimensional lattice, we need only to find a physical point that has the corresponding values of ξ_1 and ξ_2 and *any* value of the other ξ_i values that correspond to a waveform within the physically allowed manifold. For some cases where a 2-dimensional lattice is not sufficient to cover the space we will also specify values of ξ_3 and ξ_4. We use a brute force method to find a physical solution that is sufficiently close to the desired point using a numerical solution, which has the downside of being computationally inefficient.

The TaylorF2 metric can be used to place a bank of waveforms modeled with the TaylorT2 approximant. However, we also require that our template placement algorithm place a bank of waveforms that can detect aligned-spin signals modelled using TaylorT4 with no more loss in SNR than that specified by the minimal match of the bank. This will allow us to investigate the efficiency of aligned-spin banks to search for precessing NSBH signals using two waveform models. Using two models will help to mitigate any bias in our results that arises due to the choice of waveform approximant. We investigate the distribution of fitting factors when using a template bank constructed using the TaylorF2 metric to search for aligned-spin TaylorT4 NSBH signals in Sec. 6.6 and find that this would result in a reduction of sensitivity. We therefore make use of a metric that models the TaylorT4 waveform well. To do this we use the TaylorR2F4 waveform model. We have found that restricting the TaylorR2F4 model to terms no larger than 4.5PN and placing a bank of templates using the ensuing metric is sufficient to cover the TaylorT4 parameter space. For ease of comparison Table 1 gives the sizes and properties of all the banks that are used in this work.

Template bank	Approximant	Waveform cutoff frequency	Number of templates in bank
Geometric non-spinning bank	TaylorF2	1000Hz	117,632
Geometric non-spinning bank	TaylorR2F4 (up to 4.5PN)	1000Hz	99,309
Geometric aligned-spin bank	TaylorF2	1000Hz	817,460
Geometric aligned-spin bank	TaylorF2	400Hz	432,537
Geometric aligned-spin bank	TaylorF2	240Hz	282,090
Stochastic aligned-spin bank	TaylorF2	Dynamic	971,105
Geometric aligned-spin bank	TaylorR2F4 (up to 4.5PN)	1000Hz	1,100,277
Geometric aligned-spin bank	TaylorR2F4 (up to 4.5PN)	400Hz	504,132
Geometric aligned-spin bank	TaylorR2F4 (up to 4.5PN)	240Hz	260,325
Stochastic aligned-spin bank	TaylorR2F4 (up to 4.5PN)	Dynamic	1,327,175

Table 1: The sizes of the various template banks that are used in this work. All of these banks are valid for aligned-spin NSBHs with BH mass $\in [3, 15)M_{\odot}$; NS mass $\in [1, 3)M_{\odot}$; BH dimensionless spin $\in [-1, 1]$; NS dimensionless spin $\in [-0.05, 0.05]$. For all banks the aLIGO zero-detuned, high-power noise curve is used with a lower frequency cutoff of 15Hz.

6.6 Results I: Validating the new template bank placement for aligned-spin systems

In this section we demonstrate that our aligned-spin template banks achieve the level of coverage they are constructed for when used to search for aligned-spin signals. We also compare our banks to banks generated using a stochastic placement algorithm [100, 112, 113, 141] and show that our method acheives the same level of coverage with fewer templates.

To verify the performance of our aligned-spin template banks we compute the fitting factors between the banks and a set of 100,000 aligned-spin NSBH waveforms. These waveforms are drawn from the distribution that we describe in Sec. 6.2, except that the spins are all aligned (or anti-aligned) with the orbital angular momentum.

In Fig. 22 we show the results of this test using the template bank constructed with the TaylorF2 metric. We show results when both template waveforms and signals are modelled using the TaylorF2 approximant, when both are modeled using the TaylorT2 approximant and when we model the template waveforms with TaylorF2 and the signals with TaylorT2. In both cases where the same waveform model was used almost all of the fitting factors were greater than 0.97. The bank generation was successful.

The lowest matches in the TaylorF2 vs TaylorF2 results were in cases where a system with low mass ratio was recovered with a template with a high mass ratio, or vice-versa. These are systems where the degeneracy between the spins and the

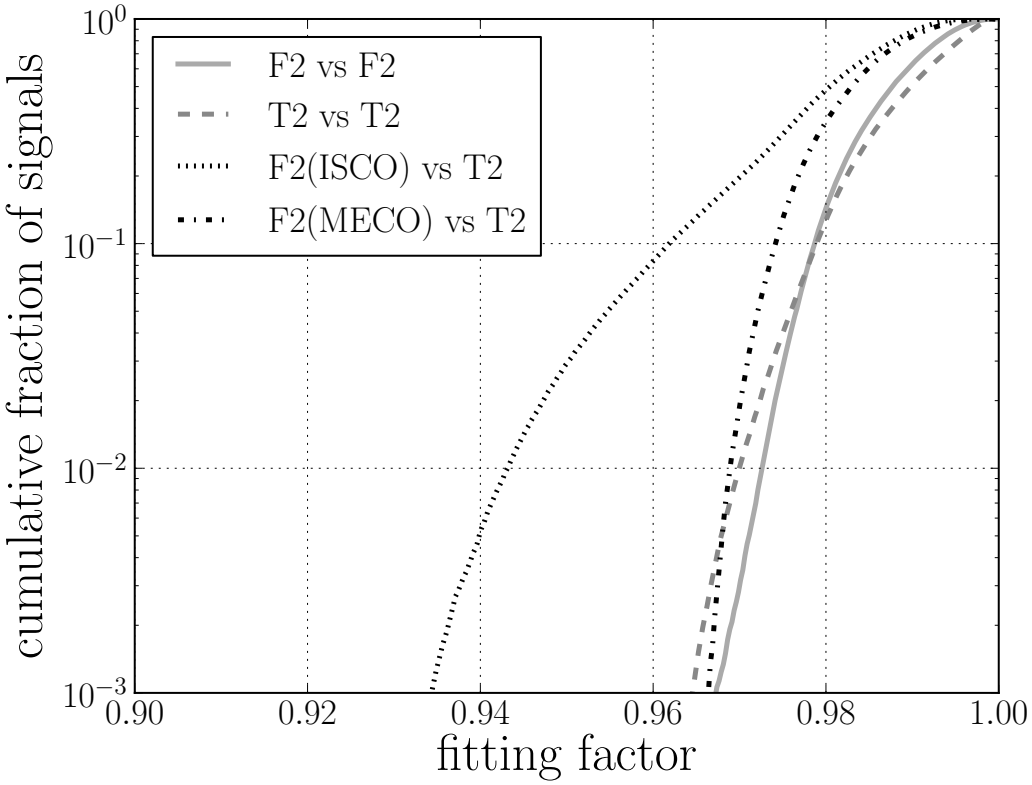

Figure 22: Fitting factor between a set of aligned-spin NSBH signals and our geometrically placed aligned-spin template bank placed using the TaylorF2 metric. Shown when both templates and signals are generated using the TaylorF2 approximant (gray solid line) and when both are modelled with TaylorT2 (gray dashed line). Also shown when the signals are modelled with TaylorT2 and the templates modelled with TaylorF2 waveforms terminated at ISCO (black dotted line) and TaylorF2 waveforms terminated at MECO (black dot-dashed line). Results obtained using the zero-detuned, high-power advanced LIGO sensitivity curve with a 15Hz lower frequency cut off.

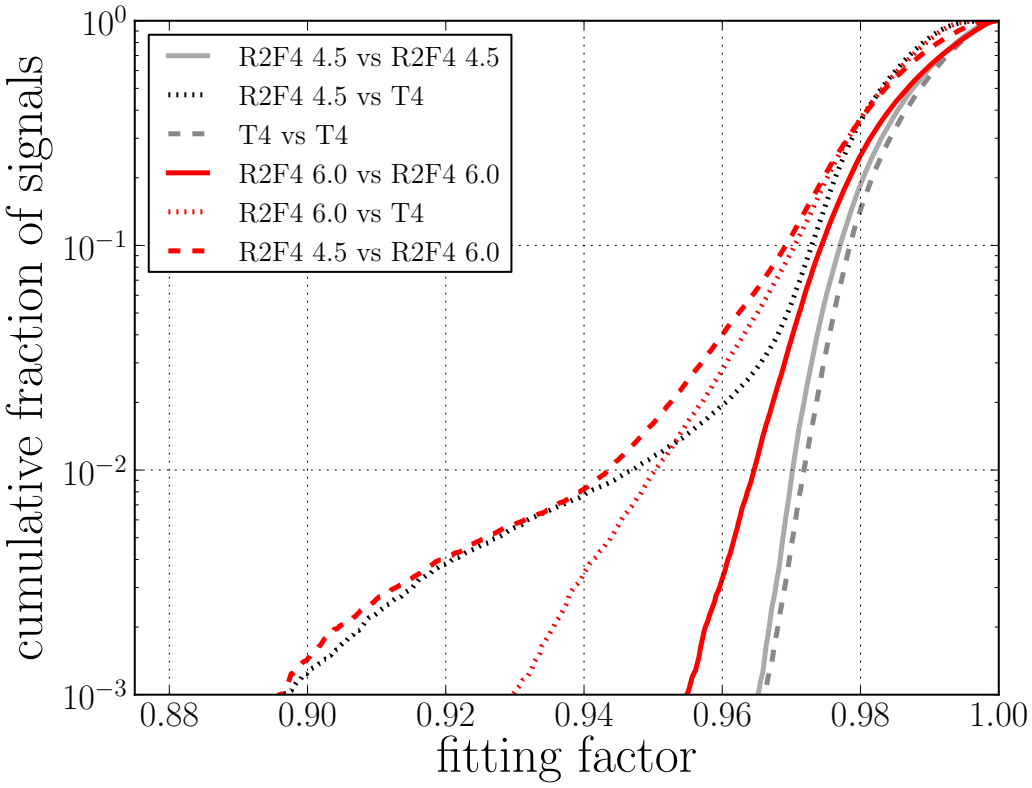

Figure 23: Fitting factor between a set of aligned-spin NSBH signals and our geometrically placed aligned-spin template bank placed using the TaylorR2F4 metric. Shown are comparisons between TaylorT4 waveforms, TaylorR2F4 waveforms including terms to 4.5PN order and TaylorR2F4 waveforms including terms to 6PN order. Results obtained using the zero-detuned, high-power advanced LIGO sensitivity curve with a 15Hz lower frequency cut off.

mass ratio [148] causes the phase evolution of the two systems to be very similar and therefore the match predicted by the metric is higher than 0.97. However, the system with the larger black hole mass will terminate at a significantly lower frequency than the system with the smaller black hole mass and some power is lost due to the difference in termination frequencies, which is not predicted by the metric.

The difference in termination conditions is also the reason why we see comparatively poorer performance when using TaylorF2 waveforms, terminated at the innermost stable circular orbit (ISCO) frequency, to search for TaylorT2 signals. The TaylorT2 signals terminate when the evolution becomes unphysical, either at the MECO or where the frequency spuriously begins to drop. In some cases, especially when the spins are large, these can correspond to rather different termination frequencies. To demonstrate this we also show the performance of searching for TaylorT2 signals with TaylorF2 waveforms, but where we terminate the TaylorF2 waveforms using the same cut-off frequency that TaylorT2 waveforms would have at the given masses and spins. This gives a much more comparable performance to the TaylorF2 vs TaylorF2 and TaylorT2 vs TaylorT2 cases.

In Fig. 23 we repeat this test using the template bank constructed with the TaylorR2F4 metric, with terms restricted to 4.5PN order. We show results when the template waveforms and signals are modeled with varying approximants. We use TaylorR2F4 with terms up to 4.5PN order, TaylorR2F4 with terms up to 6PN order and TaylorT4. We can see from this figure that using TaylorR2F4 template waveforms with terms only to 4.5PN order would not be satisfactory when conducting searches for signals modelled with the TaylorT4 approximant. However, we note that when this bank is used with either TaylorT4 templates or TaylorR2F4 templates including terms up to 6PN order the coverage is much better. When TaylorT4 is used to model both the signals and the template waveforms we find that $> 99\%$ of the fitting factors are greater than 0.97. In this plot the TaylorR2F4 waveforms are terminated at the same frequency (the MECO frequency) as the TaylorT4 waveforms.

The TaylorR2F4 metric, with terms up to 4.5PN, is sufficient to place a bank of templates to cover waveforms modeled by the TaylorT4 approximant. However, when performing the matched-filtering the templates must be modeled with either TaylorT4 or TaylorR2F4 with terms up to 6PN order.

In Fig. 24 we also show the performance of a bank placed using the TaylorF2

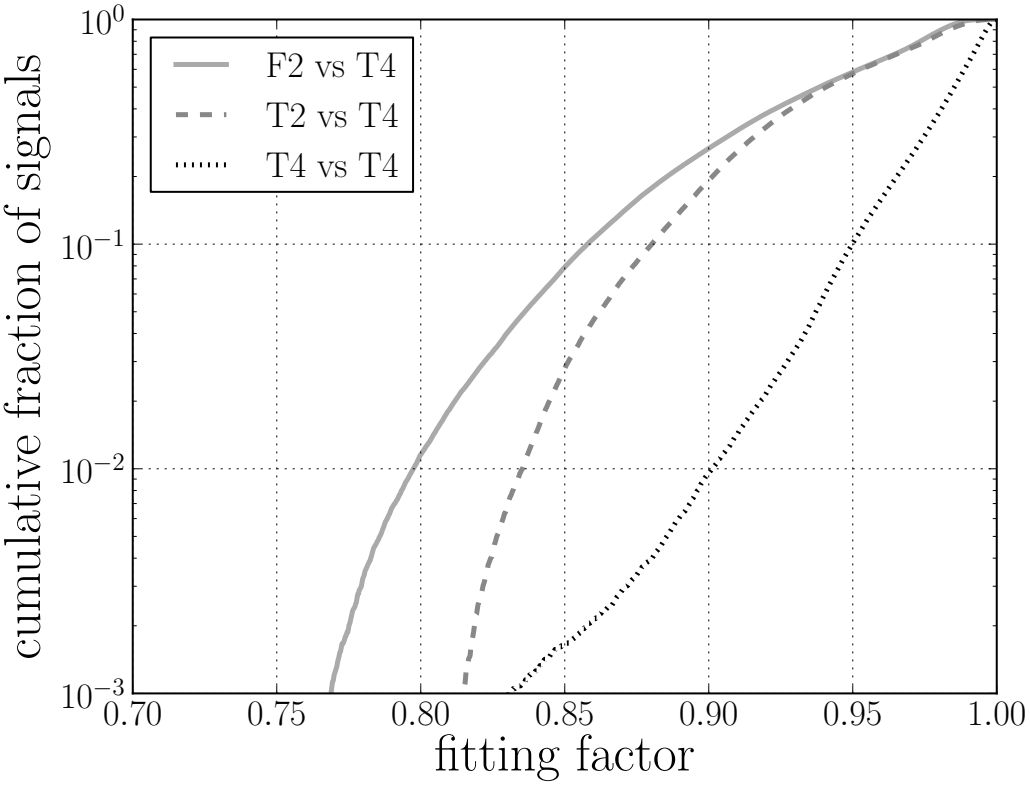

Figure 24: Fitting factor between a set of aligned-spin NSBH signals modeled with the TaylorT4 approximant and our template bank of aligned-spin signals placed using the TaylorF2 parameter space metric. Shown are the fitting factors when the templates used are modelled using the TaylorF2 approximant (gray solid line), TaylorT2 (grey dashed line) and TaylorT4 (black dotted line). Results obtained using the zero-detuned, high-power advanced LIGO sensitivity curve with a 15Hz lower frequency cut off.

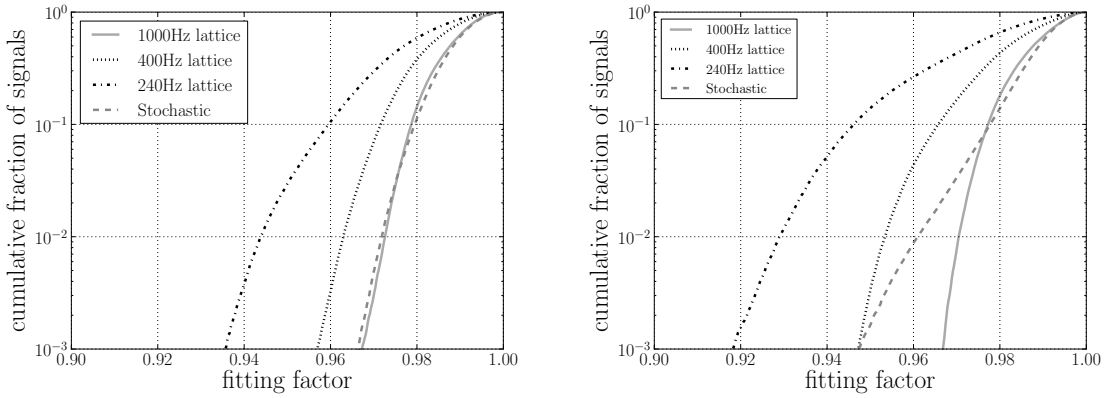

Figure 25: Fitting factor between a set of aligned-spin NSBH signals and a template bank of aligned-spin waveforms for varying values of the upper frequency cutoff used in the construction metric. Shown for template banks placed using the TaylorF2 metric and with both templates and signals modelled using the TaylorF2 approximant (left). Also shown for template banks placed using the TaylorR2F4 metric and with both templates and signals modelled using the TaylorR2F4 approximant (right). The performance of using a stochastically placed template bank with varying upper frequency cutoff is also plotted. Results obtained using the zero-detuned, high-power advanced LIGO sensitivity curve with a 15Hz lower frequency cut off.

metric to search for TaylorT4 aligned-spin signals. We assess the performance when the templates are modeled using TaylorF2, TaylorT2 and TaylorT4 approximants. Even when TaylorT4 is used to model both template waveforms and signals, 10% of signals are recovered with fitting factors smaller than 0.95. The TaylorF2 metric does not achieve the desired coverage for TaylorT4 waveforms.

6.6.1 Varying the upper frequency cutoff and comparison with stochastic placement algorithms

Filtering $\sim 10^6$ templates against data from advanced gravitational-wave detectors will require a large amount of computing power. It would therefore be desirable if we could reduce the overcoverage that is incurred in the high mass region of the parameter space when using an upper frequency cutoff of 1000 Hz. An alternative "stochastic" placement scheme, based on randomly picking points in the space and only retaining points which are not close to points already in the bank [100, 112, 113], is capable of using an upper frequency cutoff that varies with mass [141]. However, this method is

known to pack templates more densely than a geometrical lattice [100]. We found that using a stochastic method to cover this NSBH space with the same covering criterion required 971,105 (1,327,175) templates when using the TaylorF2 (TaylorR2F4) metric to place the bank. In both cases this is $\sim 20\%$ larger than our geometric algorithm using a constant upper frequency cutoff of 1000 Hz. It is also possible to generate the geometric bank with a lower upper frequency cutoff. This will require less templates, but will not reach the desired coverage in the lower mass regions of the parameter space. In Fig. 25 we compare the efficiency of geometric banks placed using a 240Hz, 1000Hz and 400Hz upper frequency cutoff. These correspond to roughly the lowest possible ISCO frequency, the highest and an "average" system. The sizes of these banks are shown in Table 1. As expected we notice a number of systems recovered with fitting factors less than 0.97 when the upper frequency cutoff is reduced. We also compare with the performance of a stochastic placement algorithm, which uses a varying upper frequency cutoff. The performance of the stochastic bank is very comparable to the 1000Hz bank when using the TaylorF2 metric. When using the TaylorR2F4 metric the stochastic bank, which was placed using 10^9 seed points, seems to be struggling to achieve the necessary coverage in certain regions of the space. As the stochastic placement algorithm only uses a finite number of sample points, it is known that it can leave holes in the parameter space, resulting in undercoverage [100].

We plan to adapt the geometric placement algorithm to allow the upper frequency cutoff to vary over the space, however we leave this investigation for future work. We note that the minimal match and *lower* frequency cutoff of the bank can also be modified to reduce the number of templates and balance the computational cost [56].

6.7 Results II: Template bank performance when searching for generic NSBH signals

In this section we evaluate the efficiency of searching for generic NSBH systems using template banks of non-spinning waveforms. Template banks of non-spinning waveforms were used to search for NSBH signals in data from LIGO and Virgo's most recent science runs [12, 13, 14, 15]. We demonstrate that ignoring the effects of spin when conducting searches for NSBH systems in the advanced detector era will significantly decrease the rate of NSBH observations and impose a selection bias against

systems with large spins and large m_{BH}/m_{NS}. We then evaluate the efficiency of searching for generic NSBH systems using our new template bank of aligned-spin waveforms. We calculate the improvement gained by using our new bank when compared to a non-spinning bank.

6.7.1 Performance of non-spinning template banks when searching for generic NSBH signals

We compute fitting factors between a set of 100,000 generic, precessing NSBH signals and a bank of non-spinning template waveforms. The precessing signals are drawn from the distribution that we describe in Sec. 6.2. To mitigate any bias that arises due to the choice of waveform approximant we run the simulation twice. First we use the TaylorT2 approximant for both signal and template waveforms and a template bank designed to obtain a fitting factor of at least 0.97 for any TaylorT2 non-spinning signal. The simulation was then repeated using the TaylorT4 approximant for both signal and template waveforms and a bank designed with the same fitting factor criterion for TaylorT4 signals. These banks were constructed using the methods described to create aligned-spin banks in Sec. 6.5 but with the spins set to 0.

The results of this simulation can be seen in Fig. 26. From this we can calculate the mean and median values of the fitting factor over the signal distribution that we used. The mean fitting factor of the signals is 0.82 (0.84) for the TaylorT2 (TaylorT4) approximant, while the median fitting factor was 0.86 (0.88). In both cases the distributions have long tails, with some systems recovered with less than 30% of their optimal SNR. We also show results where we have modeled the templates using the TaylorT2 approximant and the signals using the TaylorT4 approximant. In this case the mean fitting factor is 0.84 and the median is 0.87. We notice that fewer signals are recovered with high fitting factors (> 0.95) than in the other two cases, but we notice that at lower values of fitting factor the performance is very similar to the TaylorT4 vs TaylorT4 case. The slight *improvement* of the TaylorT2 vs TaylorT4 case at lower fitting factors can be attributed to the fact that the TaylorT2 bank is $\sim 20\%$ larger than the TaylorT4 bank and therefore has more freedom to match TaylorT4-modeled spinning signals.

In Fig. 27, we show the mean fitting factor as a function of the intrinsic parameters of the system when both templates and signals were modeled with the TaylorT4

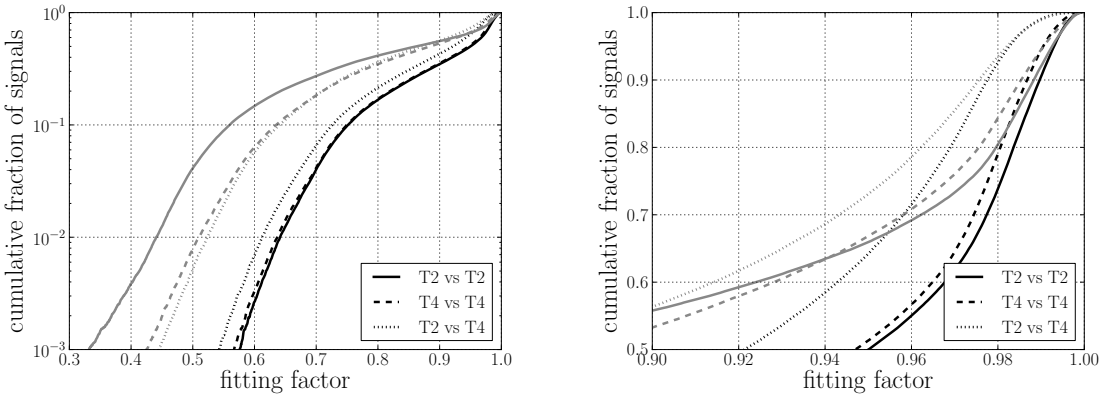

Figure 26: Fitting factor between a set of generic, precessing, NSBH signals and a template bank of aligned-spin waveforms. Shown when both templates and signals are generated using the TaylorT2 approximant (black solid line) and the TaylorT4 approximant (black dashed line). Also shown when the templates are modeled using TaylorT2 and the signals are modelled using TaylorT4 (black dotted line). For comparison the same results using a template bank of non-spinning waveforms are also plotted in grey. Plotted over the full range of fitting factors (left) and zoomed in to show only fitting factors greater than 0.9 (right). The distribution that the NSBH signals are drawn from is described in Sec. 6.2. The template bank construction is described in Sec. 6.5. Results obtained using the zero-detuned, high-power advanced LIGO sensitivity curve with a 15Hz lower frequency cut off.

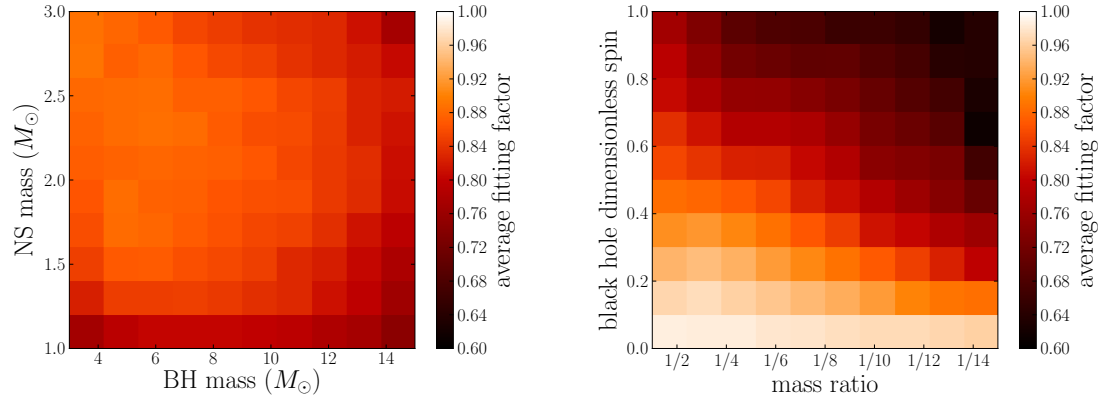

Figure 27: Average fitting factor between a set of generic, precessing, NSBH signals and a template bank of non-spinning waveforms as a function of the component masses (left) and as a function of the mass ratio and the black hole dimensionless spin magnitude (right). Both the signals and the template waveforms are modelled using the TaylorT4 approximant. The distribution that the NSBH signals are drawn from is described in Sec. 6.2. Results obtained using the zero-detuned, high-power advanced LIGO sensitivity curve with a 15Hz lower frequency cut off.

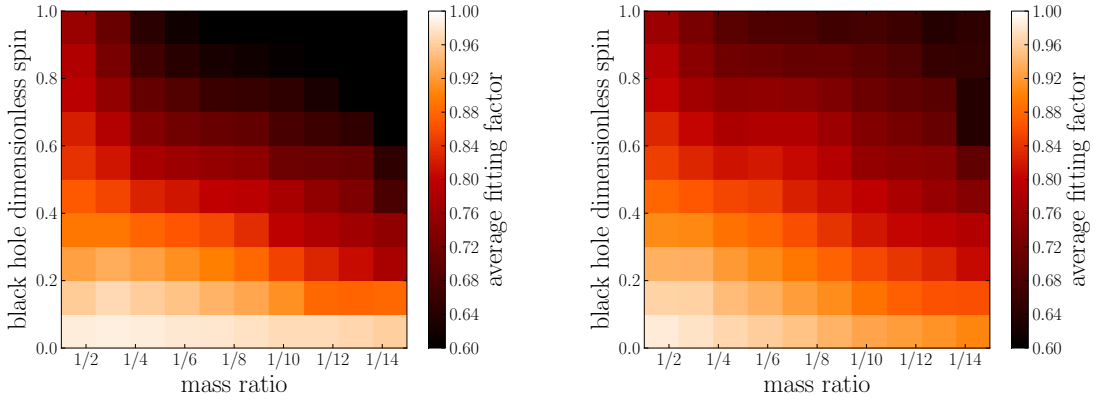

Figure 28: Average fitting factor between a set of generic, precessing, NSBH signals and a template bank of non-spinning waveforms as a function of the mass ratio and the black hole dimensionless spin magnitude (right). Shown when both the template waveforms and signals are modeled with TaylorT2 (left) and when the template waveforms are modeled with TaylorT2 and the signals are modelled with TaylorT4 (right). The results in these plots are almost identical to each other and to the right panel of Fig. 27. The distribution that the NSBH signals are drawn from is described in Sec. 6.2. Results obtained using the zero-detuned, high-power advanced LIGO sensitivity curve with a 15Hz lower frequency cut off.

approximant. For comparison, in Fig. 28 we show the mean fitting factor as a function of the spin magnitude and mass ratio for the TaylorT2 vs TaylorT2 results and the TaylorT2 vs TaylorT4 results. In both cases the results are similar to the TaylorT4 vs TaylorT4 case, which indicates that the results are not suffering from a significant bias due to the choice of waveform approximant. However, we note that when using TaylorT2 as the signal model, the performance of the non-spinning banks is worse for high spin, unequal mass systems than when using TaylorT4 as the signal model.

In Fig. 29 we show the signal recovery fraction as a function of the BH spin magnitude and the mass ratio. The signal recovery fraction is defined in Sec.6.4. It is clear that using a non-spinning bank to search for NSBH systems will result in a considerable reduction in the NSBH detection rate. In addition, the ability to detect systems with high spin, especially systems that also have unequal masses, is especially poor. We note that these efficiencies would be improved by using non-spinning templates outside of the chosen mass ranges, for example BNS or binary black-hole template waveforms, or even templates with unphysical mass parameters [55, 148].

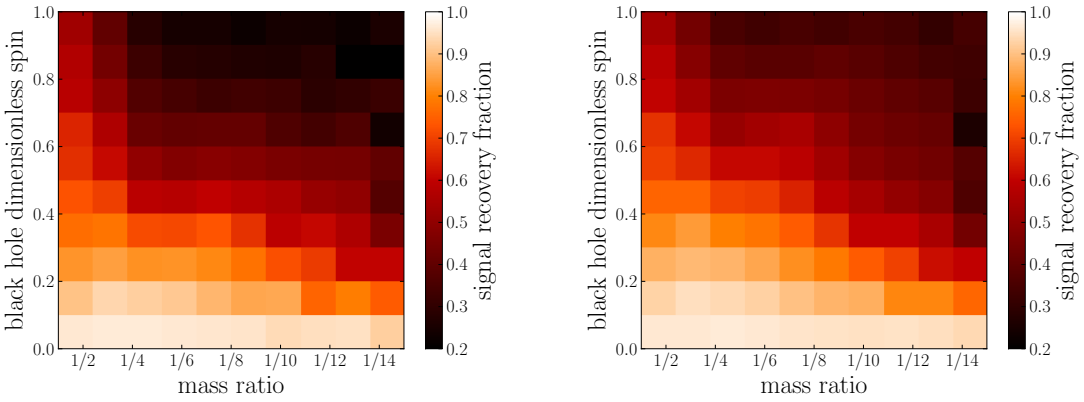

Figure 29: The signal recovery fraction obtained for a set of generic, precessing, NSBH signals and a template bank of non-spinning waveforms as a function of the mass ratio and the black hole dimensionless spin. Shown when both the template waveforms and the signals are modeled with TaylorT2 (left) and when both the template waveforms and the signals are modeled with TaylorT4 (right). The distribution of the signal recovery fraction over the mass space is very similar to the distribution of average fitting factors shown in Figs. 27 and 28. The distribution that the NSBH signals are drawn from is described in Sec. 6.2. Results obtained using the zero-detuned, high-power advanced LIGO sensitivity curve with a 15Hz lower frequency cut off.

6.7.2 Performance of aligned-spin template banks when searching for generic NSBH signals

With the template banks of aligned-spin systems described in Sec. 6.5, we are able to recover aligned-spin systems modelled with either the TaylorT2 or TaylorT4 approximant with fitting factors greater than 0.97 in $> 99\%$ of cases, as shown in Sec. 6.6. If we use these banks to search for precessing systems modelled with the same approximants, any loss in signal power, beyond that lost due to the spacing of the aligned-spin bank, is entirely due to precession. We now assess the performance of these aligned-spin banks when searching for generic, precessing NSBH signals and identify regions of the parameter space where precessional effects cause a significant loss in detection rate.

Our signal population is a set of 100,000 precessing NSBH signals. This distribution was described in Sec. 6.2. For comparison this is the *same* set of signals as we used in Sec. 6.7.1. As before, we will assess fitting factors using both the TaylorT2 and TaylorT4 models to mitigate any bias arising from choice of waveform model. When TaylorT2 is used as the signal model, we will use the bank of aligned-spin systems that was placed using the TaylorF2 metric and a 1000Hz upper frequency cutoff and model the templates using the TaylorT2 approximant. When TaylorT4 is used as the signal model, we will use the bank of aligned-spin systems placed using the TaylorR2F4 metric and model the templates with TaylorT4. The placement of these banks was described in section 6.5.

The results of these simulations can be seen in Fig. 26, where we also compare with the results obtained in Sec. 6.7.1 when using non-spinning template banks. We can clearly see from Fig. 26 that the distribution of fitting factors for the case when both signals and templates were modeled with TaylorT2 agrees well with the case when both were modeled with TaylorT4. This indicates that we have disentangled precessional effects from waveform-dependent effects and our results are free of any bias due to the choice of waveform model. The mismatches seen here, beyond that caused by the discreteness of the bank, are due only to the effects of precession. In both cases we observe a median fitting factor of ~ 0.95 and a mean fitting factor of ~ 0.91. This is a clear improvement over the non-spinning results where the mean fitting factor was 0.82 (0.84) for TaylorT2 (TaylorT4) and the median fitting factor

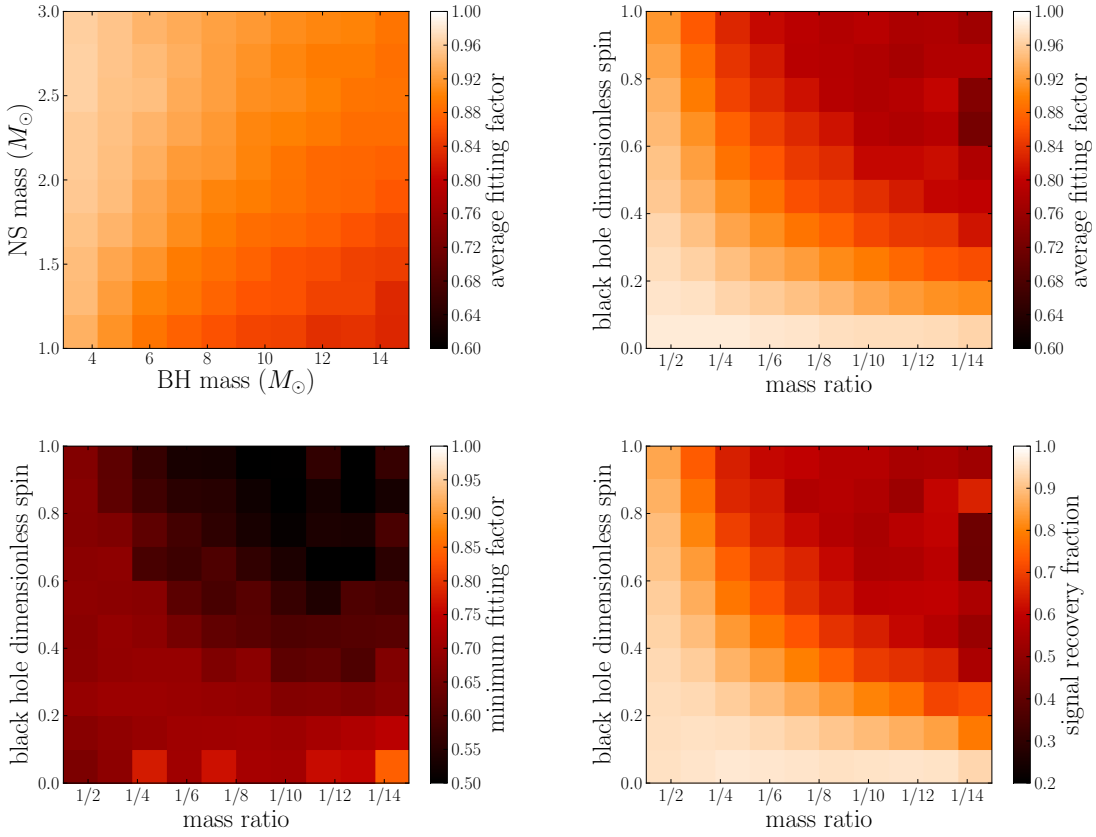

Figure 30: Average fitting factor between a set of generic, precessing, NSBH signals and a template bank of aligned-spin waveforms as a function of the component masses (top left) and as a function of the mass ratio and the black hole dimensionless spin magnitude (top right). Also plotted is the minimum fitting factor (bottom left) and the signal recovery fraction (bottom right) as a function of the mass ratio and the black hole dimensionless spin magnitude. Both signals and template waveforms are modeled using the TaylorT4 approximant. The distribution that the NSBH signals are drawn from is described in Sec. 6.2. The template bank construction is described in Sec. 6.5. Results obtained using the zero-detuned, high-power advanced LIGO sensitivity curve with a 15Hz lower frequency cut off.

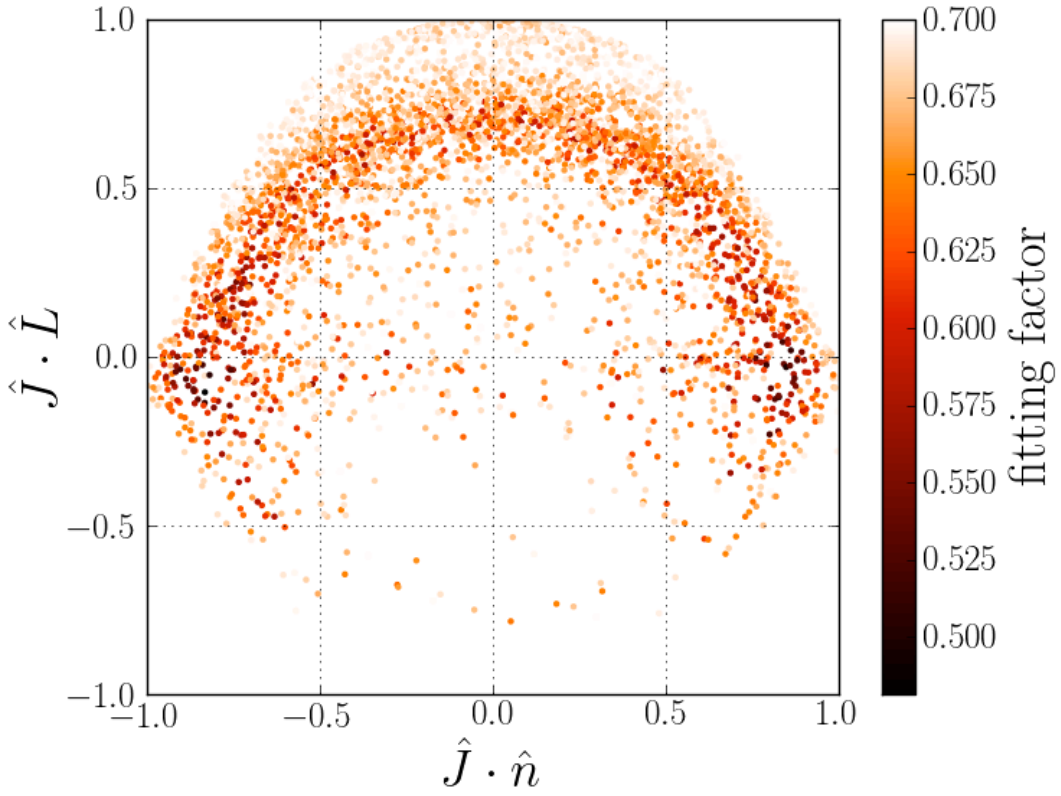

Figure 31: The distribution of precessing NSBH signals that are recovered with fitting factors < 0.7 when searching with an aligned-spin template bank. We use $\hat{J}$ to denote the initial total angular momentum of the system, $\hat{n}$ denotes the line of sight towards the observer and $\hat{L}$ denotes the orbital angular momentum when the gravitational wave frequency is 60 Hz (at which point approximately half of the signal power has accumulated). Both signals and template waveforms are modelled using the TaylorT4 approximant. The distribution that the NSBH signals are drawn from is described in Sec. 6.2. The template bank construction is described in Sec. 6.5. Results obtained using the zero-detuned, high-power advanced LIGO sensitivity curve with a 15Hz lower frequency cut off.

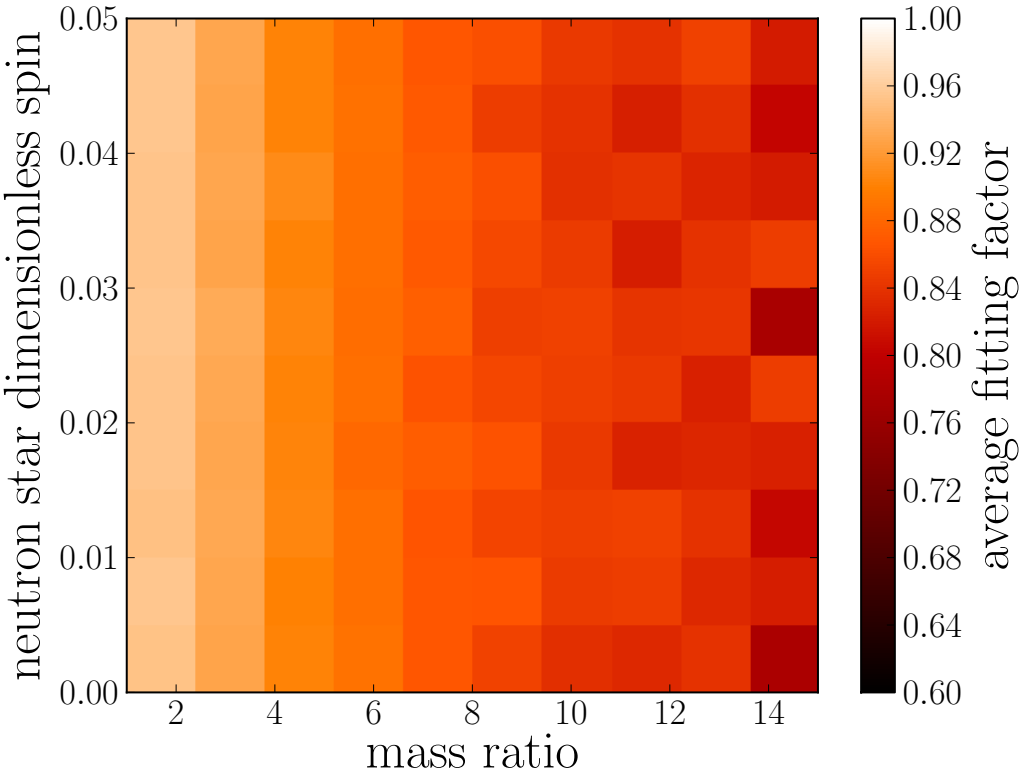

Figure 32: Average fitting factor between a set of generic, precessing, NSBH signals and a template bank of aligned-spin waveforms as a function of the mass ratio and the neutron star dimensionless spin magnitude (top right). Both signals and template waveforms are modeled using the TaylorT4 approximant. The distribution that the NSBH signals are drawn from is described in Sec. 6.2. The template bank construction is described in Sec. 6.5. Results obtained using the zero-detuned, high-power advanced LIGO sensitivity curve with a 15Hz lower frequency cut off.

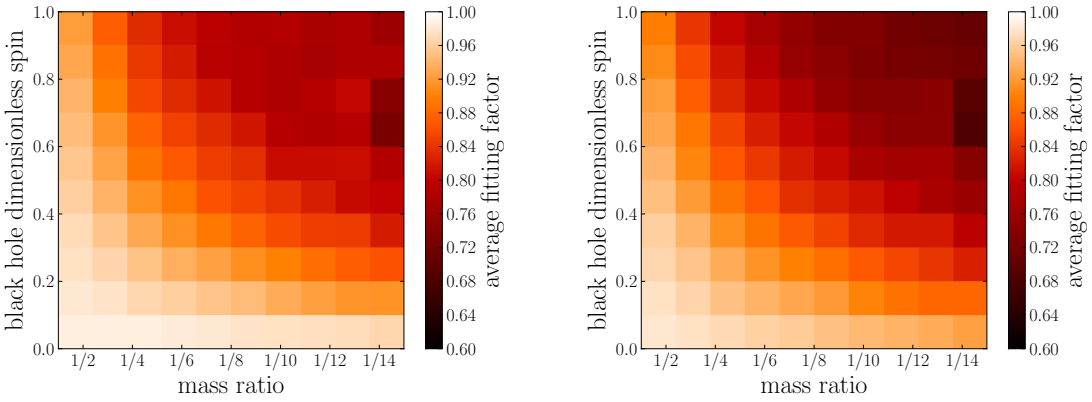

Figure 33: Average fitting factor between a set of generic, precessing, NSBH signals and a template bank of aligned-spin waveforms as a function of the mass ratio and the black hole dimensionless spin magnitude. Shown when both the template waveforms and signals are modeled with TaylorT2 (left) and when the template waveforms are modelled with TaylorT2 and the signals are modeled with TaylorT4 (right). The results in these plots are almost identical to each other and to the top right panel of Fig. 30. The distribution that the NSBH signals are drawn from is described in Sec. 6.2. The template bank construction is described in Sec. 6.5. Results obtained using the zero-detuned, high-power advanced LIGO sensitivity curve with a 15Hz lower frequency cut off.

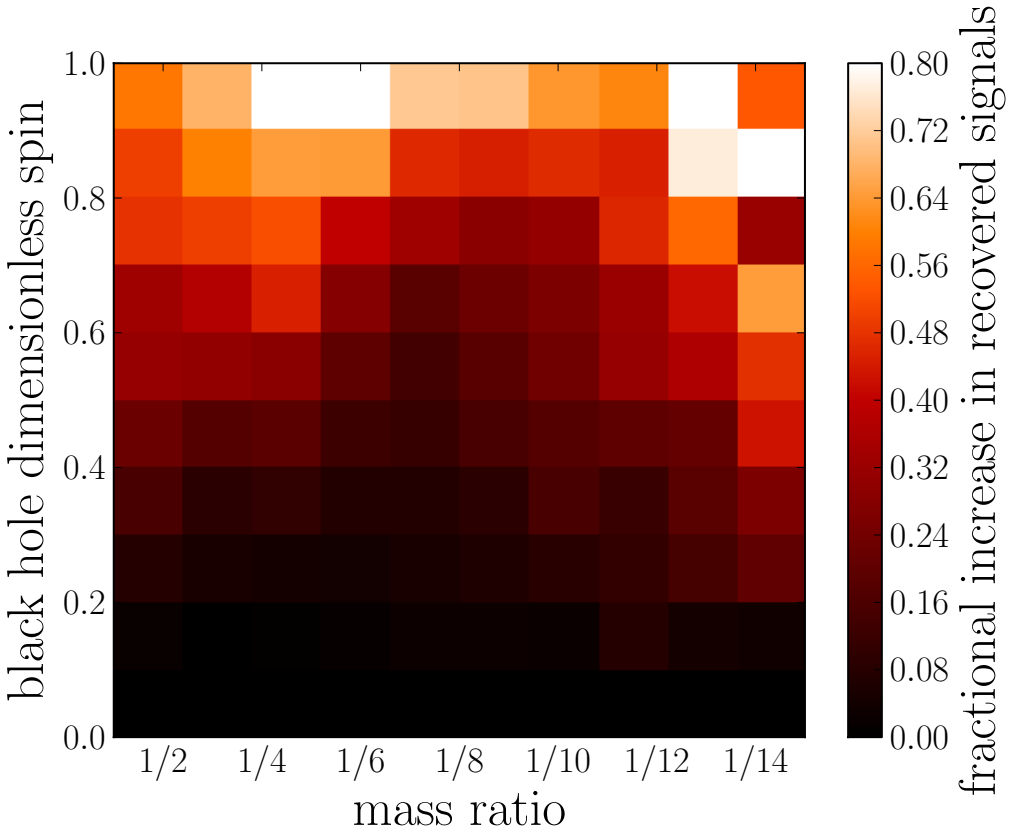

Figure 34: The fractional increase in the number of recovered signals when searching for generic, precessing, NSBH signals using a template bank of aligned-spin waveforms and a template bank of non-spinning waveforms. Both signals and template waveforms are modeled using the TaylorT4 approximant. The distribution that the NSBH signals are drawn from is described in Sec. 6.2. The template bank construction is described in Sec. 6.5. Results obtained using the zero-detuned, high-power advanced LIGO sensitivity curve with a 15Hz lower frequency cut off.

was 0.86 (0.88).

In Fig. 26 we also show results where the template waveforms are modeled with TaylorT2 and the signals are modeled with TaylorT4. In this case the performance is worse, with a median fitting factor of ~ 0.92 and a mean fitting factor of ~ 0.88.

In Fig. 30 we show the mean fitting factor as a function of the intrinsic parameters for our results with the TaylorT4 waveform. We also show the minimum fitting factor and the signal recovery fraction as a function of the BH spin magnitude and mass ratio for the same results. The Figure serves to highlight that there are certain systems in certain regions of the parameter space where precessional effects cause the NSBH signals to have large mismatches with a bank of aligned-spin templates. This is most prominent when m_{BH}/m_{NS} and the BH spin magnitude are both large, ie. where the black hole's angular momentum is particularly large relative to the orbital angular momentum. We explore this further in Fig. 31 where, following the work of [114], we show the distribution of precessing systems recovered with fitting-factors smaller than 0.7. This is plotted as a function of the angles between the total angular momentum, the orbital angular momentum and the line of sight to an observer. As predicted in [114], there is clearly a correlation between these angles and the systems recovered with the lowest fitting factors. To demonstrate that these results are not specific to the TaylorT4 waveform, in Fig. 33 we show the mean fitting factor as a function of the BH spin magnitude and mass ratio for our TaylorT2 vs TaylorT2 and TaylorT2 vs TaylorT4 results. The TaylorT2 results are very similar to the TaylorT4 results in Fig. 30. This again demonstrates that the choice of waveform is not affecting our statements regarding the effect precession will have on searches for NSBH signals using aligned-spin template banks. When searching for TaylorT4 signals with TaylorT2 templates we see lower fitting factors. The disagreement between these two waveform models is a significant factor that will affect searches for NSBH systems with second generation observatories. Computing higher order terms in the Post-Newtonian (PN) expansion of the center-of-mass energy and gravitational wave flux will help to reduce this disagreement and produce waveforms that better match real gravitational-wave signals. In Fig. 32 we plot the average fitting factor as a function of the mass ratio and the *neutron star* dimensionless spin. There is not any noticeable correlation between the average fitting factor and the neutron star's spin.

We can also compare these results to the results we obtained using a non-spinning

Template	Signal	Signal recovery fraction for non-spinning bank		Signal recovery fraction for aligned-spin bank		Fractional improvement in signal recovery	
		Average	$(10, 1.4)M_\odot$	Average	$(10, 1.4)M_\odot$	Average	$(10, 1.4)M_\odot$
TaylorT2	TaylorT2	64%	63%	83%	74%	30%	17%
TaylorT4	TaylorT4	69%	67%	82%	73%	19%	9%
TaylorT2	TaylorT4	67%	64%	77%	67%	16%	5%

Table 2: The performance of our aligned-spin template banks when used to search for a set of generic, precessing, NSBH signals using varying approximants for the template and signal waveforms. We show both the mean signal recovery fraction over the full NSBH signal population we consider and the signal recovery fraction for a NSBH system with masses $(10 \pm 0.5, 1.4 \pm 0.05)M_\odot$. The distribution that the NSBH signals are drawn from is described in Sec. 6.2. The template bank construction is described in Sec. 6.5. Results obtained using the zero-detuned, high-power advanced LIGO sensitivity curve with a 15Hz lower frequency cut off and a 1000Hz upper frequency cut off.

template bank in Sec. 6.7.1. In Fig. 34 we show the fractional increase in the number of recovered signals between using non-spinning and aligned-spin template banks for the TaylorT4 approximant. The fractional increase in the number of recovered signals is calculated by taking the ratio of the signal recovery fraction when using a non-spinning bank and the signal recovery fraction when using an aligned-spin bank. This figure helps to emphasize that a much greater fraction of systems with large spin would be recovered when using an aligned-spin template bank. In Table 2 we summarize the average signal recovery fractions for the aligned-spin banks and compare these numbers to the results obtained with non-spinning template banks. We remind the reader that we are comparing signal recovery at a fixed signal-to-noise ratio. Signal recovery at a fixed false-alarm probability will depend on other factors, including the size of the parameter space covered by the template bank and the non-Gaussianity of the data. We discuss this further in the conclusion.

Finally, we compare our results with previous works. In [141] the authors presented an efficiency study when using a template bank of stochastically generated aligned-spin signals. We verified that when using the stochastic algorithm we used in this work, and using the same set of parameters as the study described in [141], we generated a bank with the same number of templates. We have therefore demonstrated that our template bank algorithm requires less templates to acheive the same level of coverage as the algorithm used in [141]. In that work the effective fitting

factor for a NSBH system with masses given by $10M_\odot$, $1.4M_\odot$ was estimated to be 0.95, which corresponds to a signal recovery fraction of 86%. In contrast, our results show a lower signal recovery fraction for the same masses of $73-74\%$ when the same waveform model is used to model both the template and signal. It isn't clear why this discrepancy occurs, however it may be partially explained by the fact that the authors of [141] used a lower frequency cutoff in their matched-filters of 20Hz, whereas we used 15Hz, which is more appropriate for the predicted aLIGO zero-detuned–high-power noise curve.

In [114] the authors used a simplified model of precessing systems to predict the distribution of fitting factors for NSBH systems. These results, shown in Figure 11 of that work, agree qualitatively with the results obtained here. We also obtain quantitative agreement by comparing our simulations of generic precessing systems with TaylorT4 as the signal and template model with the values predicted by Eq. 46b of [114]. We find that 90% of the fitting factors are within 0.03 of the predicted values. They also predicted the distribution of the signals that would be recovered with the lowest fitting factors as a function of the orientation of the black hole spin and the orientation of the orbital plane with respect to the line of sight. We produce a similar distribution in Fig. 31. A further exploration of the agreement of the fitting factors with this prediction will be carried out in a future work making use of these simulations.

6.8 Conclusions

In this work we have explored the effect that the angular momentum of the black hole will have on searches for neutron-star black-hole binaries with aLIGO. The black hole's angular momentum will affect the phase evolution of the emitted gravitational-wave signal, and, if the angular momentum is misaligned with the orbital plane, will cause the system to precess. We have found that if these effects are neglected in the filter waveforms used to search for NSBH binaries it will result in a loss in detection rate of $31-36\%$ when searching for NSBH systems with masses uniformly distributed in the range $(3-15, 1-3)M_\odot$. When restricting the masses to $(9.5-10.5, 1.35-1.45)M_\odot$ we find that the loss in detection rate is $33-37\%$. The error in these measurements is due to uncertainty in the PN waveform models used to simulate

NSBH gravitational-wave signals.

We have shown that an aligned spin template bank offers a $16\% - 30\%$ improvement in the detection rate of neutron-star black-hole mergers when compared to a non-spinning template bank when searching for NSBH systems with masses in the range $(3 - 15, 1 - 3)M_{\odot}$. However, when searching for NSBH systems with masses restricted to the range $(9.5 - 10.5, 1.35 - 1.45)M_{\odot}$ we find the improvement is reduced to $5 - 17\%$. Some systems are not recovered well with this new bank of filters. These systems are ones where the black-hole spin is misaligned with the orbit and the waveform is significantly modified due to precession of the orbital plane. This happens most often when m_{BH}/m_{NS} and the spin magnitude are both large. In [114] the authors predict where in the parameter space to expect NSBH systems that will not be recovered well by non-precessing template banks. These predictions were given in terms of the angles between the orbital plane, the black hole's angular momentum and the line-of-sight to an observer. These predictions agree with the results that we obtain in this work. In [141] the authors claim that an aligned-spin template bank will be effectual for detecting precessing NSBH systems. In this work, we find that with an aligned-spin template bank $17 - 23\%$ of NSBH systems will be missed compared to an ideal search with exactly matching filter waveforms. In reality this ideal search could never be performed as it would require an infinite number of filter waveforms. Template banks are usually constructed to allow for no more than a 3% loss in SNR, therefore we expect to lose up to 10% of systems even if the template bank fully covers the signal parameter space. We therefore conclude that searches using precessing waveforms as templates could potentially increase the detection rate of NSBH signals, but not by more than $\sim 20\%$. Performing such a search would, however, remove an observational bias against systems where precessional effects are most prevalent in the gravitational-wave signal.

These figures are also affected by the parameter distribution chosen for the NSBH systems. Here we chose a distribution that is uniform in mass, uniform in spin magnitudes, isotropic in spin orientations and isotropic in orientation parameters and sky location. We have however, explored how the ability to detect precessig NSBH signals varies as a function of the masses and spins as seen in Figs. 30 and 31.

When searching for NSBH systems in aLIGO one has to consider the non-Gaussianity of the background noise, which we have not done in this work. A non-Gaussian noise

artifact can produce SNRs that are considerably larger than those expected from Gaussian noise fluctuations. To deal with this, numerous consistency tests are used in the analyses to separate gravitational wave signals from instrumental noise artifacts [59]. It is possible that the detection rate could be further reduced from the values we quote in this work if some signals *fail* these consistency tests and are misclassified as non-Gaussian noise transients. However, these signal consistency tests should only act to remove, or reduce the significance of, events that already have low fitting factors and therefore do not match well with the search templates. Another important consideration is that of the number of templates used in the bank. To achieve higher fitting factors will require more template waveforms, covering a larger signal space, which will allow more freedom in matching the background noise and will mean that the SNR of the loudest background triggers will increase. Therefore signals will need slightly higher SNRs to achieve the same false alarm probability. However, a factor of 10 increase in the number of *independent* templates will only increase the expected SNR of the loudest background event by less than 5%, if Gaussian noise is assumed. Therefore, while we are careful to note these considerations, we do not believe they will have a large impact on the numbers we quote above and leave a detailed investigation of such effects to future work.

In this work we have restricted ourselves to considering post-Newtonian, inspiral-only signal waveforms and consider only the case of two point particles. This was done as there is not currently any widely available waveform model that includes both the full evolution of a NSBH coalescence *and* includes precessional effects over the full parameter space that we consider. When such a model is available it may be that tidal forces and the merger component of the waveform may affect our conclusions. We believe that such effects will be limited as the black hole mass is $< 15M_{\odot}$ in our simulations, however it would be informative to repeat our simulations when a full NSBH waveform model is available.

Chapter 7

Improvements to the CBC Search Pipeline

7.1 Introduction

In this chapter we focus on the offline search pipeline that will be used to search for compact binary coalescence signals in aLIGO and AdV. We describe several proposed modifications to the `ihope` search pipeline to create a simpler, more sensitive search pipeline and to reduce the computational cost of the search. These improvements include: (i) changing the pipeline workflow from the *two-stage* analysis described in Ref. [59], where two coincidence tests are applied to reduce the computational cost of signal-based vetoes, to a *single-stage* pipeline with one coincidence test; (ii) a more efficient algorithm for computing the signal-based veto used in previous LIGO-Virgo searches; (iii) improved methods for using time-shifted detector data to estimate the significance of candidates; (iv) use of third-and-half order post-Newtonian waveforms to place the bank of templates used for matched filtering [149]; (v) simplifying template placement by using a power spectral density estimate over longer periods of time, and by using a shared template bank in all detectors [57]; (vi) improvements to the methods use to determine if candidate events are coincident in the detector network.

In this analysis, we have configured the pipeline to search for non-spinning compact object binaries with a total mass between 2 and 25 $M_{\odot}$ using 3.5 post-Newtonian

order TaylorF2 waveforms in the matched filter. The TaylorF2 waveform is constructed using the stationary phase approximation and includes only the inspiral portion of the waveform [88]. We use data from LIGO's sixth science run to test the search pipelines. These data are dominated by seismic noise frequencies below 40 Hz. We therefore set the starting frequency for these template waveforms at 40 Hz, with the templates terminating at the frequency of the innermost stable circular orbit for a test particle in the spacetime (ISCO). These parameters are chosen to be the same as for the S6/VSR2,3 search described in Ref. [15]. However, since that analysis it has been shown that searches for signals with total mass above $\sim 12\ M_{\odot}$ should use templates that capture the full inspiral-merger-ringdown signal to obtain the maximum signal-to-noise ratio [30]. Furthermore, since the simulated signals that are used to test search sensitivity are generated in the time domain, they are generated using a different post-Newtonian approximant than the frequency-domain filter templates. The maximal mass of the injected systems is therefore restricted by the uncertainties of the post-Newtonian waveforms. For total masses below $\sim 14\ M_{\odot}$, it has been shown that the discrepancy between post-Newtonian models is negligible [29]. Consequently, we set the upper limit of the injections to $\sim 14\ M_{\odot}$. We discard templates corresponding to chirp masses higher than $6.1\ M_{\odot}$ in post-processing. This is equivalent to ignoring the results of the highest mass bin in the S6/VSR2,3 search, allowing us to make a direct comparison to the S6/VSR2,3 results in a region where post-Newtonian waveforms are known to be valid for aLIGO and AdV. We determine the effect of the proposed changes to the search pipeline by comparing the sensitivity of the search in two weeks of LIGO data from the sixth LIGO science run to its performance on two weeks of stationary, Gaussian noise. To determine the performance of the search, simulated signals are added to the detector data and we record the search's ability to identify and measure the significance of these simulated gravitational waves and to measure the sensitivity of the search pipeline as a function of false-alarm rate. Searches for higher mass systems and searches using template waveforms that incorporate spin have been also been performed [11, 150, 151, 152, 153], but they are outside the scope of this work.

We show that the new pipeline is substantially simpler than that of Ref. [59] and that it can calculate false-alarm rates to $\sim 1/10,000$ years on one week of LIGO data. The performance of the search pipeline in LIGO S6 data is very close to that of

stationary, Gaussian noise. The computational cost of the improved pipeline is also comparable to the pipeline used in previous science runs. We show that together, our proposed improvements yield approximately a 10% improvement in search sensitive volume at a false-alarm rate of 1/1000 years. Given these advantages, we propose that this pipeline be used as the basis for offline searches for compact binary coalescence in future LIGO and Virgo observing runs. We note some additional improvements that can be made to the pipeline before aLIGO and AdV's first observing runs.

The rest of this chapter is organized as follows: in Sec. 7.2, we describe the methods used to search for coincident detector searches for compact binary coalescence. In Sec. 7.3 we review the `ihope` pipeline used in S6/VSR2,3, describe the improvements that we propose, and our methods for testing these improvements. For aLIGO and AdV the pipeline workflow generator, template placement, and filtering engine have been substantially re-written as part of the PyCBC package [153]. Our changes beyond the `ihope` pipeline are implemented in PyCBC for use in upcoming LIGO and Virgo observing runs. Sec. 7.4 describes how each of our proposed changes affects the sensitivity of the search pipeline. Finally, Sec. 7.5 shows the overall improvement from each of these changes and we suggest directions for further possible improvements to the search pipeline.

7.2 Coincident Matched-Filter Search for Compact Binaries

We start with configuration of the search pipeline used in S6/VSR2,3. While the basic steps remain the same, different choices can be made to create various configurations and topologies for the search pipeline. In this chapter, we propose and test several changes to the search pipeline used in the S6/VSR2,3 search for low-mass compact binaries. For each proposed improvement, we use the methods described in Sec. 7.3 to assess the impact on the search sensitivity. The results of these tests are presented in Sec. 7.4. Fig. 35 summarizes these modifications, and contrasts the workflow of the `ihope` pipeline used in S6/VSR2,3 with our proposed new pipeline. Each color in the figure represents a modification to the pipeline, as described below.

We first change the workflow of the pipeline from a two-stage pipeline to a single-stage pipeline, shown by the yellow section of Fig. 35 and described in Sec. 7.4.1. In the `ihope` pipeline, a coincidence stage was applied after computing the matched filter

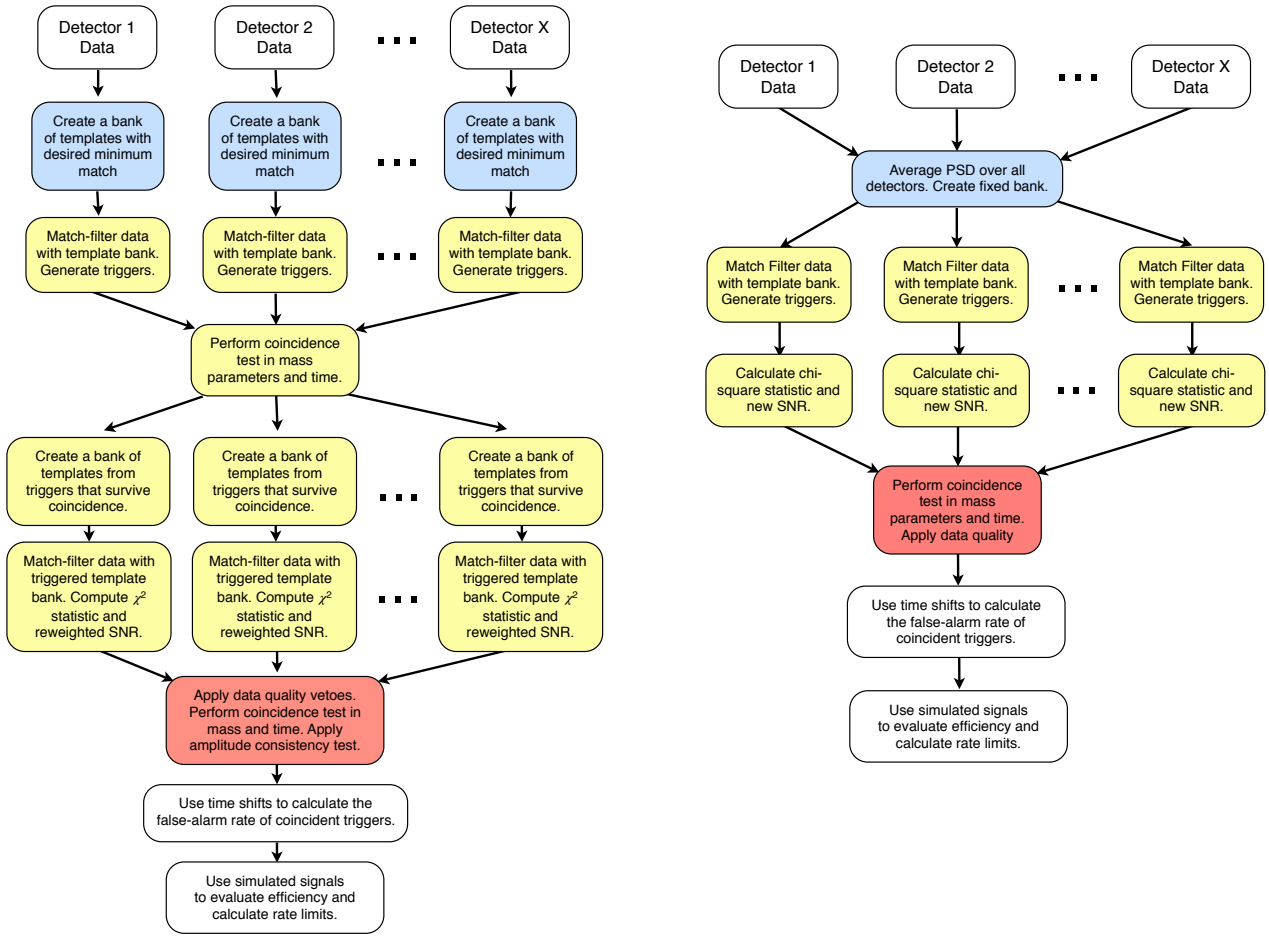

Figure 35: These flowcharts describe the topologies for the pipeline used in the S6 search (left) and the final configuration described here (right). Each color represents a distinct modification made to the pipeline described in the different sections in the chapter. The yellow is described in Sec. 7.4.1, the blue in Sec. 7.4.3 and the red in Sec. 7.4.4.

signal-to-noise ratio, but before computing the χ^2 statistic. The two-stage pipeline was created in order to avoid performing the computationally expensive χ^2 test on gravitational-wave candidates that were caused by noise and would be removed by the computationally cheaper time coincidence test. However, this lead to difficulty when estimating the significance of loud gravitational-wave candidates: only candidates surviving the second round of coincidence testing had the χ^2 test performed and thus the reweighted signal-to-noise ratio detection statistic calculated. The single-stage pipeline computes χ^2 before coincidence, so that the reweighted signal-to-noise ratio is available for all single-detector triggers, allowing the pipeline to estimate the false-alarm rate of loud candidates.

We then propose two changes to the placement of the template bank, shown by the blue section of Fig. 35. We change the bank construction from using a metric accurate to 1.5 post-Newtonian order [52] and the placement technique of Ref. [53] to using a metric accurate to 3.5 post-Newtonian order [149] (the same order as the template waveforms) and the placement methods described in Ref. [55]. We also investigate several different methods of generating the average power spectral density of the detectors used to construct the placement metric, including fixing the power spectral density for bank construction for a week of data, and averaging the noise spectrum between the two LIGO detectors, so that a shared bank is used in all detectors. Considering the noise properties of S6 data, we chose the lower-frequency cutoff for bank generation and filtering to be 40 Hz, and the boundaries of the template bank are specified by $1\,M_\odot \leq m_1, m_2$ and $m_1 + m_2 \leq 25 M_\odot$.

It is possible to construct several different types of tests for signal coincidence: early LIGO analyses used a simple, independent check on the consistency of the time of arrival and mass. Ref. [154] introduced a new method, applied to later analyses, including searches using S5, S6, and Virgo data, that uses the template bank metric to construct an ellipse of a given size around a trigger. Overlap of these ellipses is then used to determine if triggers are coincident.

Finally, in Sec. 7.4.4, we investigate a new type of coincidence test, shown by the red boxes in Fig. 35 and compare it to the ellipsoidal coincidence method, as used in the S6/VSR2,3 search. This test uses the method of Ref. [154] to determine if the triggers are consistent in time, but requires that the mass parameters of the signal are exactly the same in the detectors. This test naturally requires using a shared

template bank between detectors, which we construct using the best proposed power spectral density averaging method.

We test these improvements using two metrics for the performance of the search pipeline: (i) the ability of the different search pipelines to detect a distribution of simulated signals injected into the data, called *software injections*, and (ii) comparing the distribution of coincident triggers from real LIGO data to that of Gaussian noise. The next section describes how these tests are performed.

7.3 Testing Improvements to the Search

To test the proposed pipeline improvements, we use data from the S6 LIGO science run [15]. Since it is planned that the first aLIGO offline search will analyze one-week intervals of data, we test the search pipeline on one-week time intervals. To obtain two representative times, we examined the sensitivity of the detector, as measured by the detector's range to a binary neutron star system which would produce a signal-to-noise ratio of 8 in a single detector. The BNS inspiral horizon distance, shown in Fig. 36, is calculated from the detector's power spectral density [15]. Therefore, a variation in the power spectral density leads to a change in the inspiral horizon distance. For our analysis, we chose the time interval, July 08 to July 15, 2010 (blue rectangle in Fig. 36), as a week when the sensitivity of the detectors changed considerably. We also investigate a second time interval of L1 and H1 data, the week from August 14-21, 2010 (black rectangle in Fig. 36) with a more stable range to verify our results. We also re-analyzed these two weeks replacing the LIGO data with simulated stationary Gaussian noise, colored with the design spectrum of the initial LIGO detectors. To compare the performance of the pipeline in real data to its performance in Gaussian noise, we show histograms of the combined reweighted signal-to-noise ratio for coincidence background candidates obtained from analyzing Gaussian noise and from analyzing LIGO data. These histograms allow us to determine the search pipelines' ability to eliminate non-Gaussian noise transients in the LIGO data.

As the primary metric of search sensitivity, we measure the sensitivity of a pipeline by finding the *sensitive volume*, which is proportional to the number of detections a pipeline will make per unit time at a given false-alarm rate. We use a simulated population of signals to assess the sensitive volume. Masses are distributed uniformly

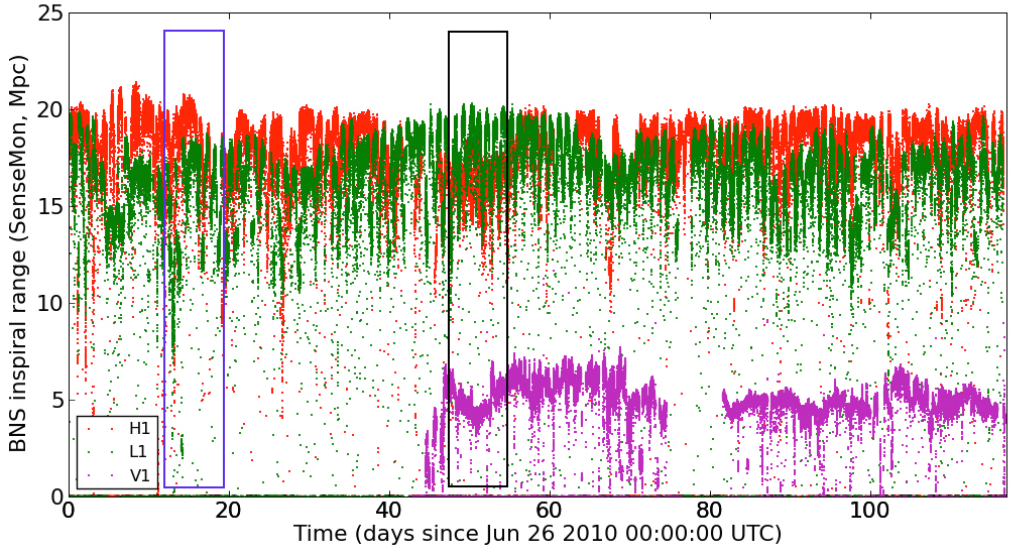

Figure 36: Sensitivity of the gravitational-wave detectors for the last part of the sixth science run for LIGO (S6D) and the third VIRGO science run (VSR3). The plot shows the volume-weighted average distance at which a 1.4, 1.4 BNS would be observed with an signal-to-noise ratio of 8 for each detector. The two rectangles indicate time intervals used for this study.

in component mass, with the bounds dependent on the type of compact object: $m \in [1, 3]\,\mathrm{M}_\odot$ for neutron stars (NS); $m \in [1, 13]\,\mathrm{M}_\odot$ for black holes (BH). We also restrict the total masses of binaries to be $\leq 14\,\mathrm{M}_\odot$. We allow template banks to extend to a total mass of $25\,\mathrm{M}_\odot$, as shown in Fig. 37. We assume approximately equal rates of BNS, NSBH, and BBH systems. Injections are generated at 3.5 PN order in the time domain using the TaylorT4 approximant. We find that $r_{\mathrm{min}} = 0.5\,\mathrm{Mpc}$ and $r_{\mathrm{max}} = 30\,\mathrm{Mpc}$ are reasonable bounds for a binary in which both component masses are $1.4\,\mathrm{M}_\odot$.

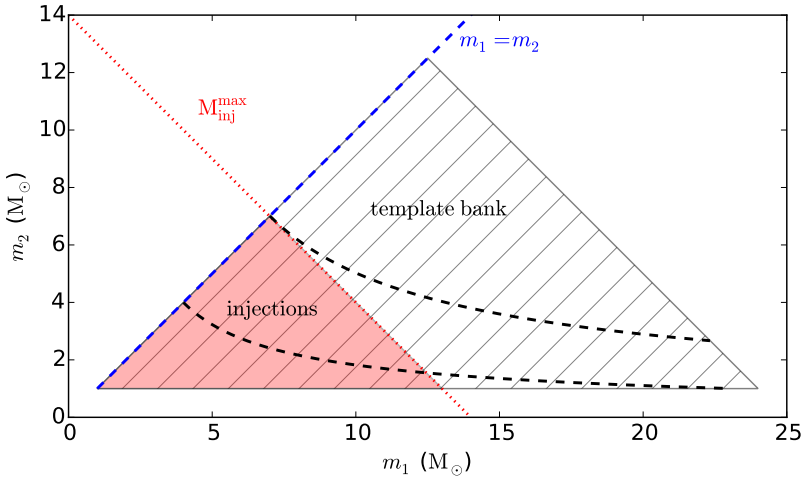

Figure 37: Mass-ranges for software injection, shown in the $m_1 - m_2$ mass-plane. As customary, we restrict to $m_1 \geq m_2$. The template bank used to search for these injections is indicated by hatched regions and the injection set by the red shaded region. The black dashed line shows a chirp mass of 3.48 $M_\odot$, the boundary between the two mass bins used. Triggers from templates with chirp masses larger than 6.1 $M_\odot$ are discarded in post-processing.

7.4 Search Sensitive Volume Comparison

We have performed a total of eight different analyses to test our proposed changes. These are summarized in Table 3. The first analysis used the two-stage `ihope` search pipeline in the same configuration originally used in the S6/VSR2,3 search for low-mass compact binaries. Each successive analysis represents a single modification from the previous search. Thus, the effect each change has on the search pipeline's

sensitivity can be individually noted. For each analysis, we compute the sensitive volume as a function of false-alarm rate, and for analyses 1, 2, and 7 we also compare the distribution of background triggers in LIGO data to that of Gaussian noise.

<table>
<tr><th>Analysis</th><th>Pipeline</th><th>Bank Metric</th><th>Bank PSD estimation</th><th>Detector banks</th><th>Bank PSD Averaging</th><th>Coincidence</th></tr>
<tr><td>1</td><td>Two-stage
<code>ihope</code></td><td rowspan="2">1.5 pN</td><td rowspan="4">Regenerated every 2048 s</td><td rowspan="4">Separate</td><td rowspan="3">N/A</td><td rowspan="6">Ellipsoid</td></tr>
<tr><td>2</td><td>Single-stage
<code>ihope</code></td></tr>
<tr><td>3</td><td rowspan="6">Single-stage
<code>PyCBC</code></td></tr>
<tr><td>4</td><td rowspan="5">3.5 pN</td></tr>
<tr><td>5</td><td rowspan="2">Harmonic</td></tr>
<tr><td>6</td><td rowspan="3">Fixed for week</td><td rowspan="3">Shared</td></tr>
<tr><td>7</td><td>Smallest-Value</td></tr>
<tr><td>8</td><td>Harmonic</td><td>Exact-match</td></tr>
</table>

Table 3: Overview of the eight different analysis performed to test improvements to the search pipeline in this chapter. Each successive analysis incorporates a change from the previous search pipeline. The pipeline column indicates the pipeline workflow and the software used to run the search. The bank metric column indicates whether templates are placed using a metric accurate to 1.5 pN or 3.5 pN order. The bank power spectral density (PSD) estimation column indicates whether the template bank was placed using a power spectral density re-computed every 2048 seconds, or if the search used one fixed template bank for the entire week. The detector banks column indicates whether a separate template bank was generated for each detector, or if the template bank was shared by both detectors. For fixed template banks, the bank power spectral density averaging column gives the type of power spectral density averaging used over the week to generate place the bank. The coincidence column indicates whether the analysis used the ellipsoidal coincidence method or the exact-match coincidence method.

7.4.1 Single-Stage Pipeline Workflow

Our analysis begins with pipeline used in LIGO's sixth science run. This pipeline, shown on the left in Fig. 35, was a two-stage pipeline, so called because there are two times that the coincidence test is applied. The two-stage process was created in order to avoid performing the computationally expensive χ^2 test on gravitational wave candidates that were caused by noise and would be removed by the computationally

cheaper time coincidence test. For this reason, the coincidence test was performed before the χ^2 test.

The two-stage `ihope` pipeline was very effective at downweighting the significance of triggers due to noise. Fig. 38 shows two histograms of gravitational-wave candidates as a function of reweighted signal-to-noise ratio that survived time-lagged coincidence tests. The red lines in the figure are from an analysis of Gaussian noise, while the black lines denote an analysis of real LIGO data. The plots demonstrate that the two-stage pipeline downweights significant noise-generated triggers to the point that the LIGO data is very close to the analysis of Gaussian noise.

However, the two-stage workflow led to difficulty when estimating the significance of surviving gravitational-wave candidates: only candidates surviving the second round of coincidence testing had the χ^2 test performed and thus the new detection statistic calculated. In the S6/VSR2,3 search the pipeline used 100 time shifts, each with a 5 second offset, limiting the significance that can be measured. For loud gravitational-wave candidates, further background estimation must be performed to calculate false-alarm rates at less than one in a thousand years. To calculate this extended background, the data is offset by multiples of 0.2 seconds to perform a coincidence test. This is done as many times as possible, and the resulting coincident triggers are used to estimate a false-alarm rate. computing as many time shifts as possible, while coincident data remains.

In the S6/VSR2,3 analysis, applying this extended background estimation required re-analysis of the data with the χ^2 test turned on at the first stage, eliminating any computational savings of the two-stage pipeline. Furthermore, although the output of the two-stage pipeline should be identical to a single-stage pipeline, in practice the two-stage pipeline does not produce the same triggers. This is primarily due to the fact that the single-detector triggers are clustered in a 30 ms window over the template bank after the first matched-filtering jobs, and then fed back into the search as a new bank after coincidence [59]. This non-linearity adds additional complication when testing and tuning the pipeline.

For both of these reasons, although primarily for the false alarm-rate considerations, it is desirable to abandon the two-stage pipeline and switch to a simpler single-stage workflow, as shown on the right in Fig. 35. The single-stage pipeline essentially rearranges the previous pipeline computing the χ^2 test before the coincidence test and

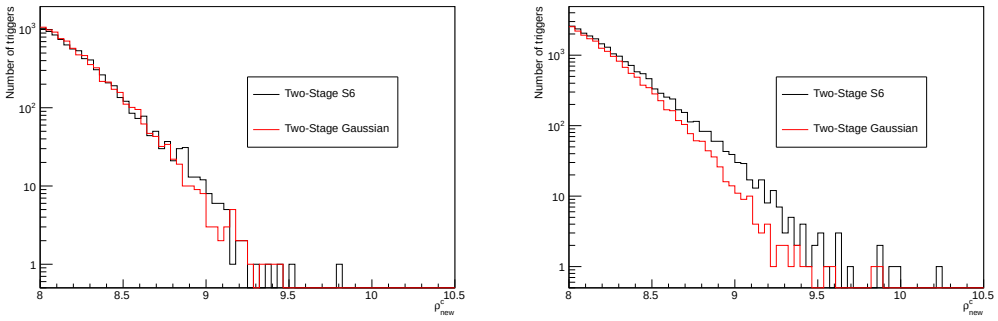

Figure 38: This histogram shows the number of background triggers that survived coincidence testing from the two-stage analyses. They are categorized in bins of combined reweighted signal-to-noise ratio. The left plot represents an analysis of a week of data from July 2010 while the right plot represents an analysis of a week of data from August 2010. The red line denotes the background triggers from the Gaussian analysis. The black line denotes the background triggers from the first S6 data analysis.

removing the triggered template bank generation and the second match-filter process. Fig. 39 shows the background triggers as a function of reweighted signal-to-noise ratio of the single-stage analysis of S6 data compared to a those of a single-stage analysis of Gaussian data. Like the two-stage pipeline's performance shown in Fig. 38, we see the single-stage pipeline is also successful in removing candidates with high significance. The single-stage pipeline is expected to perform identically to the two-stage pipeline. Fig. 40 compares the sensitive volumes of these search pipelines. The sensitive volume measurement for the two-stage pipeline terminates at a false-alarm rate of order one per year, limited by the 100 time-slides performed by the two-stage pipeline. However, with the single-stage pipeline, many more time-slides can be performed and the false-alarm rate of injections can be computed down to of order $1/10,000$ years using one week of data. We can see that in the region where both can compute the false-alarm rate of triggers, the sensitivities of the two pipelines agree as expected.

As described above, the primary motivation for the two-stage pipeline was to mitigate the computational cost of the signal-based vetoes. If triggers are found above threshold, the χ^2 time-frequency signal consistency test is applied. The test consists of breaking the waveform into p frequency bins of equal power. Each bin is filtered against the data to obtain the partial signal-to-noise ratio contribution ρ_l

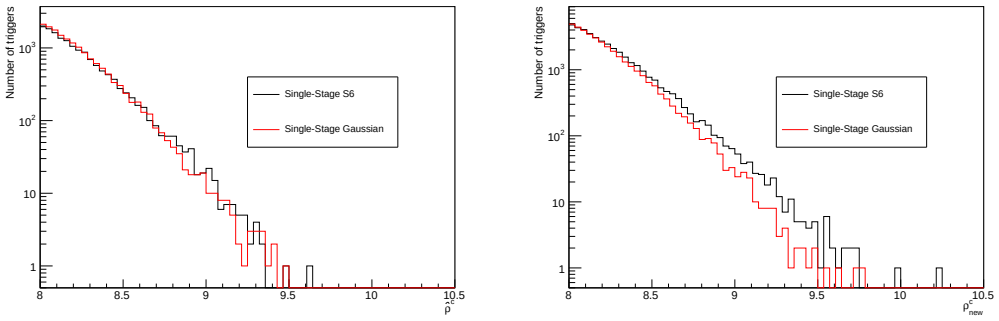

Figure 39: This histogram shows the number of background triggers that survived coincidence testing from the single stage analyses in different bins of combined reweighted signal-to-noise ratio. The left plot represents a week analysis of data from July 2010 while the right plot represents an analysis of a week of data from August 2010. The red line denotes the background triggers from the Gaussian analysis. The black line denotes the background triggers from the first S6 data analysis.

and then compared to the expected signal-to-noise ratio contribution ρ/p. In the `ihope` pipeline, the value of the χ^2 statistic was computed as a function of time for a template if there were any signal-to-noise threshold crossings in the 2048 second block of analysis time. The calculation of the p filters for each bin requires a single inverse complex Fast Fourier Transform, and neglecting lower-order terms, we find a cost of $pN\log(N)$. However, as we know the location of peaks, we can also directly calculate this test only for those points. We illustrate the method by considering a single-phase of the signal-based veto given in Eq. (2.8). We can express the quantity that needs to calculated in terms of existing information as

$$\frac{\chi^2+\rho^2}{p}[j] = \sum_{l=1}^{p} \rho_l^2, \tag{7.1}$$

which can be written as

$$\frac{\chi^2+\rho^2}{p}[j] = \sum_{l=1}^{p} \left(\sum_{k=k_l^{min}}^{k_l^{\max}} \tilde{q}_k e^{-2\pi i j k/N} \right)^2, \tag{7.2}$$

where $[j]$ is the set of indices of the N_p peak values, and $\tilde{q}_k = \tilde{h^*}_k \tilde{s}_k$. Naively, this

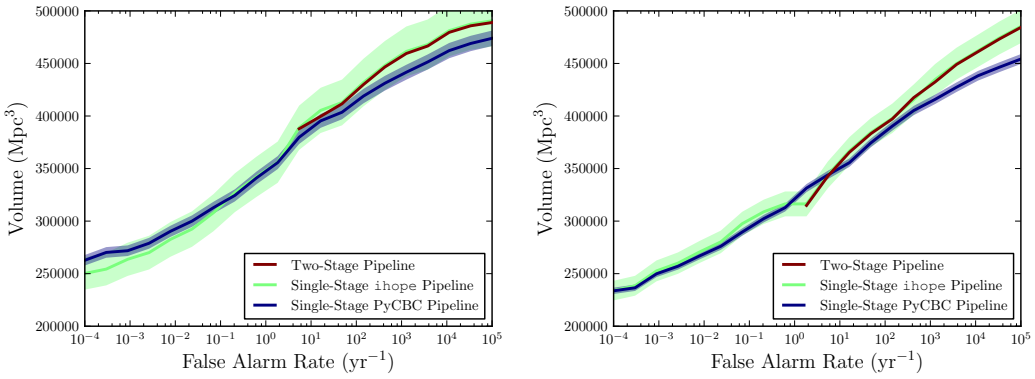

Figure 40: This plot gives the relative sensitive volume of the two-stage analysis to the single-stage analysis as a function of the false-alarm rate In the region above a false-alarm rate of ~ 2 per year, where both pipelines can measure the false-alarm rate of candidates, the sensitivity of the two pipelines is the same. By performing many more time shifts to estimate the background, the single-stage pipeline can estimate the significance of triggers to a false-alarm rate of $\sim 10^{-4}$ per year using one week of data. We also include an analysis with the same pipeline workflow as the single-stage pipeline, but that uses the new `PyCBC` search code, instead of the previously-used `ihope` code. The error bars on the `PyCBC` search are smaller, as the increased computational efficiency of this pipeline allows us to perform an order of magnitude more injections. However, the results otherwise agree. The left plot represents an analysis of a week of data from July 2010 while the right plot represents a week analysis of data from August 2010.

expression involves the explicit calculation of $k_{\max}$ root-of-unity complex multiplicative constants. However, the computational cost can be reduced to a single complex multiply by pre-calculating a single root-of-unity complex multiplicative constant and iteratively finding the next. To do this, we write the expression in the following form:

$$\frac{\chi^2 + \rho^2}{p}[j] = \sum_{l=1}^{p} \left(\sum_{k=k_l^{min}}^{k_l^{\max}} \tilde{q}_k (e^{-2\pi i j/N})(e^{-2\pi i j k/N})^{k-1} \right)^2 . \tag{7.3}$$

This reduces the computational cost to two complex multiplies, one for the root-of-unity complex multiplicative constant and one for the multiplication by $\tilde{q}$; which combined with the summing of two complex numbers gives a total cost of $14k_{\max} * N_p$. For small values of N_p we note that this can be vastly more efficient than the full FFT based calculation of the veto. The crossover point can be estimated as

$$N_p = \frac{p * 5N \log(N)}{14k_{\max}}. \tag{7.4}$$

This equation is only a rough guide because the computational cost of an FFT is highly influenced by its memory access pattern, but for our typical configuration where $N = 2^{20}$, it would predict the new algorithm to be more efficient whenever the number of points at which the χ^2 statistic must be evaluated is less than approximately 100. The cost savings can therefore be quite large for data stretches that are clean enough that the number of candidate triggers is *much* less than this crossover. This method has been implemented in the new `PyCBC` search pipeline and is used in the second single-stage analysis presented here. We have configured `PyCBC` to produce a search pipeline that is identical to the single-stage `ihope` pipeline, with the exception of adding the more computationally efficient implementation of the χ^2 test described above. The performance of this search is shown as the third curve in the sensitive volume plot in Fig. 40. As expected, the performance of this search is essentially identical to the single-stage `ihope` pipeline. Table 4 compares the computational cost of the two-stage `ihope` pipeline to the single-stage `PyCBC` pipeline. We see that the reduction in cost of the χ^2 veto results in a pipeline that can compute the reweighted signal-to-noise ratio for all single detector triggers, at the same computational cost of the two-stage pipeline.

Job Type	Two-Stage `ihope`	Single-Stage `PyCBC`
Computing Injection Parameters	0.0	0.0
Template Bank Generation	13.3	4.7
Match-filtering and χ^2	515.4	515.5
Second Template Bank	0.1	-
Coincidence Test	0.3	9.9
Total	529.1	530.0

Table 4: This table details the computational costs of different parts of the listed search pipelines. The costs are given in CPU days.

Finally, Fig. 39 shows the background triggers as a function of reweighted signal-to-noise ratio for the single-stage `PyCBC` analysis of S6 data compared to analysis of Gaussian data. Like the two-stage pipeline's performance shown in Fig. 38, we see the single-stage pipeline is also successful in removing candidates with high significance and results in a trigger distribution that is close to Gaussian. Given the success of this analysis, all subsequent analyses here use the single-stage `PyCBC` pipeline.

7.4.2 Post-Newtonian Order of the Bank Metric

The next analysis used a bank of waveforms placed at 3.5 PN order, while the previous analysis placed templates at 1.5 PN order. While a new placement algorithm was used, the same minimum match between template waveforms was required. As with the single-stage and two-stage volume plot, the higher line indicates a larger sensitive volume and a more efficient pipeline. The 1.5 and 3.5 PN template placement produces similar sensitivities for signals at low false-alarm rate, while the 3.5 PN placement is slightly better for signals at high false-alarm rate. We can see this from the volume plot in Fig. 41 This suggests that the PN order of template placement does not have a significant effect on the sensitivity of the pipeline. For symmetry with the templates used (which are 3.5 PN order), we configure the pipeline to use 3.5 PN template placement in our subsequent analyses.

7.4.3 Power Spectra Used for Bank Placement

Since the shape of the detector's power spectral density changes over time, the S6/VSR2,3 analysis recomputed the noise power spectral density used in the matched

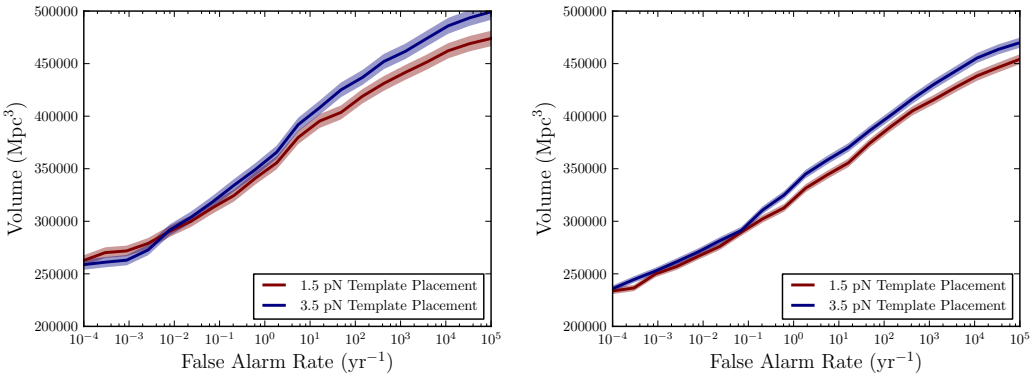

Figure 41: This volume plot compares the analysis with a 3.5 PN bank to our previous analyses with a 1.5 PN bank week of S6 data. The red line shows that of the single-stage analysis with a 1.5 PN bank and the blue line shows the single-stage analysis with a 3.5 PN bank. The left plot represents a week analysis of data from July 2010 while the right plot represents an analysis of a week of data from August 2010.

filter every 2048 seconds. Furthermore, the template banks used in the search were also regenerated on the same cadence. Since the power spectral densities of the detectors in the network are not the same, the template bank was computed independently for both detectors. Since the placement of templates is not identical between detectors, the pipeline must use a coincidence test that allows for mismatch between the mass parameters of a signal. We investigate an alternative method for generating and placing the template bank. Rather than re-generating the bank every 2048 seconds, we explore the creation of a single, fixed bank for the entire duration of the (one week) analysis by averaging the detector's noise power spectral density over the full analysis time and using this globally averaged power spectral density to place the template bank.

We initially try independently averaging the power spectral density from each detector, creating separate banks for each detector. We then test the use of a single, fixed bank for both detectors by further averaging the power spectral density between the two detectors. Using a bank shared between detectors allows us to use a new coincidence testing code, described in Sec. 7.4.4 which requires the mass parameters to be identical in a coincident trigger. To compare the different power spectral density estimations, we tested several different averaging methods and compared their relative

sensitive volumes. We begin by considering several methods to average the power spectral density over a week of gravitational-wave data. The methods used are:

1. Separate Harmonic Mean. We first create a single bank for each detector for the duration of the search. We measure the power spectral density of the noise every 2048 seconds to construct N power spectra S_n, as in the existing template placement. We then construct the harmonic mean power spectral density defined by averaging each of the separate f_k frequency bins according to

$$S_n^{\text{harmonic}}(f_k) = N \Big/ \sum_{i=1}^{N} \frac{1}{S_n^i(f_k)} \ . \tag{7.5}$$

   The use of the harmonic mean was motivated by Ref. [57] which shows that the harmonic sum of the individual detector power spectral densities in a network yields the same combined signal-to-noise ratio as a coherent analysis of the detector data. The harmonic mean $S_n^{\text{harmonic}}(f_k)$ is then used to place a single template bank that is used for the entire search using one week of data. Our first test generated an independent harmonic mean power spectral density for each detector, and so separate template banks were generated for each detectors. These banks are used for match-filtering in their respective detectors and the resulting gravitational-wave candidates undergo a coincidence test between detectors using the ellipsoidal coincidence test.

2. Shared Harmonic Mean. We next average the power spectral density between the two detectors to create a single template bank that is shared by both detectors (i.e. each detector shares exactly the same templates from a single bank). This fixed bank was averaged over the week-long data set and was used for the entire analysis. After being match-filtered against the data and the gravitational-wave candidates identified, the ellipsoidal coincidence test is applied.

3. Shared Smallest-value Estimation. Our last configuration created a single bank between the two detectors while choosing the smallest value for the power spectral density. The smallest value in each frequency bin represents the best performance of the detector. The template banks generated by the smallest value

power spectral density give typically a higher number of templates than the other averaging methods. Thus by using the smallest value for each bin of the power spectral density, we can create the most densely packed bank of templates possible.

Fig. 42 shows the power spectral density computed for a week of data using these different averaging methods and the difference of these methods to the arithmetic mean of the power spectral density.

To test how each of these banks affect the search sensitivity, we performed several analyses with these different averaging methods. The results of these investigations are shown in Fig. 43 which compares the sensitive volume as a function of false-alarm rate. For the first week of data from July 2010, which has large fluctuations in the inspiral range, the fixed template banks have approximately the same sensitivity as the regenerated template banks for high estimated false alarms rates. For false-alarm rates of $\sim 10^{-3}$ per year, the bank generated using the fixed harmonic-mean power spectral density gives the best sensitive volume. For the second week of data from August 2010, which has a more stable inspiral range, all of the bank placement methods have the same sensitivity, within measurement error. In the case when fixed banks provide increased sensitivity, the harmonic mean gives the best sensitivity, so we recommend this averaging method for the search.

We also note that using a fixed template bank reduces the overall computational cost of the search. Table 4 shows that the cost of generating the template banks used here is a small fraction of the overall run time of the search. Fixing the template bank essentially eliminates this cost, but since the cost of the bank generation is less than 1% of the overall computational cost, this is not a significant saving. However, for searches that incorporate compact-object spin in the waveform templates, template bank generation can be significantly more expensive [100, 55, 153]. For example, for searches for binary neutron stars between 1–3 $M_\odot$ and dimensionless spins up to $\chi \leq 0.4$, or for neutron star–black hole binaries with black holes masses between 3 and 15 $M_\odot$ and spins up to $\chi = 1$, the cost of generating the template bank is three to four orders of magnitude more expensive than the cost of the bank used here (depending on the low-frequency sensitivity of the detector). However, the number of templates in the bank, and hence the cost of matched filtering, only increases by a factor of 2–5. If the template bank is re-generated every 2048 seconds for searches

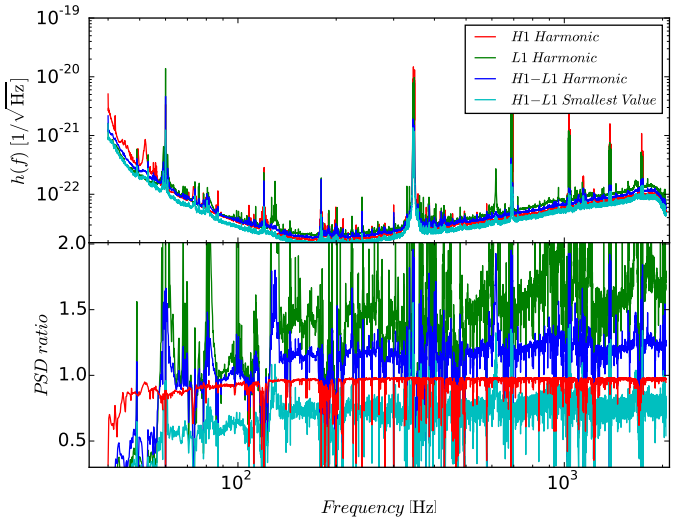

Figure 42: The top panel shows the power spectral densities for different averaging methods of the measured power spectral densities for the one-week time interval July 08-15, 2010 for the LIGO Livingston (L1) and LIGO Hanford (H1) detectors. The lower panel demonstrates the ratio of the different power spectral densities to the arithmetic mean power spectral density of the LIGO Hanford Detector.

for binaries with spin, bank placement can become a significant fraction of the overall search cost. The power spectral density averaging methods proposed here to generate a fixed template bank can be applied to those searches, significantly reducing the computational cost [153].

7.4.4 Trigger Coincidence Test

Since the S6/VSR2,3 search used separate regenerated template banks for each detector, a coincidence test that allows triggers to have slightly different mass parameters must be used in the search. The template placement metric was used to construct the ellipsoidal coincidence test which determines if two waveforms are coincident in time and mass between detectors [154]. Tuning the size of the ellipsoidal coincidence test is performed empirically by calculating the distribution of the ellipsoidal coincidence window for simulated signals and for noise events from the background time shifts, and choosing a value of the parameter controlling the size of the ellipse that provides the best separation of signals and background.

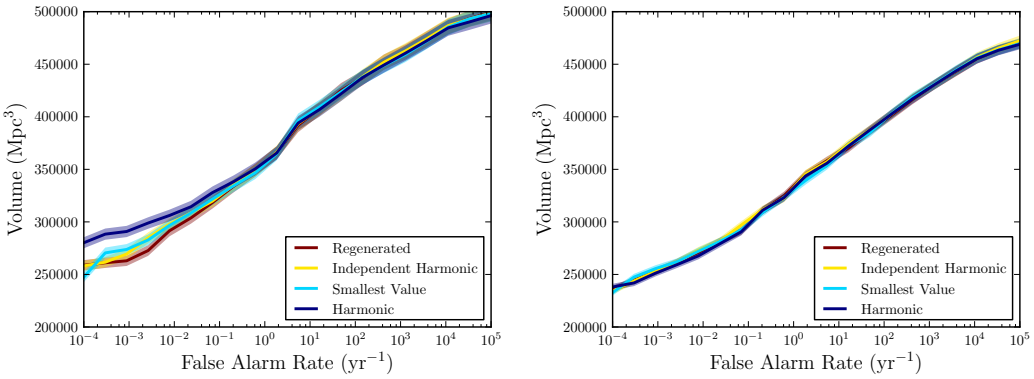

Figure 43: This volume plot describes the sensitive volumes of the searches in different configurations. The red line is an analysis using template banks regenerated every 2048 s. The blue, yellow and cyan lines show different analyses with fixed banks. The blue and yellow used a harmonic mean to estimate the power spectral density, while the cyan simply chose the lowest power spectral density measured at each frequency. The regenerated-bank and the independent-harmonic analyses used separate banks for the different detectors, while the smallest-value and harmonic analyses used a common bank for both detectors. The left plot represents an analysis of a week of data from July 2010 while the right plot represents a week analysis of data from August 2010.

Using a shared, fixed bank for both detectors allows us to investigate a new, simpler type of coincidence test. In this *exact-match* coincidence test, we use the ellipsoidal window to determine if triggers are coincident in time, since there is still a time-of-flight difference between triggers in the detectors, however we require that the mass parameters m_1 and m_2 of the template are exactly the same in both detectors. This requirement decreases the chance that triggers generated by noise transients will be found in coincidence between detectors, as it is a stricter test than the ellipsoidal test. The exact-match method of testing for coincidence is useful in situations where there is no simple metric to compare gravitational waveforms, as is the case with template waveforms for binaries with spinning neutron stars or black holes [153].

In Fig. 44, we compare the performance of the search on two weeks of S6 data using the same, fixed harmonic bank in both detectors, but using either the ellipsoidal coincidence test or the exact-match coincidence test. The ellipsoidal coincidence test tends to recover injections with higher combined reweighted signal-to-noise ratio than exact-match test: the less stringent ellipsoidal coincidence test allows more templates in each detector to contribute to coincidence, thus there is more chance of an upwards fluctuation in the detection statistic. The gain in sensitivity from the exact-match test is a tradeoff between the (on average) smaller signal-to-noise ratio of signals and the lower background level, giving an increase in detection significance at a given signal-to-noise ratio. For the week from July 2010, the performance of the exact-match coincidence test is slightly better than that of the ellipsoidal test, although the difference is within the error bars at a false-alarm rate of 10^{-3} per year. However, for the week from August 2010, the sensitivity of the search using the exact-match test is clearly higher at a false-alarm rate of 10^{-3} per year.

We can understand this increase using Figs. 45 and 46, which compare histograms of the combined reweighted signal-to-noise ratio of background triggers obtained in S6 data to Gaussian noise. For the first week of data, the distribution of background triggers using the ellipsoidal coincidence test, shown in Fig. 45, is very close to that of Gaussian noise. However, for the second week, the S6 data contain more triggers at higher combined reweighted signal-to-noise ratio. This difference can still be seen in Fig. 46, which shows the distribution of background triggers from the exact-match coincidence test. Note, also, that in the exact-match analysis, the overall rate of triggers is significantly lower for both weeks, resulting in lower false-alarm rate at a

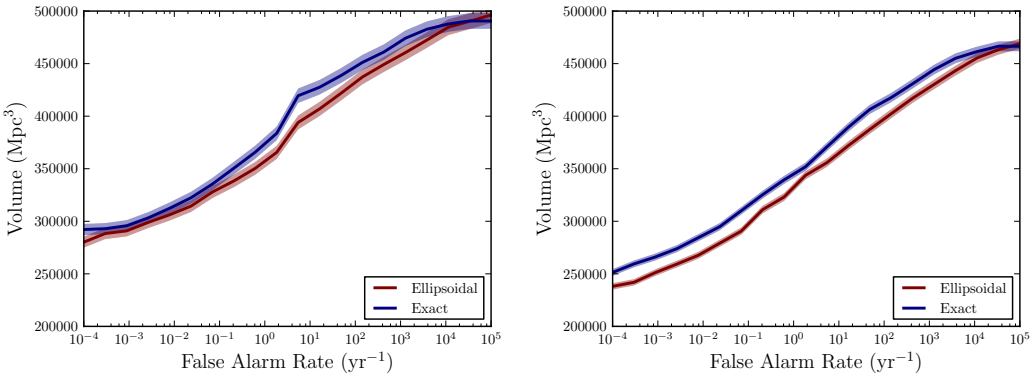

Figure 44: This volume plot describes the relative sensitive volumes of the different search pipelines as a function of false-alarm rate. The red curve describes the sensitivity of a search pipeline using the ellipsoidal coincidence test. The blue curve demonstrates the sensitivity of the search pipeline using a fixed bank and the new exact-match coincidence test. The left plot represents a week analysis of data from July 2010 while the right plot represents an analysis of a week of data from August 2010.

given value of combined reweighted signal-to-noise ratio. Our results show that the lowering of the noise background with exact-match coincidence is the dominant effect: signals are recovered with greater significance, raising the search sensitivity.

7.5 Conclusions

We have demonstrated the use of a new pipeline to search for gravitational waves from compact object binaries in LIGO data. The results of our study are summarized in Fig. 47 which compares the sensitivity of the search pipeline used in S6/VSR2,3 (analysis 1 of Table 3) with the most sensitive pipeline proposed here (analysis 8 of Table 3) which uses a shared fixed 3.5pN template bank in both detectors generated using a harmonic mean power spectral density, and the exact-match coincidence test. We see that these improvements result in a gain of $\sim 10\%$ in the sensitive volume of the search at a false-alarm rate of 10^{-3} per year. The new pipeline uses a simpler, single-stage workflow that allows us to estimate false-alarm rates to $\sim 10^{-4}$ per year using one week of data. With our improved implementation of the χ^2 signal-based veto, we demonstrate that the new pipeline has the same computational cost as the two-stage workflow used in the S6/VSR2,3 analysis. We propose that this workflow

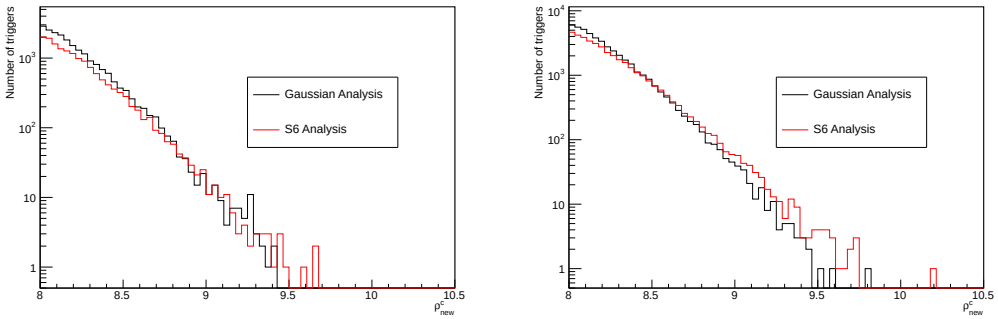

Figure 45: This histogram shows the number of background triggers that survived coincidence testing from the analysis using a shared, fixed harmonic bank using ellipsoidal coincidence testing in different bins of combined reweighted signal-to-noise ratio. The red line denotes the background triggers from the Gaussian analysis. The black line denotes the background triggers from the S6 data analysis. The left plot represents an analysis of a week of data from July 2010 while the right plot represents a week analysis of data from August 2010.

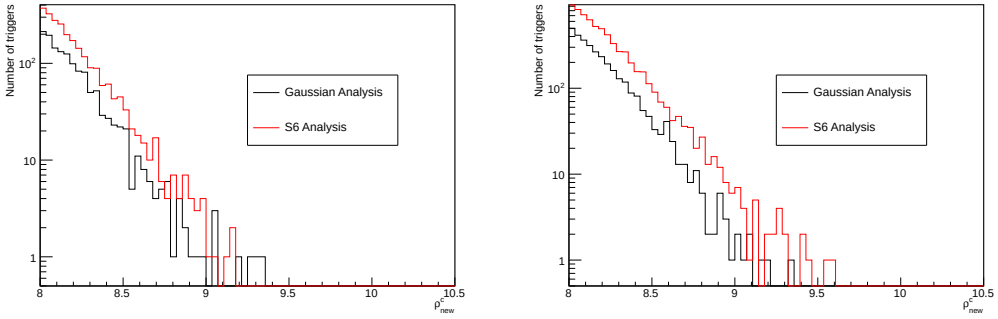

Figure 46: This histogram shows the number of background triggers that survived coincidence testing from the analysis using a shared, fixed harmonic bank using `exact-match` coincidence testing in different bins of combined reweighted signal-to-noise ratio. The red line denotes the background triggers from the Gaussian analysis. The black line denotes the background triggers from the S6 data analysis. The left plot represents an analysis of a week of data from July 2010 while the right plot represents an analysis of a week of data from August 2010.

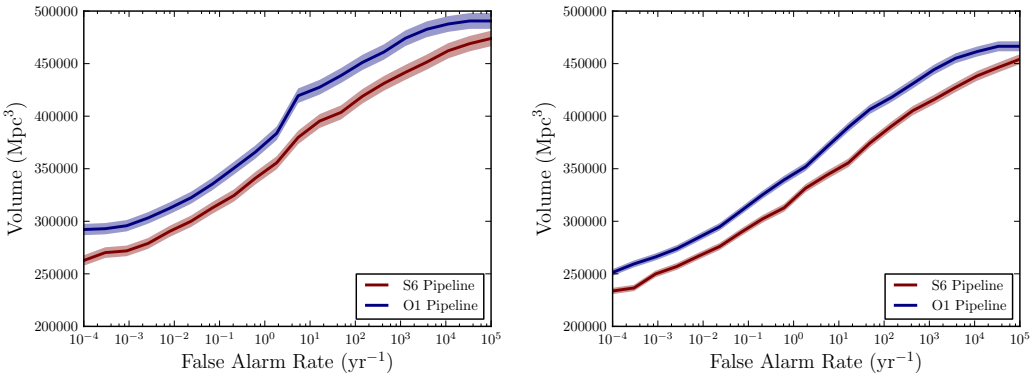

Figure 47: This volume plot describes the relative sensitive volumes of the different search pipelines as a function of false-alarm rate. The red curve describes the sensitivity of the search pipeline used in LIGO's sixth science run, reformatted to have a single coincidence test. The blue curve demonstrates the sensitivity of the search pipeline using a fixed bank and the new exact-match coincidence test. The left plot represents an analysis of a week of data from July 2010 while the right plot represents an analysis of a week of data from August 2010.

be used as a basis for offline searches for gravitational waves from compact-object binary sources in aLIGO and AdV.

We note that a new class of search pipeline was prototyped in S6/VSR2,3 [66] that produces triggers in low-latency for rapid follow-up by electromagnetic observatories. These pipelines are under active development for aLIGO and AdV [155, 156]. Low-latency searches differ from the pipeline presented here as they are constrained to only use information available in the past and trade computational cost for speed of producing detection candidates. However, since they are based on coincident matched filtering, our results can also be used to inform the development of low-latency searches. For example, we would expect that the harmonic mean (using recent past detector data) would provide the best power spectral density estimation for the construction of template banks used in the singular value decomposition proposed in Ref. [156]. Similarly, we expect that exact-match coincidence would provide the best coincidence method for the low-latency pipelines.

Finally, we note that Figs. 45 and 46 show that, although the distribution of triggers in the S6 search using the ellipsoidal test is very close to that of Gaussian noise this is not the case for exact-match. This suggests that additional tuning is possible

to increase the sensitivity of the search. Investigation of improved tuning could explore the optimal length of time for a single bank, further tuning of the coincidence test, improvements to power spectral density estimation used in the matched filter, improved signal-based vetoes and optimization of the combined detection statistic. Further tuning beyond what is presented here will be the subject of future studies.

Chapter 8

Optimizing the Matched-filtering Implementation

8.1 Introduction

We consider the compuatational optimizations that we have made to the implementation of matched-filtering used in searches for compact binary coalescences. In S6/VSR2,3 the dominant computational cost of the ihope pipeline was the `lalapps_inspiral` filtering engine. Over the last two years, the ihope pipeline has been re-written for Advanced LIGO. The new framework, known as PyCBC is more modular, flexible, and scalable than the LALApps framework used previously. PyCBC has been developed to accommodate longer templates and larger template banks necessitated by the improved detector noise profile [153].

The PyCBC architecture implements the high-level program control in Python, however computations are performed using C code compiled just-in-time by the `scipy.weave` framework [157]. This ensures that all computationally intensive parts of the pipeline are executed by low-level, optimized code and not by the Python interpreter. Furthermore, direct AVX/SSE calls or OpenMP parallelization may be performed by use of the X86 intrinsic functions in the weave-compiled C-code. The Python frame work allow us to modularize the low-level kernels at low overhead. It is therefore straightforward to replace these kernels with code for new compute architectures including Graphics Processing Units (GPUs) and Intel® MICs (in addition

to architecture-specific CPU code) in the same search engine. As a result of this development, the the `lalapps_inspiral` filtering engine has been retired and replaced with the new `pycbc_inspiral` executable [56].

We discuss improved algorithms that implement the selected scientific methods. We have made performance improvements that can be realized independent of the architecture used (CPU or GPU). The improved algorithms generate *exactly the same output* as used in previous LIGO searches.

8.2 Optimization of thresholding and time clustering

After the matched filter SNR is computed for a given template, the resulting time series must be searched for points above a runtime-specified threshold to obtain gravitational-wave candidate triggers. Since both signals and glitches can produce many nearby SNR samples above threshold (which do not represent independent triggers), the SNR samples above threshold tend to be clustered in time. This leads to a high probability that there is a minimum spacing of a user-specified length (the clustering window) between any two consecutive clustered triggers. This window is chosen based on the impulse response of the filter and the character of the data, so that triggers produced come from independent events (noise or signal).

In `lalapps_inspiral` these two steps (thresholding and clustering) were implemented as separate kernels. We optimize this by fusing the two kernels. The primary motivation for this fusion is the thresholding step. Searching through an array for points above threshold is trivial to implement in serial, un-vectorized code. Vectorization or parallelization of this code must be done with care; the problem is equivalent to *stream compaction*, which is difficult to vectorize or parallelize without requiring at least two passes over the array to be compacted [158]. However, the number of floating point computations to be performed for each memory operation is very low, and so this kernel will be bandwidth limited; multiple passes over the array incur heavy performance penalties. The primary difficulty is that stream compaction takes its input array and writes out another array consisting of all elements of the input satisfying some criterion, consecutively. This cannot be vectorized or parallelized in one step, because the location to which the output should be written potentially depends on the calculation of all input array elements before any given element.

Fusing the array compaction and the clustering allows us to bypass this difficulty. The key idea is to find the maximum of the output over sub-arrays no longer than the clustering window, and write one output for each such window. We can do this in a single pass over the data, since the output destination is predetermined. We then cluster in a followup pass that looks at the maximum for each window. While that followup pass is not parallelized, in our typical configurations it looks at of order one hundred array elements, rather than a million, and so has trivial cost in comparison. This change greatly improves the performance of both CPU and GPU implementations, and the CPU particularly when multi-threaded FFTs are used to compute the matched filter.

8.3 CPU implementation and optimization

We now turn to the specific optimizations and implementation choices necessary for CPU architectures. For concreteness, we focus on the Intel® E5-2670 (Sandy Bridge) product.Our reference system has two sockets of eight cores each, running at 2.6 GHz clock speed. All performance results presented here, whether single or multi-threaded, were tested with the CPU affinity of the process set to bind it to a number of cores equal to the number of threads assigned to that process, and resident on the same CPU socket. CPU throttling and hyper-threading were also disabled for these tests. Each socket has a unified shared L3 cache of 20 MB, and each core has an L1 data cache of 32 KB, and an L2 cache of 256 KB. The architecture supports the AVX (but not AVX2) instruction set, and each core therefore has access to sixteen SIMD registers that can hold either eight single-precision or four double-precision floating point numbers. Potentially one add and one multiply instruction can be retired each clock cycle, so the maximum theoretical peak single precision performance of each socket is $2.6 \times 8 \times 8 \times 2 = 332.8$ GFLOPS.

Standard profiling tools can reveal where `pycbc_inspiral` spends most of its time, and timing tests can reveal whether we are in fact able to utilize the most efficient, multi-threaded FFT. Initially, that configuration did *not* give us the highest throughput per socket: the other kernels in the core matched filter were not well parallelized or vectorized and though their cost was small when the program was run in a single-threaded configuration, they became unacceptably slow when the FFT was

switched to the faster, multi-threaded configuration. Indeed these kernels before and after the FFT were sufficiently slow in their original implementation that not only did we not achieve close to the matched filter performance expected based on the FFT alone, we did not achieve the highest throughput by running in a multi-threaded configuration. We therefore began our CPU optimization by both vectorizing and parallelizing these kernels, and in the next sections we report in some detail on those changes, and the resulting performance improvements.

One expensive kernel remains that has not yet received a thorough optimization in its CPU implementation: the time-frequency χ^2 veto. This kernel is more complex and is also only a significant bottleneck when the data quality is poor enough that there are many candidate triggers per segment above threshold. Our next optimization target is a careful vectorization and parallelization of this algorithm. If the autocorrelation χ^2 veto is also shown to be necessary, we will also implement an optimized kernel for the algorithm.

8.3.1 Parallelization of expensive kernels

Both the correlation of the frequency-domain data segment with the frequency domain template (to produce the input to the inverse FFT) and the combined thresholding and clustering algorithm (described in Sec. 8.2 above, and acting on the output of the inverse FFT) are implemented in the pipeline as C-code kernels. These are parallelized with OpenMP and will dynamically adjust to run on all cores made available to the kernel. The optimal performance was achieved not by a straightforward `for` loop parallelization, but rather by parallelizing a loop that called another function to act on "chunks" of data, where the chunk size is chosen to maximize the amount of data that can fit in the L2 cache of each core.

The quality of parallelization is relatively easy to quantify: a given kernel is benchmarked running on a single core with all other cores idle, and that benchmark compared to the kernel executing on all cores of the socket. Again, we reiterate that we always set the CPU affinity of a kernel so that the operating system cannot dynamically migrate it. If the parallelization is optimal, then the ratio of the single-threaded execution to multi threaded should be the number of cores on the socket, in our case eight.

For correlation of the first half of two arrays of length 2^{20} with output written

to a third such array, the parallelized kernel executed on all eight cores in a time of 87.2 μs; the single-threaded kernel in 581 μs, for a ratio of 6.7. For the combined threshold-and-cluster kernel, the eight-threaded kernel executed in 69.3 μs, and the single-threaded in 379 μs, for a ratio of 5.5. While these ratios are not quite at 8, as we would desire, they are still sufficiently close that they do not affect by themselves the performance of the FFT greatly: he difference between the observed multi-threaded performance and the theoretical performance that perfect scaling would imply is of order 35 μs combined, or roughly 4% of the execution time of the optimal FFT. As described below, other cache effects dominate over this, but when this becomes a bottleneck we will again investigate improving it further.

8.3.2 Vectorization of expensive kernels

The C implementation of the correlation and thresholding has also been vectorized to support SSE4.1 and AVX. The vectorization is hand-coded using compiler provided instrinsic functions that map directly onto SIMD instructions, and the loops are unrolled to permit the vectorized kernel to operate on an entire cache line. Wherever possible memory loads and stores are performed with the "aligned" memory intrinsics, and the arrays on which these kernels act are allocated with 32-byte aligned memory, as they are for the FFT call. Much as for parallelization, for the fused threshold-and-cluster kernel, an efficient vectorization is only possible because of the algorithmic change summarized in Sec. 8.2.

As a first estimate of the quality of vectorization, we can benchmark this kernel in isolation and see how many of their instructions are indeed packed AVX instructions; for threshold, this was 99.6%, and for correlate, 100%. Thus the compiler is indeed generating exclusively AVX instructions as we have directed it to via the intrinsic functions. We can quantify the quality of the vectorization similarly to our quantification of the parallelization: benchmarking the kernel with it on and off. In our case it is relatively straightforward to disable most of the vectorization; though it has been hand-coded with vector intrinsics, these are always wrapped in preprocessor directives to allow a graceful fall-back to straight C-code. Hence the intrinsics can be commented out and compiler flags given to prevent the compiler from generating

most such instructions on its own[1]. This comparison has been made for both the correlation and thresholding and clustering kernels, where the ratios are 1.83 and 2.34, respectively.

At first sight these ratios appear quite poor, since for the Sandy Bridge AVX instruction set, the peak theoretical speedup from vectorization is a factor of sixteen for single precision code. That factor comes from a factor of eight for the SIMD single-precision vector width and another factor of two because the core can generate a multiply and an add at each clock cycle. Of course, achieving this peak theoretical speedup is often difficult in practice: the latencies of the multiply and add instructions are five and three clock cycles, respectively, and there are only sixteen SIMD registers that can serve as operands for these instructions. Thus only very specific problems will have the necessary data independence and structure to allow retiring 16 single-precision SIMD arithmetic operations per clock cycle.

Our kernels do not have such structure. The correlate kernel is simpler to analyze, since it is almost identical to element-by-element complex multiplication, for which AVX optimized code is widely available (including from Intel). The only difference between our code and these is that we must add a single instruction, to complex conjugate one of the input vectors. A standard single-precision complex multiplication requires six floating point operations (four multiplications and two additions); an AVX register can hold four single precision complex numbers. Thus the relevant speedup would be how many clock cycles are required to execute the AVX multiplication of the 24 floating point operations equivalent to the multiplication of four complex numbers simultaneously. Because of the need to conjugate an operand as well as the shuffle operations inherent to complex multiplication, there are seven instructions needed for this calculation (there are six in the widely available libraries for AVX complex multiplication; our modification to calculate the complex conjugate adds only a single instruction with a latency of one clock cycle), giving a theoretical speedup of a factor of $2 \times (24/7) = 6.86$, if we were in fact able to retire two AVX instructions per clock cycle. The analysis of the thresholding and clustering algorithm is similar if more complex; each execution of the inner loop requires eight AVX instructions to find

[1]It is not possible to prevent *all* SIMD instructions; because the operating system is 64-bit, the C-library is compiled with a minimal set of SSE instructions, so that turning off all SIMD instructions generates linking errors.

the location and values of the maximum of four consecutive complex numbers, which corresponds to 16 scalar floating point operations if we include the comparison. Thus the maximum speedup is only a factor of four, at most.

The further gap between the theoretical peak speedup of vectorization and our measurement can be attributed to memory bandwidth. The correlation kernel reads in two single precision complex numbers—equivalent to four single precision floating point numbers—and writes out a third; between these memory operations, it performs six floating point computations (four multiplies and two adds). There is therefore a one-to-one ratio of memory operations to floating point operations. For the threshold and cluster kernel, two floats are read, and three floating point operations performed, for a floating point to memory ratio of 1.5. The low floating point to memory ratios mean that any kernel implementing them will be memory bandwidth bound.

We can compare the execution times of these kernels to what memory bandwidth-limited kernels could perform. A correlation for a 2^{20} FFT length must read two vectors of half that length (because the second half is always zero, as part of the FINDCHIRP algorithm to maximize over unknown inspiral phase) and write out a third vector of half that length; a total of 12 MB of memory transactions must occur. If all of that memory lived in the computer's RAM, then we can measure its bandwidth using the STREAM benchmark [159]; for a single socket this bandwidth is approximately[2] 26 GB/s. For correlation, this would imply an execution time of 460 μs, much higher than what is measured, and 307 μs for thresholding, again much higher than observed.

That is unsurprising, since we want the data for those calculations to remain in cache and the benchmark performance numbers for those kernels reflect a repeated execution from within cache. Our kernels are parallelized with the goal that each "chunk" remains in L2 cache, which has a published latency of 12 cycles [160]. However since our memory for each kernel is accessed sequentially we expect that hardware prefetching ensures that the next data to be read is almost always in the L1D cache, which has a *load* latency of typically five cycles, though it can be as high as seven

[2]It is possible to improve this by roughly a third by forcing the use of *streaming stores*; however, while this significantly improves the bandwidth as measured by STREAM, it does so by bypassing the cache on writes. Since the only kernel with significant writes is correlation, this is not beneficial: the output of the correlation *needs* to remain in cache if possible since it will immediately become the input to the FFT.

cycles for AVX loads. For an eight-core E5-2670, which can load or store up to 32 bytes per core, these latencies and the 2.6 GHz clock speed imply an effective load bandwidth of 95 to 133 GB/s. The 87 μs execution of the correlate kernel (which must move 12 MB of memory) would correspond to a bandwidth of 138 GB/s, and the 69 μs execution of the threshold and cluster kernel (which reads 8 MB of memory) would give a bandwidth of 116 GB/s. The correlate kernel slightly outperforms this because its memory accesses are not purely loads. Thus, we conclude that these kernels are bandwidth limited, but achieve essentially the peak bandwidth feasible.

For the two kernels that we have vectorized and parallelized, we find that the parallelization is reasonably good but the performance of vectorization much lower than one might expect. However, this is directly attributable to bandwidth limitation of the kernels, which do achieve close to fthe peak bandwidth for the architecture.

8.3.3 Performance relative to theoretical peak

We have designed our overall algorithm to be dominated by the FFT, and the optimal FFT implementation to be the multi-threaded FFTW library. Our benchmark above gave approximately 960 μs as the execution time of a 2^{20} single-precision, out-of-place complex inverse FFT; if we use $5N \log N$ as the number of floating point operations performed by the FFT, then this corresponds to a performance of 95 GFlops. For comparison, we also measure the floating point operations using the Linux `perf-stat` tool. That measurement indicated first that 99.999% of the instructions retired were single-precision AVX instructions, so the FFTW library code is extremely well vectorized. The corresponding performance was 91 GFlops, or 83% of the $5N \log N$ estimate. Since there are FFT algorithms with a floating point count as low $4N \log N$, this is consistent with the library having chosen an FFT algorithm with lower floating point cost. With eight AVX capable cores that can retire as many as two AVX instructions per clock cycle, the E5-2670 has a peak theoretical floating-point rate of 333 GFlops; we therefore achieve 27% of the peak flop rate. For an algorithm with the complex memory access pattern of the FFT, this is a not unreasonable performance. Regardless, since we expect to be FFT limited we should not expect higher performance from the `pycbc_inspiral` executable as a whole than this.

The performance of `pycbc_inspiral` depends on the quality of the data. Throughout our benchmarking studies we have consistently followed three different types of

data: (i) data which is nearly Gaussian and stationary, representing very good data quality (Type A); (ii) data containing a single, loud transient glitch (Type B), and (iii) data which contains elevated levels of non-Gaussian noise at low frequencies (Type C). The last category is the worst in terms of computational cost, as the χ^2 test must be invoked frequently and the cost is dominated by the computation of that signal-based veto. In late initial LIGO science runs this level of data quality was extremely rare, and should the first observing runs of Advanced LIGO behave similarly, it is not expected to greatly impact the computational cost. The costs we have presented, however, are conservative, and simply average the throughput of the three categories of data.

Measurement of the floating point performance of `pycbc_inspiral` showed 31 GFlops for Type C data, 41 GFlops for loud data, and 44 GFlops for Type A (clean) data. These correspond to fractions of peak theoretical performance of 9.3%, 12.2%, and 13.3%. We therefore still have room for improvement, and discuss in the next section profiling results and their implications that identify the next priorities for further optimization.

8.3.4 Comparison of measured numbers with theoretical FFT throughput

Finally we assess the overall performance of `pycbc_inspiral` through profiling. Continuing with the same three categories of data, we present a profile run of `pycbc_inspiral` in Table 5 for Type A and Type C data, to illustrate the two extremes, for each kernel costing more than 1% of the overall runtime. From this table, the largest difference we observe is that the χ^2 veto is only 4.2% of the execution time in the Type A data, but 44.7% of the time in the Type C data. This is the reason Type C data is so problematic: in this example χ^2 is calculated four times as often as it was for Type A data. Hence more thorough vectorization and parallelization of this kernel is our next optimization priority.

Since our goal is for the `pycbc_inspiral` engine to be FFT limited, we also use the profile information above to measure the average execution time per FFT *in situ* and compare that to the benchmarked performance for our optimal FFT configurations. We present this in Table 6. From these results we see that for the 2048 Hz sample rate, the effective execution time of 516 μs is 84 μs longer than benchmarked average FFT time of 432 μs, whereas for the 4096 Hz sample rate the observed FFT time of

Kernel	**Type A Data**		**Type C Data**	
	Absolute time (s)	Percentage	Absolute time (s)	Percentage
FFT	1304	60.4	1159	32.3
correlate	332	13.9	300	8.4
template creation	203	9.4	202	5.6
threshold & cluster	97	4.5	87	2.4
χ^2	90	4.2	1601	44.7
data resampling	35	1.6	–	<1
recording triggers	–	<1	49	1.4
Total runtime	2158	100	3583	100

Table 5: Profiling results for clean and poor data at a 4096 Hz sample rate on an E5-2670.

Sample Rate	**Type A Data**	**Type B Data**	**Type C data**	**Average**
2048 Hz	517	518	512	516
4096 Hz	1520	1530	1350	1470

Table 6: Effective execution time (μs) of FFT within `pycbc_inspiral` on E5-2670 socket (FFTW, eight-threaded).

1470 μs is 370 μs greater than that obtained by benchmarking the FFT in isolation. We can understand this if we recall that the last-level (level 3) cache of the E5-2670 is 20 MB. While the memory of an out-of-place 2^{20} FFT fits inside this at 16 MB, the total memory required for our matched-filter inner loop of correlation, FFT, and threshold and clustering requires a total of 24 MB and does not fit in cache. Because the different areas of memory comprising this 24 MB are accessed at widely separated (in time) parts of this loop, hardware prefetching is unlikely to be able to hide much of this latency. We can validate this explanation by referring to the 2048 Hz sample rate results, where the total memory required by all of the kernels in the matched filter is 12 MB which does fit in cache. And indeed we see that the *in situ* execution time of that FFT is much closer to the isolated benchmark. As a further check, we have counted the number of last-level cache misses of each sample rate, when analyzing the same data with the same bank and number of segments. The 4096 Hz sample rate analysis incurs between 11 and 15 times (depending on data quality) as many cache misses as the 2048 Hz analysis, even though both performed exactly the same number of matched filters.

We are investigating ways to alleviate this penalty, and discuss some of these in

the next section on future optimizations. Alternatively, it is not yet decided on what hardware the various PyCBC searches will run, and should they do so on hardware with sufficiently large cache the issue could be moot.

Future CPU optimizations

We are investigating a number of performance optimizations to more efficiently implement the existing computational methods: vectorization and parallelization of the template generation and χ^2 veto, and bypassing the CPU cache for loads of some memory, to mitigate the cache eviction causing the degraded *in situ* performance of the 2^{20} size FFT. The latter are in principle possible using the streaming load operations that became available in SSE 4.1, but also require the memory from which they read to be marked as uncacheable, speculative write-combining (USWC) which is only possible through a kernel module. Aside from these implementation optimizations, we are also exploring alternative scientific methods (such as hierarchical searches and pruned FFTs) that if verified through simulations do not degrade sensitivity can provide potentially large computational savings.

8.4 PyCBC on Graphics Processing Units

New compute architectures such as GPUs have recently become widely available and supported for an increasing array of computing tasks. They are specialized for the high throughput of vector operations, which maps well to the operations of a matched-filtering algorithm, and offers the possiblity of a dramatic increase in overall performance for a matched-filtering based gravitational-wave search. Our goal when implementing the GPU-enabled version of PYCBC_INSPIRAL is to execute as much computation on the GPU, with as little data passing over the (slow) PCIe host interconnect as possible. Simply off-loading the FFT to the GPU does not significantly speed up the code, due to the rate-limiting step of moving the input and output vectors over the PCIe bus. Fortunately, the FINDCHIRP algorithm lends itself well to performing all computations on the GPU, as the pre-conditioned input data segments can be stored in global GPU memory and then processed through many templates that are generated on the GPU. Our GPU implementation therefore implements as CUDA-native kernels *both* the compute-intensive steps of the algorithm

(correlate, FFT, and time-frequency signal-based veto) *and* the relatively light-weight steps (template generation and threshold/cluster), ensuring that only very minimal PCIe bandwidth is required to initially stage the data to GPU memory and pass triggers back to host memory.

For large regions of parameter space, template generation can be expressed as an analytic polynomial, which we have implemented as a straightforward element-wise GPU kernel. Work is ongoing on extending template generation to other waveform approximants that are more appropriate for modeling higher mass BBH systems. As the correlate kernel is a point-wise complex multiply and conjugate, the GPU implementation is also straightforward. We make use of NVIDIA's proprietary cuFFT library to perform inverse FFTs. This library factors the FFT into multiple kernel calls based on the size of the FFT and the GPU hardware capability. On a Tesla K10, using CUDA 6.5, FFT sizes between 2^{20} and 2^{23} all factor into three kernels calls. As the FFT is memory bandwidth bound, it is clear that for these range of sizes the FFT throughput will scale linearly with vector length. Thresholding and clustering is divided into two kernels. The first performs both thresholding and local peak finding on small fixed window sizes. The kernel window sizes are smaller than the scientifically chosen clustering window. This exposes an additional parallelism. A second, very short-running kernel that executes a single block, is used to perform final cleanup and boundary condition checking. Following this kernel, we dump triggers back to the host, which due to the on-GPU clustering is guaranteed to be $O(10^{-3})$ the size of the data vectors in the worst case, and on average much less. Finally, we have also implemented our time-frequency signal consistency test as a set of GPU kernels where each is designed to handle a different number of triggers. This is implemented using a standard parallel reduction sum operation.

8.4.1 Optimization of the GPU Implementation

Similar to the CPU implementation, the 3 kernels that dominate the inner loop of the matched-filter (correlate, FFT, and thresholding) are all memory bandwidth bound. Therefore both memory bandwidth and floating point performance are considerations when selecting the optimal GPU hardware.

While our initial CUDA implementation of the the FINDCHIRP algorithm is efficient in the sense that as much computation is performed on the GPU as possible, we

have identified several areas for future optimization. Several of these optimizations are in progress, but others require assistance from the NVIDIA CUDA and cuFFT engineers as they require re-design of the cuFFT API.

Since all of our input data is staged to the GPU, the rate limiting factor for our current implementation is the memory bandwidth between the GPU's global memory and the on-chip Level 2 cache and registers where threads access data for computation. Our primary goal in optimizing the GPU implementation has been to reduce the number of memory transfers and maximize the use of the GPU's floating point engine. CUDA kernels operate on data in GPU global memory and for each kernel call, data is transferred across the memory bus[3] from GPU global memory to the registers of the processor cores and back to global memory at the end of the kernel. A basic performance analysis can be obtained by counting the memory operations executed by the correlate, FFT, and threshold kernels used in the FINDCHIRP loop:

$$\text{Correlate(2in+1out)+FFT(3in+3out)+threshold(1in)} = 10\,\text{memory transfers} \quad (8.1)$$

With the release of CUDA 6.5, a new feature was added to the cuFFT library that allows user defined callback functions for both the load of the initial input vector and the store of the final output vector of the FFT. This has the potential of allowing us to fuse computations from the correlate and threshold steps into the FFT kernel, reducing the number of memory transfers and increasing performance. Our first step towards optimizing our CUDA implementation has been to investigate the use of callbacks.

The current implementation of NVIDIA's cuFFT callback API allows element-by-element functions to be easily applied, with no guarantee about the relationship between nearby elements or order of operations within the kernel itself. Because the callbacks cannot be compiled into the FFT kernels themselves, and can handle only single elements, there is significant overhead to their use that cannot be easily predicted without benchmarking. Fig. 48 compares the relative execution time of the three kernels that make up the inner loop of the matched-filter code under three cases. The first case (left) uses the initial kernel implementations without making use of the callback API. The second case (middle) fuses the correlate kernel, without

[3]Typically DDR3 or GDDR5 depending on the model of GPU card.

modification, into a load callback. We see that there is a noticeable drop in the total execution time. The savings comes from the removal of both a full vector length store and read operation. Note however, that this is significantly less improvement than would expected from a naive counting of the memory savings. The final case takes full advantage of the known contiguous regions where the input vectors are zero, and where the output vector does not produce valid results due to wrap-around corruption. Callbacks appear to be a very promising avenue of optimization, and our collaborators on the NVIDIA cuFFT team are interested in our application as a use-case for developing the API further.

For certain kinds of commonly used waveform templates, in particular the TaylorF2 approximant, the amplitude of the waveform is a simple power series. This allows it to be precomputed, and instead of including it with the template itself can be pre-multiplied into the segment of data to analyze. Where this is possible, the remaining portion of the template can be expressed in the form $e^{i\psi(f)}$. It is possible to trade floating point operations for a savings in global memory reads by storing only the Fourier phase of the template, $\psi(f)$, and recalculating the full $e^{i\psi(f)}$ within a load callback of the FFT. If the callback API can be extended to allow a vectorized version of the store callback that operates on contiguous elements, it may be possible to merge a portion of the peak finding algorithm into the store callback, vastly decreasing the memory writes at the end of the fused kernel.

More optimal use of the available memory bandwidth can also be achieved by reducing the amount of data sent over the memory bus. We are investigating the possibility of storing the output SNR time and input template phase as half-precision (FP16) numbers to reduce memory bandwidth. We have also discussed with NVIDIA the possibility of adding callbacks to the intermediate steps of the cuFFT implementation (since our 2^{20} point FFTs are implemented by three kernel calls in cuFFT) that would allow us to use FP16 precision between each FFT radix. Performing the FFT operations in FP32 and storing the intermediate products in FP16 may be possible. We are beginning a study to determine if this model could meet our accuracy requirements.

Finally, we are investigating the optimal GPU/CPU ratio for systems and parellization between the host CPU and GPU kernel execution. As GPU kernel launches

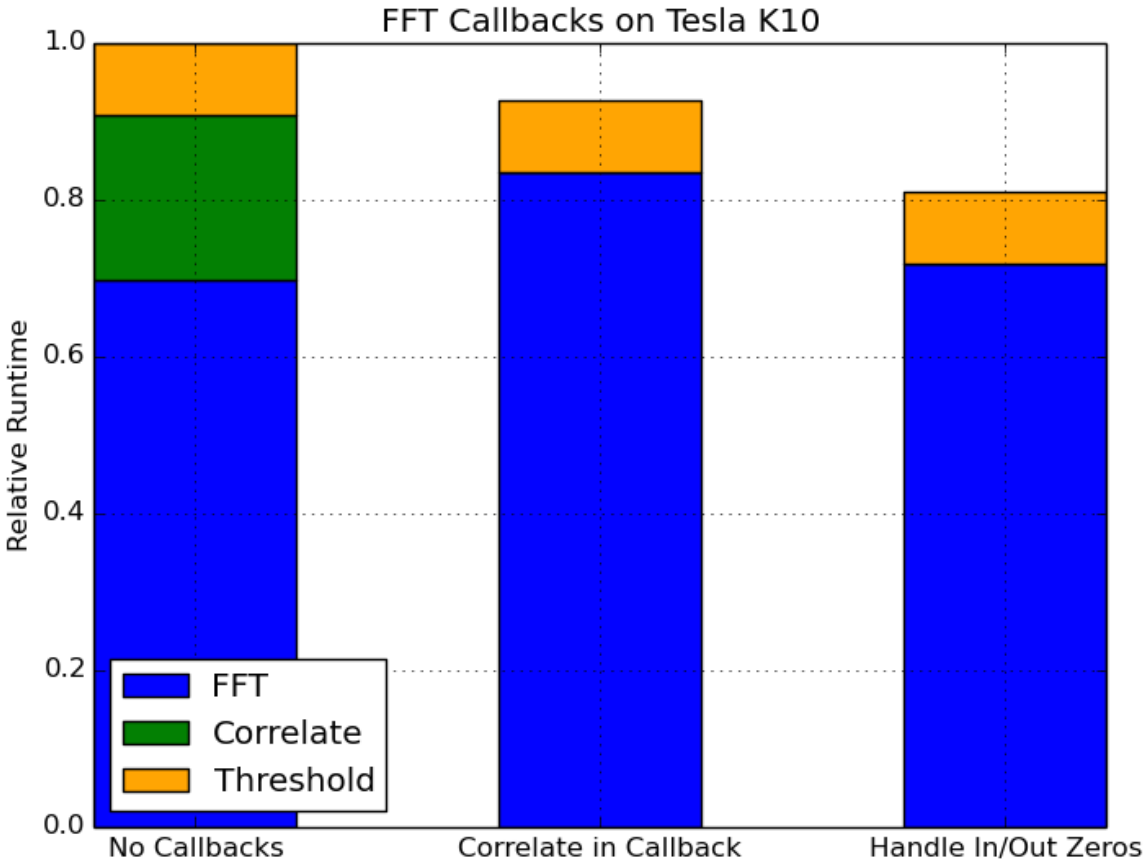

Figure 48: The relative performance of the kernels that make up the critical inner matched-filtering code. Shorter bars represent better performance. Left: The initial GPU kernel implementations without the use of cuFFT callbacks. Middle: Naive fusion of the correlate into a load callback. Right: Fusion of the correlate kernel into the load callback, where memory reads are avoided where the input is known to be zeros, and output writes are avoided where it is known to be corrupted by wrap-around effects. It is not currently possible to fuse the threshold kernel into the FFT, however we are working with NVIDIA to make the necessary changes to the cuFFT callback API to further optimize the code.

are asynchronous compared to host execution, it is possible to hide trivial serial operations that occur within the host code. The exception is where triggers are offloaded from the GPU onto the CPU, which is a blocking operation. Host execution does not proceed until the GPU queue is drained. When the data is synchronized there is a noticeable delay before new GPU kernels are executing. This can be minimized by executing multiple host processes that submit work to the same GPU, and by batching additional work together to amortize the device offload latency. We have shown that two processes running on the same CPU launching kernels to a single GPU makes more efficient use of the GPU resources; tests to find the optimal ratio are ongoing.

Chapter 9

Focused Search for Binary Neutron Stars

9.1 Introduction

We present an offline search pipeline tuned for the detection of gravitational-waves from binary neutron start sources, and show that this targeted search yields significant improvements in sensitivity to BNS sources. Whereas in prior searches for BNS systems, such as the last one conducted in S6/VSR2,3, a non-spinning template bank was constructed that contained masses up to $25M_{\odot}$ [15] and was tuned to maximize the overall sensitivity, in this work we focus solely on BNS systems with a mass range from $1 - 3M_{\odot}$. We consider two banks of templates, a *non-spinning template bank* designed to be sensitive to mergers where the components have neglible intrinsic angular moment, and an *aligned spin template bank* which is designed to be sensitive to BNS mergers where the intrinsic angular momentum of the components can be as large as $\chi = 0.4$. To approximate the conditions of the first observing run with Advanced LIGO, we focus on a two-detector network composed of the Hanford (LHO) and Livingston (LLO) observatories. To assess proposed improvements to the search pipeline we test the search on three weeks of LIGO data from S6.

This chapter is organized as follows. In Sec. 9.2 we describe the methodology of the search pipeline, and we present a method for estimating the significance of candidate events. In Sec. 9.3, starting with the configuration suggested in Ch. 7, which improved upon the S6/VSR2,3 by requiring exact-match coincidence, we present a procedure for

further improving the search sensitivity of the pipeline by optimizing key parameters of the search, namely the configuration of the power spectral estimation, the signal-consistency tests, the single detector SNR thresholds, and the lower frequency cutoff.

9.2 Significance of Candidate Events

The focused BNS search pipeline implements the single stage analysis pipeline proposed in Ch. 7. A bank of post-Newtonian TaylorF2 3.5 PN order templates, generated using the metric based placement algorithm proposed in Ch. 4, is created to span the extended binary neutron star mass range from $1 - 3M_{\odot}$. A template bank is generated separately for each of the three S6 analysis weeks, using the harmonic mean of the detector data during that week. Each template is match-filtered against the data to calculate a signal-to-noise time series. Excursions in the SNR time series from each detector are recorded if they exceed a fixed SNR threshold, which was 5.5 in S6/VSR2,3, and it is the loudest within one second. To cope with the large number of transient non-Gaussian events, we apply a signal consistency test, and calculate a reweighted signal-to-noise ratio, defined in Eq. (2.9).

We additionally require that a candidate is seen by both the Hanford and Livingston observatories. In keeping with the findings of Ch. 7 we require that the trigger in each detector be found by the same template, and within the light-travel time between the detectors. A combination of single detector events that passes this test is a *coincident event*, whose combined statistic is given by Eq. (2.10).

In order to claim a candidate signal as the detection of a gravitational-wave, we need to determine the probability that it could have been attributed to noise. We estimate the false-alarm rate by forming coincidences between single detector triggers that are outside of the standard coincident time window. For both computational efficiency and simplicity, we choose to form background coincidences by applying a time shift to one detector. The triggers from one detector are offset by all possible non-zero integer multiples of a fixed interval, T_s, known as the *timeslide interval*. For this analysis, we haven chosen T_s to be 0.2 s. From these time slides, we collect a set of coincident triggers. As this set was formed from all of the original single detector triggers, we will refer to it as the *inclusive background*, B_{inc}. Note, that if there is a loud gravitational-wave signal its component single detector triggers will also form

coincidences with noise triggers from the other detector, and those will be contained in this background set. The inclusive set of background triggers can be expanded as

$$B_{inc} = \{N_H \oplus N_L\} \cup \{N_H \oplus S_L\} \cup \{S_H \oplus N_L\}, \tag{9.1}$$

where $N_{H/L}$ are single detector noise triggers, $S_{H/L}$ are single detector triggers from gravitational-wave signals, and $\{A \oplus B\}$ represents the set of coincidences between the single detector triggers A and B. We can define a set of background triggers that excludes coincidences between signals and noise, B_{exc}, by excising single detector time surrounding each of the foreground coincident triggers, with components F_H and F_L. We refer to the amount of time ignored around each foreground event as the *blinding window*, T_{blind}, which in this case we have chosen to be 100ms. This value is chosen as a balance between the amount of triggers removed and the influence that a gravitational-wave signal may have on the template. This can be expressed as,

$$B_{exc} = B_{inc} - \{S_H \oplus T_L\} - \{R_H \oplus S_L\} - \{S_H \oplus R_L\}, \tag{9.2}$$

where $R_{L/H} \in N_{L/H}$, and the time difference between any element in $R_{L/H}$ and any element of $F_{H/L}$ is greater than the blinding window T_{blind}.

Both backgrounds are valid for different types of questions. The inclusive background admits the possibility that all triggers could be noise generated, including the triggers of a candidate signal. The exclusive background presumes that a given candidate is a signal while testing it against the remainder of the background. Estimating the significance of a candidate by comparing against the inclusive background will result in a more conservative value. This was exemplified during a blind injection challenge performed during the S6/VSR2,3 lowmass CBC search, where a signal was injected into the detectors to test the procedure for validating a candidate gravitational-wave detection. However, it was found that while the candidate had a FAR of 1 per 7000 years, the limiting background coincident events were all made from the signal in one detector and a time-shifted noise trigger in the other. [15].

We use the false-alarm rate as our principle measure of the significance of a candidate event. Given an event wih a $\rho^c_{new} = x$, we can express the false-alarm rate

(FAR), when comparing to both the inclusive and exclusive background sets as

$$FAR(x) = N(x)/T_B, \tag{9.3}$$

where $N(x)$ is the number of coincident events in the estimated background set with a $\rho^c_{new} > x$. A separate FAR is calculated using both the inclusive and exclusive background sets, giving two significance measures, FAR_{inc} and FAR_{exc}. T_B is the effective background time, which can be accurately estimated from the single-detector livetimes T_H and T_L for the Hanford and Livingston detectors, respectively, as

$$T_B = T_H \times T_H/T_s \tag{9.4}$$

Note, that this is not an exact calculation of the background livetime. The exact time can be obtained by explicitly calculating the amount of overlapping time between the Hanford and Livingston gravitational-wave data for each time slide and taking the sum. The estimate is equivelant to the exact calculation in the case that the start and end of every chunck of analyzed data lies on a multiple of the timeslide interval. As such, we can calculate the upper bound on the difference between the true and estimated value of the background livetime as

$$|T_{b,estimate} - T_{b,exact}| < 2 \times N_{chunks} \times T_s, \tag{9.5}$$

where N_{chunks} is the number of non-contiguous analysis chunks. As our analysis discards chunks of data that are less than 2048 seconds in length, and $T_s = 200$ ms, the relative error is strictly less than .02%, and so can safely be considered negligible.

9.3 Optimizing Search Sensitivity

In this section, we retune several parameters of the CBC search, with the aim of creating a search optimized for the detection of binary neutron star mergers. The potential parameter space of tuning choices is quite large, so we have started with the filtering settings used in the lowmass CBC search performed in S6/VSR23, and include the proposed changes from Ch. 7.

In the following sections, we test proposed changes to the analysis pipeline using a

template bank which is designed to have a 97% minimal match with non-spinning BNS signals with component masses between $1-3M_{\odot}$. We evaluate the search performance of a particular set of tuning parameters, by using the sensitive volume of the search integrated over the coincident livetime of each of our three sample weeks of S6 data. The sensitive volume is estimated by simulating a population of sources, inserting them into real detector data, and recovering them using the search pipeline. In this work, we choose the test injection set to consist of non-spinning BNS sources distributed uniformly between $1 - 3M_{\odot}$.

The product of the sensitive volume and the coincident analysis time, VT, can be expressed as,

$$VT(F) = \sum_{w=0}^{2} V(w, F) T_{coinc}(w) \tag{9.6}$$

where V(w, F) is the sensitive volume as given by Eq. (2.13) for a given week, w, of the sample analysis. The total amount of analysis time for a given week is given by $T_{coinc}(w)$. The quanitity VT is directly proportional to the expected number of detected gravitaional-wave signals from the simulated population.

9.3.1 Power Spectrum Estimation

Because the overall sensitivity of a detector, along with the shape of its power spectral density (PSD) changes over time, the spectral density used to calculated the matched-filtering SNR of candidate events is periodically recalculated. The S6/VSR2,3 analysis recomputed the PSD using every 1920 seconds, an interval known as the *analysis chunk*. However, due to the additional padding required for filtering, 2048s of data was used for each PSD estimate. Every 2048s chunk of data was subdivided into 15 segments, each with 256s duration and overlapped by 50%. The PSD of each analysis chunk is calculated by first taking the median average of the Fourier transform of each segment. Finally, we truncate the inverse of the PSD in the time domain to restrict the filter corruption to a fixed length of time. In addition, this has the effect of smoothing out lines within the spectrum. An inverse truncation value of 16 seconds was used throughout S6/VSR2,3.

We investigate a straightforward improvement to this algorithm. Instead of calculating the PSD using 256 second segments and applying a 16 second inverse spectrum truncation, we propose calculating the PSD using 16 second segments directly, interpolating for the intended use case, and finally applying the same 16s inverse spectrum truncation. Increasing the number of samples in the PSD estimate decreases the variance, and reduces the influence of outlier estimates, such as those caused by the nearby presence of a glitch. The results of this investigation are shown in figure Fig. 49, where the sensitive volume-time is compared for the initial reference configuration and for the proposed configuration as a function of the inverse false-alarm rate. The proposed PSD estimation shows clear improvement over the method used in S6/VSR2,3, resulting in an average $\approx 12\%$ increase in sensitivity between inverse false-alarm rates of 10^3 and 10^4 years.

9.3.2 Signal-to-noise Threshold

For each detector, triggers are recorded when the signal-to-noise ratio exceeds a predetermined threshold, ρ_t. For the S6/VSR2,3 CBC search, only triggers with an SNR above 5.5 were recorded. Beginning with the PSD tunings proposed in Sec. 9.3.1, we investigate the effect of lowering the SNR threshold to 5.0. A comparison of the search sensitivity at $\rho_t = 5.5$ and $\rho_t = 5.0$ is shown in Fig. 50. We see that lowering ρ_t from 5.5 to 5.0 has not resulted in a significant improvement in sensitivity. We observe that at high inverse false-alarm rate, the inclusive IFAR is identical between the two thresholds, but that there is a very minor increase in sensitivity when using the exclusive IFAR.

In Fig. 51 we explore where the differences between the inclusive and exclusive IFAR estimates are the greatest. At a fixed exclusive IFAR, which monotonically increases with the combined weighted SNR of an injection trigger, we find that there is an inverse relation between the inclusive IFAR and the minimum single detector SNR. This indicates that lowering the SNR threshold below ≈ 5.3 will not yield an improvement in sensitivity at inclusive false-alarm rate of 1 in 1000 years, for a two-detector search composed of the Hanford and Livingston LIGO observatories. Note that this result cannot be generalized to a multi-detector network, where there can be a non-trivial increase in detection confidence due to the presence of quiet trigger in the additional detectors. Further work is required to characterize the appropriate

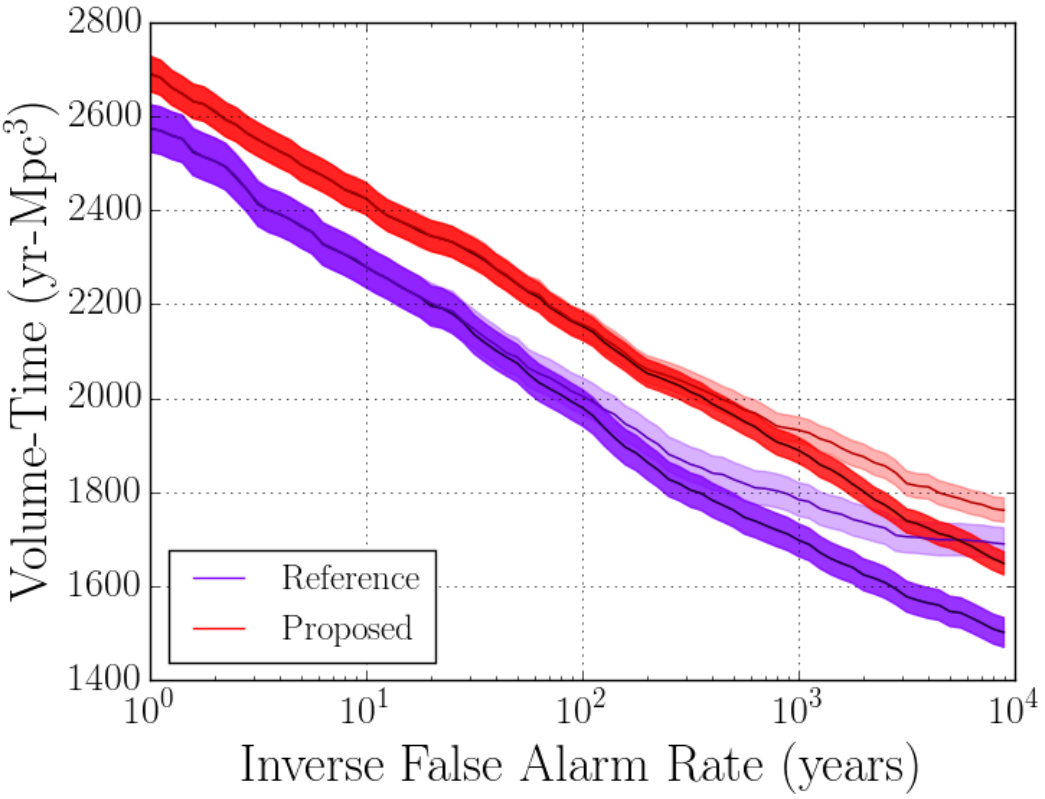

Figure 49: The combined VT as a function of inverse false-alarm rate, for the combined three weeks of analysis, and for an injection population that uniformly covers the parameter space of the non-spinning BNS region, with component masses between $1 - 3M_{\odot}$. Darker colored lines indicate the inclusive IFAR value, while lighter lines show the exclusive IFAR. The reference (red) PSD estimation uses 15, 256s segments. The proposed (purple) tuning which uses 252, 16s segments. Both truncate the inverse spectrum in the time domain to 16 seconds. The proposed configuration improves the search sensitivity by $\approx 12\%$ at a false-alarm rate of 1 per 1000 years.

SNR thresholds for multi-detector networks.

9.3.3 Signal-consistency Test and Ranking Statistic

As detailed in Ch. 2, the single-detector ranking statistic is the SNR weighted by a time-frequency signal consistency test. The test breaks a template into p frequency bins of each power. Although the boundaries of the bins are defined in the frequency domain, as the TaylorF2 templates we use in the analysis are a monotonic functions of time and frequency, we can outline the rough time-frequency boundaries of each bin as demonstrated in Fig. 52. We show the 16 bins used in the S6/VSR2,3 analysis. Since the response of the time-frequency chisq is dependent on the morphology of the non-Guassian noise present in the data, we investigate if increasing the number of time-frequency bins for a BNS focused search, where the average template duration is significantly longer than for searches that include higher mass templates, has an effect on the search sensitivity.

Starting with the analysis tunings suggested in Sec. 9.3.2, we compare the search sensitivity at a fixed exclusive FAR of 1 per 1000 years. The results in Fig. 53, show that increasing the number of time-frequency bins from 16 to 64-256 results in an $\approx 12\%$ improvement in search sensitivity. From the results of Fig. 54 we see that this improvement occurs at all values of the FAR. Based on this result, we propose using a value of 128 bins for a BNS analysis, but would suggest re-examining this choice as the effective length of a BNS template increases as detectors such as Advanced LIGO proceed towards design sensitivity.

9.3.4 Lower-frequency cutoff of the matched filter

As we have been using data from the sixth LIGO science run, we expect that seismic noise will dominate at low frequencies, and so have used the same 40Hz lower-frequency cutoff used in the S6 analysis. We can verify that using a 40Hz lower-frequency cutoff does not impact search performance by constructing

$$V(f_{min}) = \left[\frac{\int_{f_{min}} \frac{h^*(f)h(f)}{S_n(f)} df}{\int_0 \frac{h^*(f)h(f)}{S_n(f)} df} \right]^3 \tag{9.7}$$

where $h(f)$ is a template waveform, $S_n(f)$ is the power spectral densitity, and the

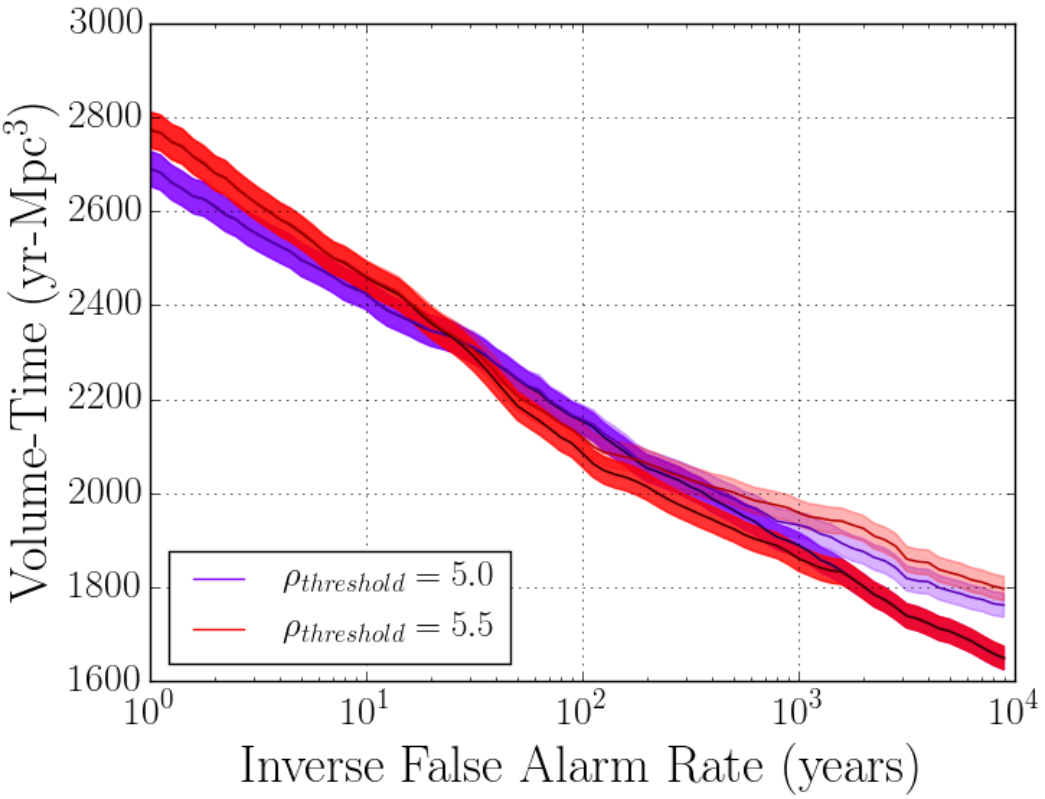

Figure 50: The combined VT as a function of inverse false-alarm rate, for the combined three weeks of analysis, and for an injection population that uniformly covers the parameter space of the non-spinning BNS region, with component masses between $1 - 3M_{\odot}$. Darker shaded lines indicate the inclusive IFAR value, while lighter lines show the exclusive IFAR. We find that dropping the SNR threshold of the analysis from 5.5 (red) to 5.0 (purple) has a negligible effect on the overall search sensitivity.

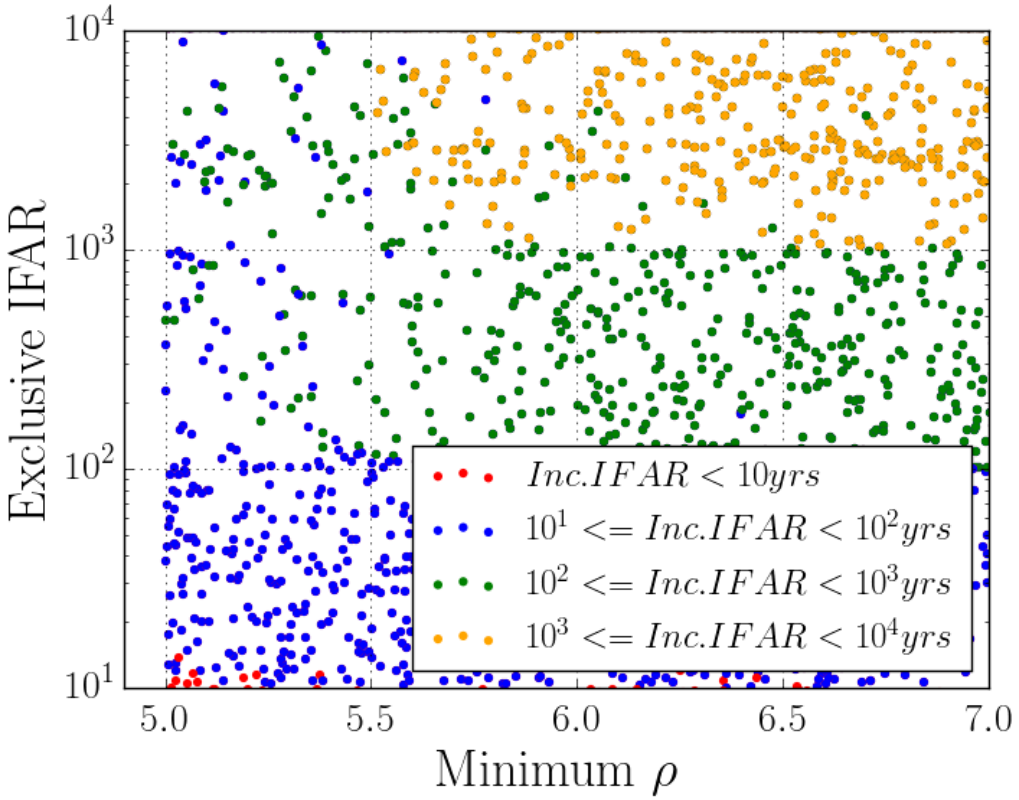

Figure 51: The distribution of exclusive IFAR as a function of the minimum single detector SNR, for an injection population that uniformly covers the parameter space of the non-spinning BNS region, with component masses between $1 - 3M_{\odot}$. Injections are colored by the value of their inclusive IFAR. We observe that there is an inverse relationship between the inclusive IFAR and the minimum SNR value. This indicates that for a given value of inclusive IFAR, there is a corresponding SNR threshold, below which, the search sensitivity as function of inclusive IFAR will not improve

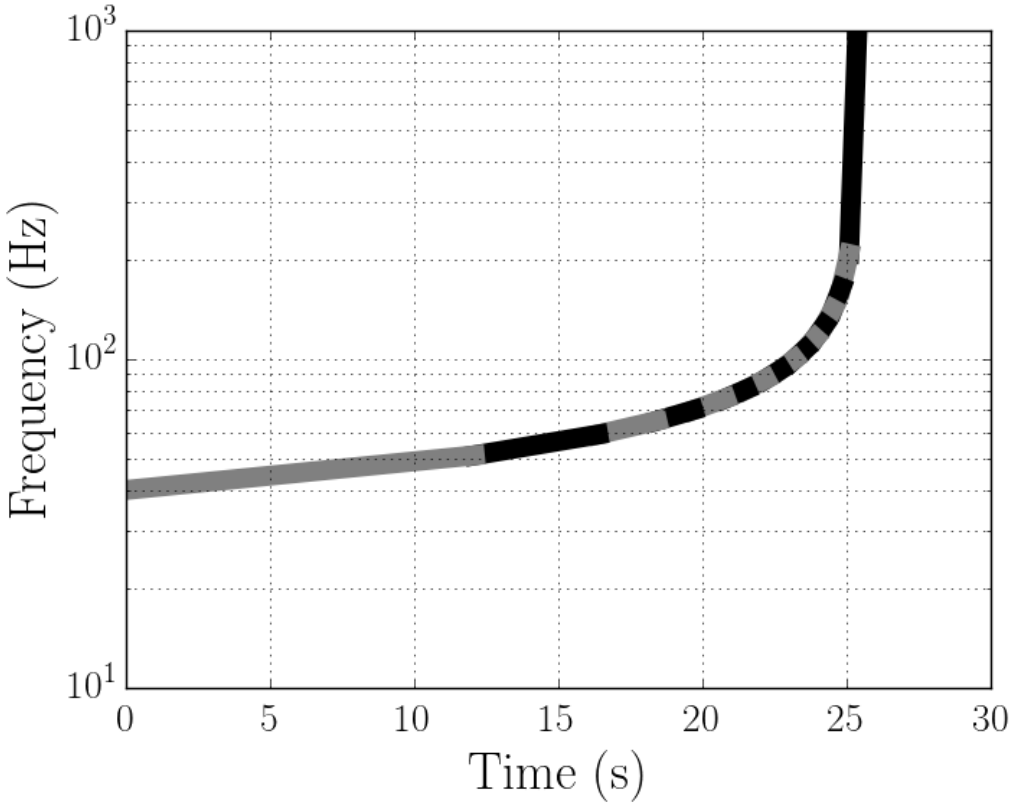

Figure 52: Approximate boundaries of the 16 bins that make up the time-frequency signal consistency test, as used in S6/VSR2,3, overlaid on the track of a $1.4 - 1.4 M_{\odot}$ BNS waveform.

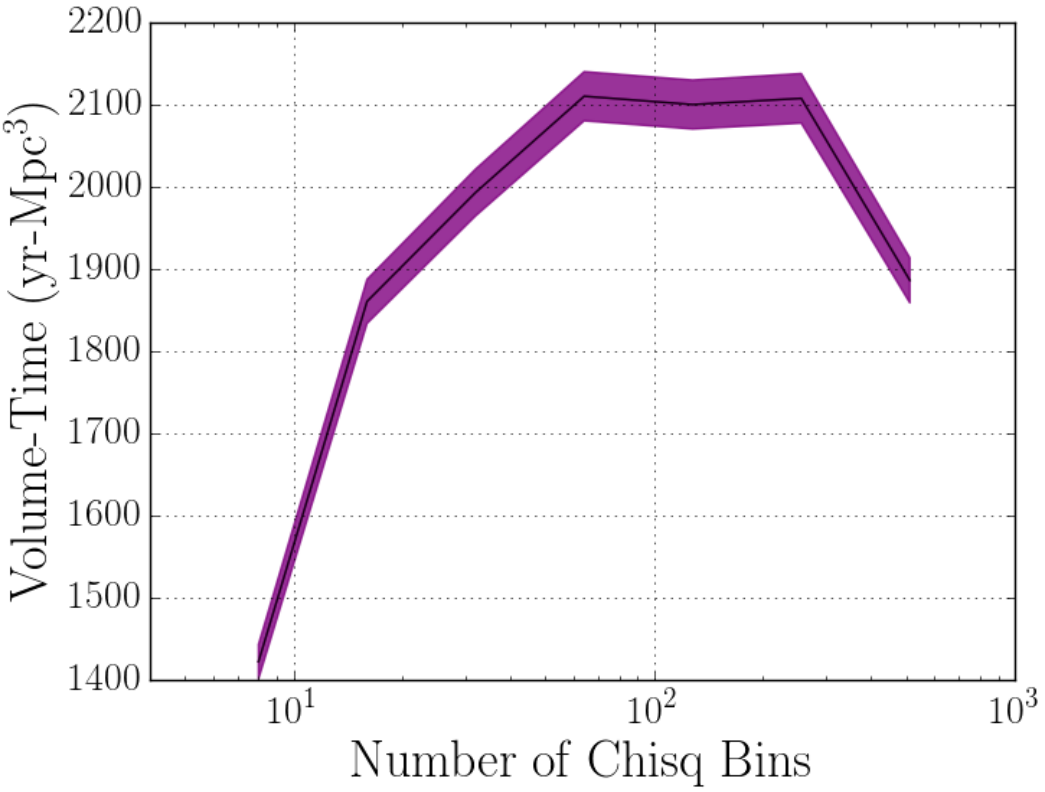

Figure 53: The combined VT at inclusive inverse false-alarm rate of 1/1000 years as a function of the number of time-frequency bins in the signal-consistency test, for the combined three weeks of analysis, and for an injection population that uniformly covers the parameter space of the non-spinning BNS region, with component masses between $1 - 3M_{\odot}$. There is an $\approx 13\%$ improvement in the analysis sensitivity when using 64-256 bins, as compared to the reference 16 bins.

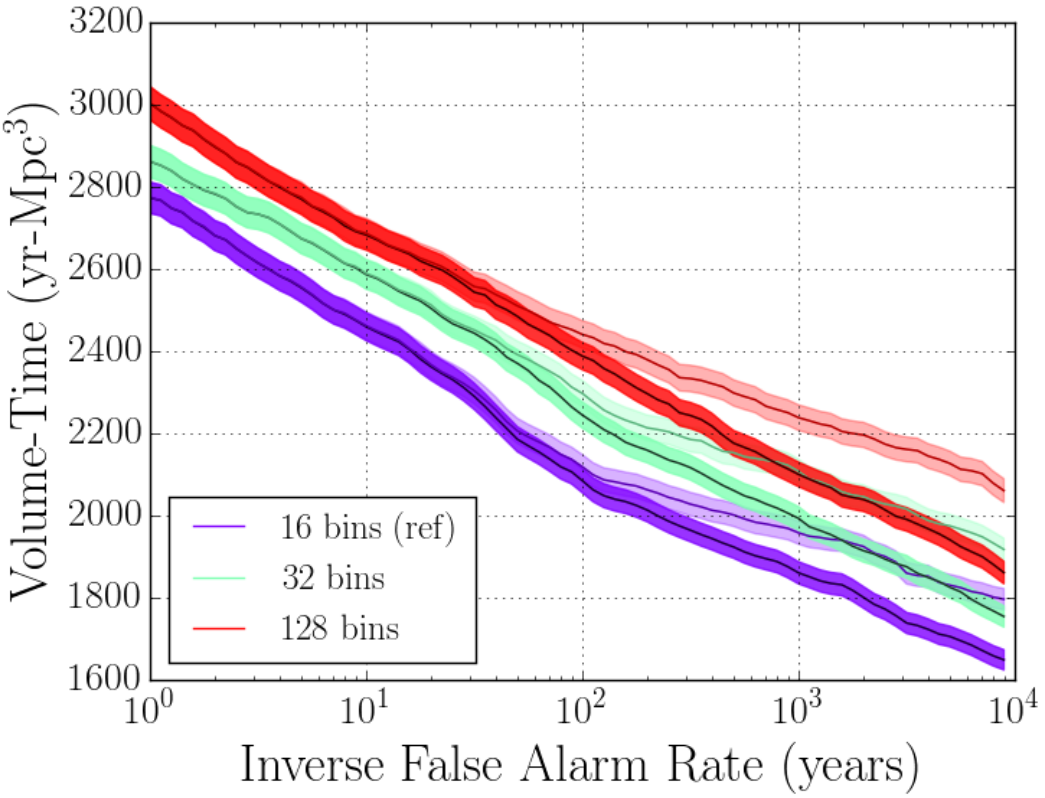

Figure 54: The combined VT as a function of inverse false-alarm rate, for the combined three weeks of analysis, and for an injection population that uniformly covers the parameter space of the non-spinning BNS region, with component masses between $1 - 3M_{\odot}$. Darker colored lines indicate the inclusive IFAR value, while lighter lines show the exclusive IFAR.

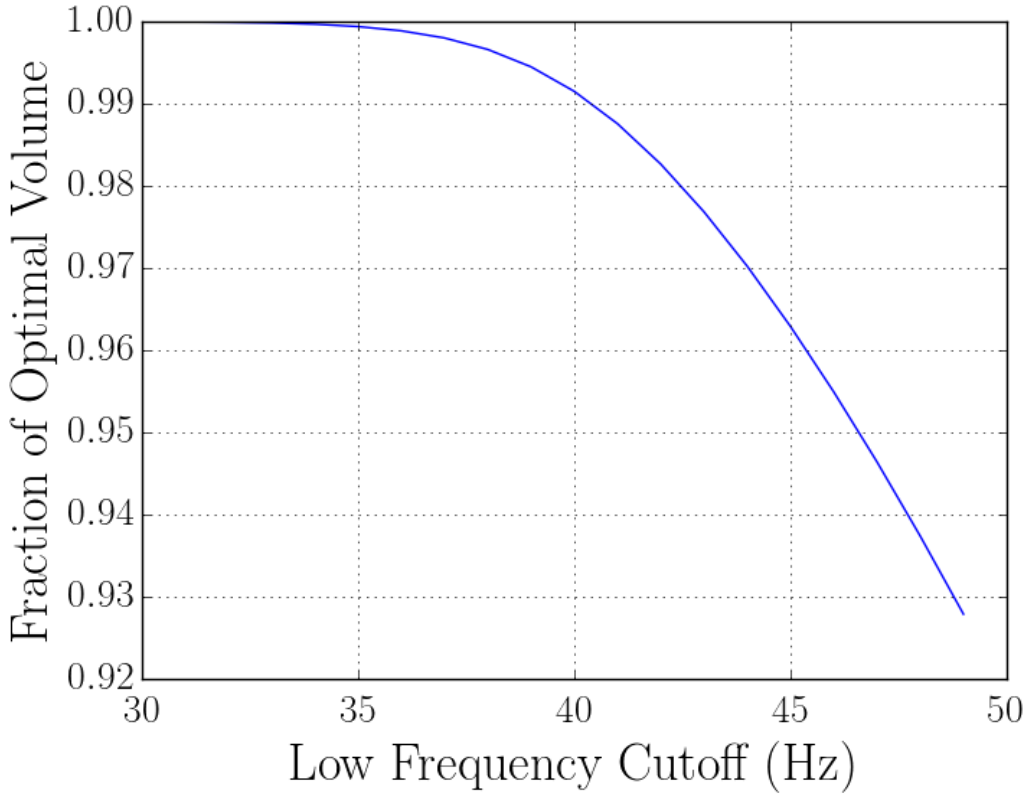

Figure 55: The fraction of the optimal search volume for a $1.4 - 1.4 M_{\odot}$ TaylorF2 BNS waveform, as a function of the lower-frequency cutoff of the matched filter.

quantity $V(f_{min})$ represents the fraction of the optimal volume for a single template filtered from the lower-frequency cutoff, f_{min}. Fig. 55 shows that filtering from 40Hz only results in only a 1% loss in search volume, for a single 1.4-1.4$M_{\odot}$ TaylorF2 template, and so it is an appropriate choice for this data.

9.4 Sensitivity to Astrophysical Sources

In the following sections we compare the sensitivity of tuned BNS analysis we find from Sec. 9.3.3 to the original filter settings used in Ch. 7, and which mimic those used in the S6/VSR2,3 analysis. We consider two choices banks of templates, a *nonspin* template bank designed to be sensitive to mergers where the components have neglible intrinsic angular moment, and an *aligned* template bank which is designed to be sensitive to BNS mergers where the intrinsic angular momentum of the components

can be as large as $\chi = 0.4$, and is aligned with the binary's orbital angular momentum.

9.4.1 Broad distribution of non-spinning sources

In this section we test the sensitivity of the BNS analysis to broad mass distribution $(1 - 3M_{\odot})$ of sources where the component neutron stars are non-spinning. The parameter space corresponds to the intended coverage of the non-spinning template bank we have tuned against in Sec.9.3. In Fig. 56 we show the reference and tuned pipeline configuration using both the aligned spin and nonspin template banks. We see that for either template bank there is a 25% increase in search volume using the improved pipeline tunings. Both template banks use the same geometric placement algorithm and required minimal match, and since the injection set is strictly within the boundaries of both template banks, the loss of $\approx 6\%$ loss in search volume when using the aligned spin template bank is due to the increase in background associated with the $\approx 10x$ increase in template bank size.

9.4.2 Broad distribution of aligned-spin sources

In this section we choose a distribution of sources drawn uniformly from the parameter space that the aligned spin template bank is intended to cover, where each components' mass is between 1 and 3 $M_{\odot}$ and the spin magnitude is uniformly distributed between χ =0 and 0.4. The intrinsic spin of each neutron star is restricted to aligned to the orbital angular momentum. One would expected this distribution to be more favorable to the aligned spin template bank than the non-spinning one. We find in Fig. 57 that the aligned spin template only provides a marginal $\approx 2\%$ improvement in search volume, which we note is close to the measured statistical error.

9.4.3 Broad distribution of precessing Sources

In contrast to the distribution of injections used in Sec. 9.4.2, we do not expect that coalescing systems will preferentially contain binary neutron stars whose spin is aligned with the orbital angular momentum. In this section, we test the same population of sources, but where the spin angles are isotropically distributed. This will allow the systems to precess, however, as the mass ratio of a BNS systems and the magnitude of the spin is small, the effect of precession is not significant. Although the

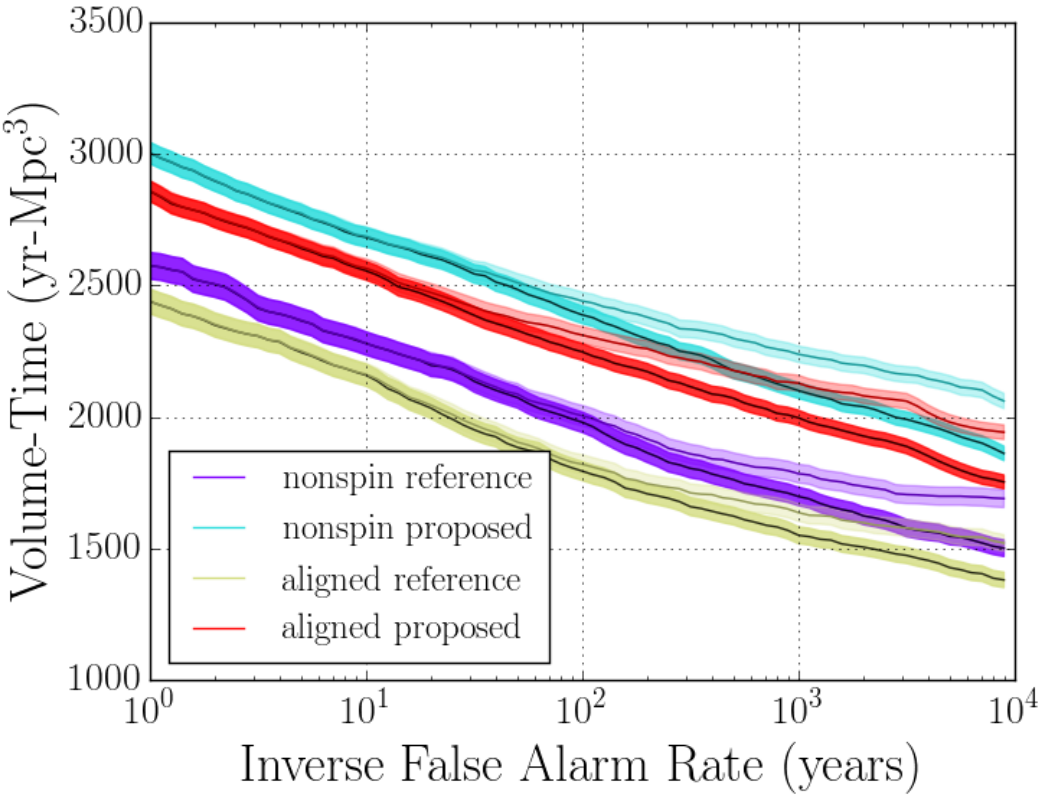

Figure 56: The combined VT as a function of inverse false-alarm rate, for the three sample analysis weeks, for an injection population that uniformly covers parameter space of the non-spinning BNS region, $1 - 3M_{\odot}$. Darker shaded lines indicate the inclusive IFAR value, while lighter lines show the exclusive IFAR. For both the non-spinning template bank and the aligned spin template bank there is $\approx 25\%$ improvement in search sensitivity.

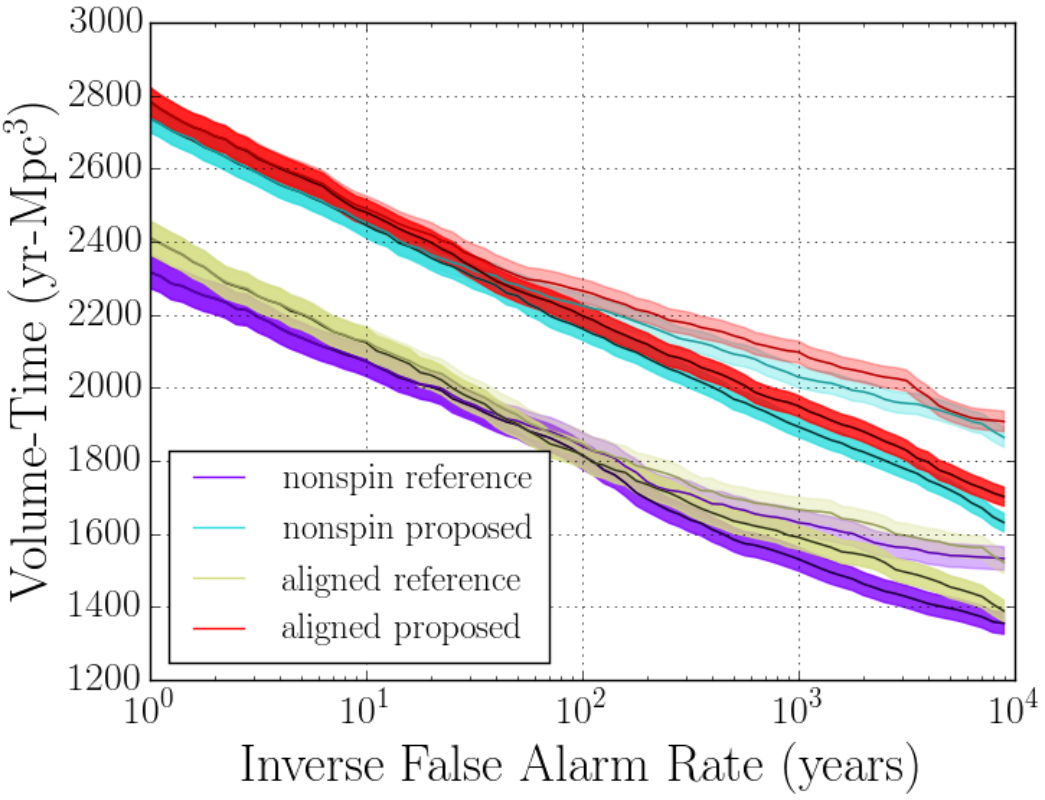

Figure 57: The combined VT as a function of inverse false-alarm rate, for the three sample analysis weeks, for an injection population that uniformly covers parameter space of the aligned spinning BNS region, $1 - 3M_{\odot}$, and $|\chi| <= 0.4$. Darker shaded lines indicate the inclusive IFAR value, while lighter lines show the exclusive IFAR. At a false-alarm rate of 1 per 1000 years, the aligned spin template bank improves the overall search sensitivity by only $\approx 2\%$

injection population covers the full range of spin magnitudes, which the aligned spin template bank is designed to recover, the nonspinning template bank is marginally more sensitive. Fig. 58 shows there is an $\approx 1.5\%$ increase in search volume. A source population that is highly weighted towards highly spinning systems would be required for the aligned spin template to substantially improve the search sensitivity over the nonspinning template bank.

9.4.4 Astrophysically-motivated Conservative Source Distribution

We test the focused BNS analysis against an estimate of astrophysical sources using an injection population drawn from a conservative range of mass and spin distributions. Based on the population of observed BNS sources, as noted in Sec. 3.1, we draw injections from a population with a Gaussian distribution of component masses centered on $1.40 M_{\odot}$, and a standard deviation of 0.13. The intrinsic spin of each neutron star is chosen from a uniform distribution of spin magnitudes $|\chi| < 0.05$, and an isotropic distribution of spin angles.

We clearly see in Fig. 59 that a search using only a non-spinning template bank yields a $\approx 7\%$ improvement in search sensitivity over one that covers an expansive spin range. If the true distribution of signals matches the expectations from current observations, then a non-spinning template bank is the preferred option. Note, that future work should investigate alternate possibilities for incorporating expected population distributions into the search directly, which may allow a more fine-grained inclusion of spinning regions of the parameter space, while sacrificing less in overall sensitivity to the most likely signals.

9.5 Conclusions

We have presented a new pipeline specifically targeted for the detection of gravitational-waves from binary neutron star sources in LIGO data. Using the single stage search pipeline we investigated the configuration choices used for PSD estimation, SNR thresholds, low frequency cutoff, and χ^2 bins used within the ranking statistic. To assess the sensitivity, we develop a method to measure the false-alarm rate of possible signals, and introduce the concept of both the inclusive and exclusive FAR measures. We find that for S6 data, the choices for low frequency cutoff at

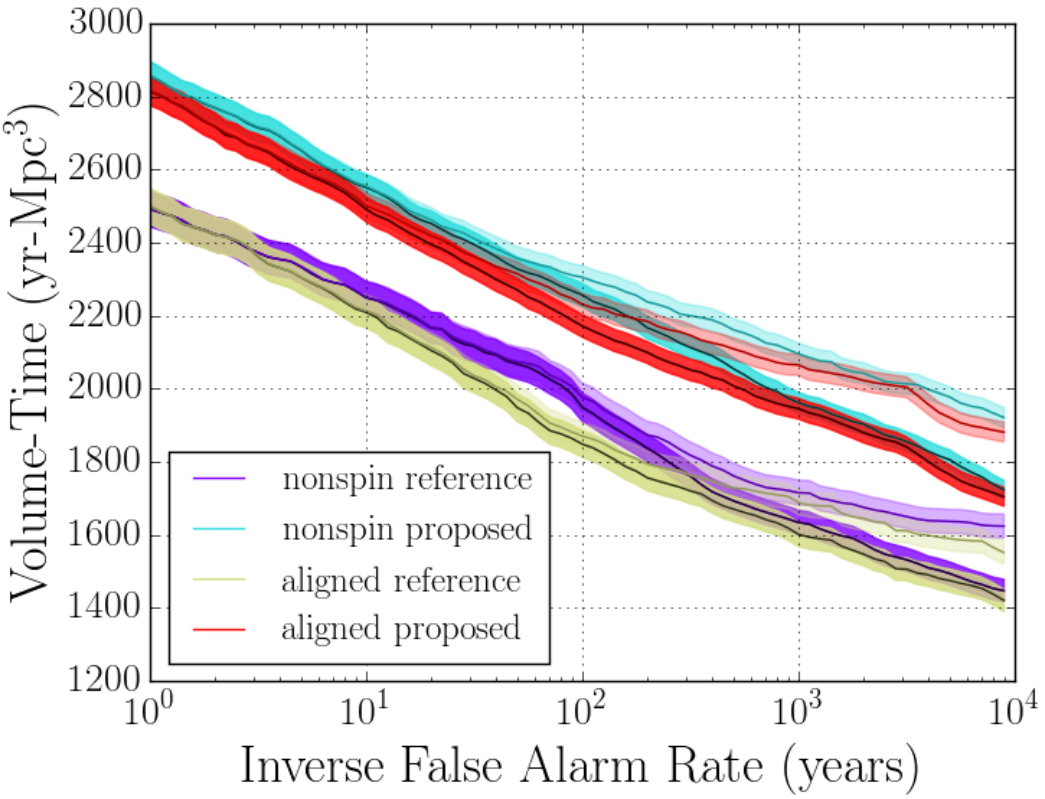

Figure 58: The combined VT as a function of inverse false-alarm rate, for the three sample analysis weeks, for an injection population that uniformly covers parameter space of the non-spinning BNS region, $1 - 3M_\odot$, where the spin angles are isotropically distributed, and the spin magnitude $|\chi| < 0.4$. Darker shaded lines indicate the inclusive IFAR value, while lighter lines show the exclusive IFAR. There is a negligible difference in search performance between using the aligned spin and nonspinning template bank.

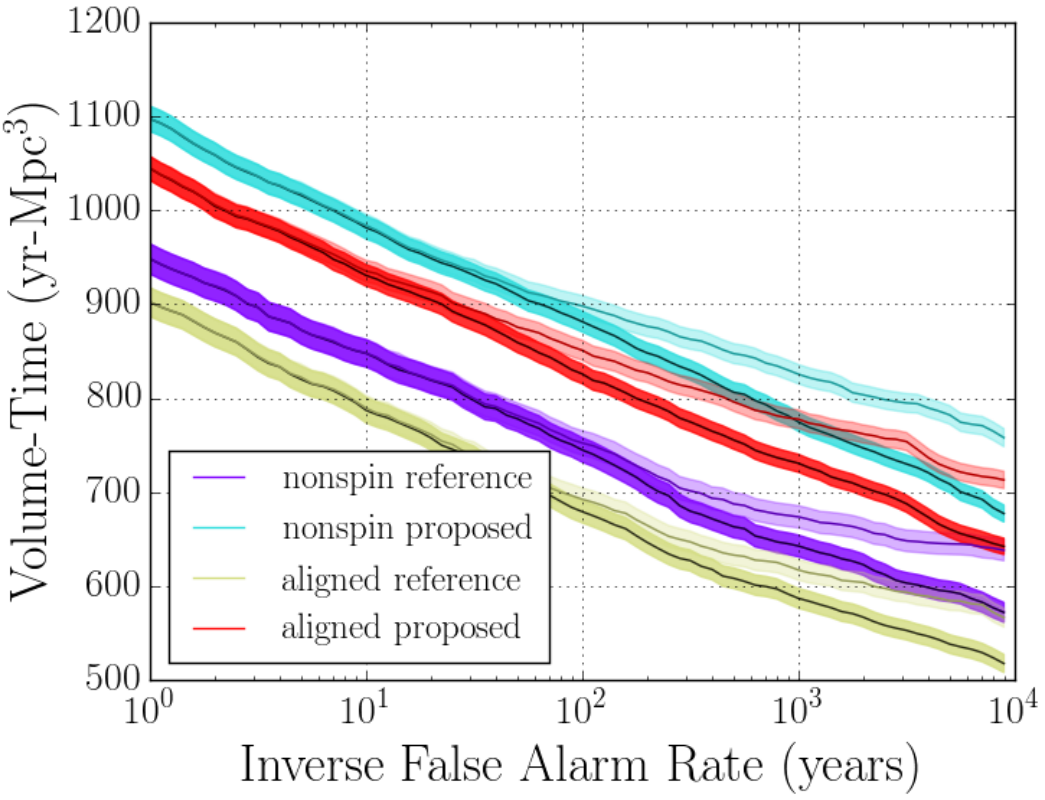

Figure 59: The VT as a function of inverse false-alarm rate, for the three sample analysis weeks, for an astrophysically-motivated conservative mass and spin distribution. Darker shaded lines indicate the inclusive IFAR value, while lighter lines show the exclusive IFAR. There is an $\approx 7\%$ drop in sensitivity when using the full aligned spin template bank when compared to the the non-spinning template bank.

40Hz, and the SNR threshold at 5.5, as used in prior S6/VSR2,3 searches for BNS sources, were appropriate. Additionally, we find that for a two detector search conducted using the Hanford and Livingston observatories, decreasing the SNR threshold below 5.3 will not result in any gain in search sensitivity using the conservative inclusive IFAR. In Sec. 9.3.1 and Sec. 9.3.3 we show significant improvements in search sensitivity for BNS sources by retuning the number of PSD samples per estimate, and the number of bins used in the signal consistence test, respectively. We find an additional 25% increase in the detection rate of BNS systems when using the retuned BNS search over a BNS search that uses the configuration proposed in Ch. 7, which already showed a 10% increase over the S6/VSR2,3 configuration. We also find that using an aligned spin template bank marginally decreases the sensitivity to BNS mergers for conservative estimates of the BNS populations when comparing to a bank of stictly non-spinning templates. As these tuning significantly differ from those used in the wider lowmass search performed in S6/VSR2,3, we propose that a focused, non-spinning search for binary neutron stars be conducted for aLIGO and AdV.

Chapter 10

Conclusions

We have investigated the effects of neglecting spin when searching for binary neutron star systems in aLIGO and AdV. We have found that if component spins in binary neutron star systems are as large as 0.4 then neutron star spin cannot be neglected, and there is a non-trivial loss in signal-to-noise ratio even if the maximum spin is restricted to be less than 0.05. We have shown that the geometric algorithm for placing and aligned spin template bank works for aligned spin systems and have demonstrated that it does significantly better for generic, precessing BNS systems than the traditional non-spinning bank. However, for the BNS aligned spin $\chi_i < 0.4$ parameter space the aligned spin bank requires approximately five times as many templates as the non-spinning bank. This increased number of templates will increase the computational cost of the search and increase the number of background events, so needs to be balanced against the potential gain in being able to cover a larger region of parameter space. A further advantage of this method is the ease with which it can be incorporated into existing or future search pipelines, which include the use of signal-based vetoes [58] and coincidence algorithms [115].

We have found that there is significant disagreement between NSBH waveforms modelled with the TaylorT2, TaylorT4, and SEOBNRv1 approximants. This will pose problems for the construction of optimal NSBH detection searches, potentially reducing the event rate, and may cause significant biases in the parameter measurement of detected signals. The discrepancies are not accounted for by the differences between frequency and time domain waveforms and start at fairly low ($v \sim 0.2$) orbital velocities. Since the discrepancies in the approximants result from how the

PN expansions of the energy and flux are combined and truncated, we conclude that the calculation of higher order PN terms is required to increase the faithfulness of these approximants, and more importantly, to improve the ability to detect NSBH coalescences. The discrepancies between approximants are significantly smaller when the spin of the black hole is close to zero, which further motivates the calculation of the PN terms associated with the spin of the objects beyond those known completely up to 2.5PN order and partially up to 3.5PN.

We have explored the effect that the angular momentum of the black hole will have on searches for neutron-star black-hole binaries with aLIGO. The black hole's angular momentum will affect the phase evolution of the emitted gravitational-wave signal, and, if the angular momentum is misaligned with the orbital plane, will cause the system to precess. We have found that if these effects are neglected in the filter waveforms used to search for NSBH binaries it will result in a loss in detection rate of $31-36\%$ when searching for NSBH systems with masses uniformly distributed in the range $(3-15, 1-3)M_{\odot}$. When restricting the masses to $(9.5-10.5, 1.35-1.45)M_{\odot}$ we find that the loss in detection rate is $33-37\%$. The error in these measurements is due to uncertainty in the PN waveform models used to simulate NSBH gravitational-wave signals. We have found that an aligned spin template bank offers a $16\%-30\%$ improvement in the detection rate of neutron-star black-hole mergers when compared to a non-spinning template bank when searching for NSBH systems with masses in the range $(3-15, 1-3)M_{\odot}$. However, when searching for NSBH systems with masses restricted to the range $(9.5-10.5, 1.35-1.45)M_{\odot}$ we find the improvement is reduced to $5-17\%$. Some systems are not recovered well with this new bank of filters. These systems are ones where the black-hole spin is misaligned with the orbit and the waveform is significantly modified due to precession of the orbital plane. This happens most often when m_{BH}/m_{NS} and the spin magnitude are both large. Note, that these results are for an idealized search that neglects the effects of non-Gaussian noise.

We have demonstrated the use of a new pipeline to search for gravitational waves from compact object binaries in LIGO data. We find that the sensitivity of the search pipeline used in S6/VSR2,3 is $\sim 10\%$ less sensitive at a false-alarm rate of 10^{-3} per year than the most sensitive pipeline proposed, which uses a shared fixed 3.5pN template bank in both detectors generated using a harmonic mean power spectral

density, and the exact-match coincidence test. The new pipeline uses a simpler, single-stage workflow that allows us to estimate false-alarm rates to $\sim 10^{-4}$ per year using one week of data. With our improved implementation of the χ^2 signal-based veto, we demonstrate that the new pipeline has the same computational cost as the two-stage workflow used in the S6/VSR2,3 analysis. We propose that this workflow be used as a basis for offline searches for gravitational waves from compact-object binary sources in aLIGO and AdV. Finally, we note that although the distribution of triggers in the S6 search using the ellipsoidal test is very close to that of Gaussian noise this is not the case for exact-match. This suggests that additional tuning is possible to increase the sensitivity of the search.

We have presented a new pipeline specifically tuned for the detection of gravitational-waves from binary neutron star sources in LIGO data. Using the single-stage search pipeline we investigated the configuration choices used for PSD estimation, SNR thresholds, low frequency cutoff, and χ^2 bins used within the ranking statistic. To assess the sensitivity, we develop a method to measure the false alarm rate of possible signals, and introduce the concept of both the inclusive and exclusive FAR measures. We find that for S6 data, the choices for low frequency cutoff at 40Hz, and the SNR threshold at 5.5, as used in prior S6/VSR2,3 searches for BNS sources, were appropriate. Additionally, we find that for a two detector search conducted using the Hanford and Livingston observatories, decreasing the SNR threshold below 5.3 will not result in any gain in search sensitivity using the conservative inclusive IFAR. We show significant improvements in search sensitivity for BNS sources by retuning the number of PSD samples per estimate, and the number of bins used in the signal consistence test, respectively. We find an additional 25% increase in the detection rate of BNS systems when using the retuned BNS search over a BNS search that uses the initially proposed single-stage pipeline, which had already demonstrated a 10% improvement over the S6/VSR2,3 configuration. We also find that using an aligned spin template bank marginally decreases the sensitivity to BNS mergers for conservative estimates of the BNS populations when comparing to a bank of stictly non-spinning templates. As these tuning significantly differ from those used in the wider lowmass search performed in S6/VSR2,3, we propose that a focused, non-spinning search for binary neutron stars be conducted for aLIGO and AdV.

Appendix A

Post-Newtonian Waveforms

A.1 Post-Newtonian Energy and Gravitational-wave Flux

In this appendix, we give the PN coefficients for the center of mass energy E_i and the gravitational-wave flux F_i, whose contributions were derived and presented in [161, 162, 163, 72, 121, 73, 130, 110, 111, 164, 126, 117]. We include corrections that involve the component objects' spins up to 3.5PN. These coefficients depend on the dimensionless spins of the component objects $\chi_i = \mathbf{S}_i/m_i^2$, their projections onto the direction of so-called Newtonian orbital angular momentum $\mathbf{L}_N = M\eta\mathbf{r}\times\dot{\mathbf{r}}$, and the symmetric mass ratio η. Additionally, quadrupole-monopole contributions depend on a parameter q_i, which quantifies the strength of the quadrupole moment induced by the oblateness of each spinning compact object. For BHs, $q_i = 1$, while for NSs q_i will depend on the equation of state, with [165] finding $q_i \sim 2 - 12$.

The coefficients associated with the energy are given as

$$E_{\rm Newt} = -\frac{M}{2}\eta, \tag{A.1}$$

$$E_2 = -\frac{3}{4} - \frac{1}{12}\eta, \tag{A.2}$$

$$E_3 = \sum_{i=1}^{2} \left[\frac{8}{3}\left(\frac{m_i}{M}\right)^2 + 2\eta\right]\left(\chi_i \cdot \hat{L}_N\right), \tag{A.3}$$

$$E_4 = -\frac{27}{8} + \frac{19}{8}\eta - \frac{1}{24}\eta^2 + \eta\left[\chi_1 \cdot \chi_2 - 3\left(\chi_1 \cdot \hat{L}_N\right)\left(\chi_2 \cdot \hat{L}_N\right)\right] + \frac{1}{2}\sum_{i=1}^{2} q_i \left(\frac{m_i}{M}\right)^2 \left[\chi_i^2 - 3\left(\chi_i \cdot \hat{L}_N\right)^2\right], \tag{A.4}$$

$$E_5 = \sum_{i=1}^{2} \left[\left(8 - \frac{31}{9}\eta\right)\left(\frac{m_i}{M}\right)^2 + \eta\left(3 - \frac{10}{3}\eta\right)\right]\left(\chi_i \cdot \hat{L}_N\right), \tag{A.5}$$

$$E_6 = -\frac{675}{64} + \left(\frac{34\,445}{576} - \frac{205}{96}\pi^2\right)\eta - \frac{155}{96}\eta^2 - \frac{35}{5184}\eta^3, \tag{A.6}$$

$$E_7 = \sum_{i=1}^{2} \left[\left(27 - \frac{211}{4}\eta + \frac{7}{6}\eta^2\right)\left(\frac{m_i}{M}\right)^2 + \eta\left(\frac{27}{4} - 39\eta + \frac{5}{4}\eta^2\right)\right]\left(\chi_i \cdot \hat{L}_N\right). \tag{A.7}$$

The coefficients associated with the flux are given as

$$F_{\text{Newt}} = \frac{32}{5}\eta^2, \tag{A.8}$$

$$F_2 = -\frac{1247}{336} - \frac{35}{12}\eta, \tag{A.9}$$

$$F_3 = 4\pi - \sum_{i=1}^{2} \left[\frac{11}{4}\left(\frac{m_i}{M}\right)^2 + \frac{5}{4}\eta\right]\left(\chi_i \cdot \hat{L}_N\right), \tag{A.10}$$

$$
\begin{aligned}
F_4 &= -\frac{44\,711}{9072} + \frac{9271}{504}\eta + \frac{65}{18}\eta^2 + \eta\left[\frac{289}{48}\left(\chi_1\cdot\hat{L}_N\right)\left(\chi_2\cdot\hat{L}_N\right) - \frac{103}{48}\chi_1\cdot\chi_2\right] \\
&+ \sum_{i=1}^{2} q_i\left(\frac{m_i}{M}\right)^2\left[3\left(\chi_i\cdot\hat{L}_N\right)^2 - \chi_i^2\right] + \frac{1}{96}\left(\frac{m_i}{M}\right)^2\left[7\chi_i^2 - \left(\chi_i\cdot\hat{L}_N\right)^2\right],
\end{aligned} \tag{A.11}
$$

$$
F_5 = \left(-\frac{8191}{672} - \frac{583}{24}\eta\right)\pi + \sum_{i=1}^{2}\left[\left(-\frac{59}{16} + \frac{701}{36}\eta\right)\left(\frac{m_i}{M}\right)^2 + \eta\left(-\frac{13}{16} + \frac{43}{4}\eta\right)\right]\left(\chi_i\cdot\hat{L}_N\right), \tag{A.12}
$$

$$
\begin{aligned}
F_6 &= \frac{6\,653\,739\,519}{69\,854\,400} + \frac{16}{3}\pi^2 - \frac{1712}{105}\gamma_E - \frac{856}{105}\log(16v^2) + \left(-\frac{134\,543}{7776} + \frac{41}{48}\pi^2\right)\eta \\
&- \frac{94\,403}{3024}\eta^2 - \frac{775}{324}\eta^3 - \pi\sum_{i=1}^{2}\left[\frac{65}{6}\left(\frac{m_i}{M}\right)^2 - \frac{31}{6}\eta\right]\left(\chi_i\cdot\hat{L}_N\right),
\end{aligned} \tag{A.13}
$$

$$
\begin{aligned}
F_7 &= \left(-\frac{16\,285}{504} + \frac{214\,745}{1728}\eta + \frac{193\,385}{3024}\eta^2\right)\pi \\
&+ \sum_{i=1}^{2}\left[\left(\frac{162\,035}{3888} + \frac{971}{54}\eta - \frac{6737}{108}\eta^2\right)\left(\frac{m_i}{M}\right)^2 + \eta\left(\frac{9535}{336} + \frac{1849}{126}\eta - \frac{1501}{36}\eta^2\right)\right]\left(\chi_i\cdot\hat{L}_N\right).
\end{aligned} \tag{A.14}
$$

A.2 Post-Newtonian Approximants

The PN approximants TaylorT4, TaylorT2, TaylorF2, and TaylorR2F4 are given using the flux up to 3.5 PN and the center-of-mass energy up to 3.0 PN. Corrections due to spin are included up to 3.5 PN order. This includes the leading order spin orbit correction β at 1.5PN, leading order spin-spin correction σ at 2PN (which includes quadrupole-monopole and so-called self-spin effects proportional to s_i^2), next-to-leading order spin-orbit corrections γ at 2.5PN, tail-induced spin

orbit correction ξ at 3PN, and third order spin-orbit correction ζ appearing at 3.5PN. These corrections can be expressed as,

$$\beta = \sum_{i=1}^{2} \left[\frac{113}{12} \left(\frac{m_i}{M} \right)^2 + \frac{25}{4}\eta \right] \left(\chi_i \cdot \hat{L}_N \right), \tag{A.15}$$

$$\begin{aligned} \sigma = \eta \Bigg[& \frac{721}{48} \left(\chi_1 \cdot \hat{L}_N \right) \left(\chi_2 \cdot \hat{L}_N \right) - \frac{247}{48} \chi_1 \cdot \chi_2 \Bigg] \\ & + \frac{5}{2} \sum_{i=1}^{2} q_i \left(\frac{m_i}{M} \right)^2 \left[3 \left(\chi_i \cdot \hat{L}_N \right)^2 - \chi_i^2 \right] \\ & + \frac{1}{96} \sum_{i=1}^{2} \left(\frac{m_i}{M} \right)^2 \left[7\chi_i^2 - \left(\chi_i \cdot \hat{L}_N \right)^2 \right], \end{aligned} \tag{A.16}$$

$$\gamma = \sum_{i=1}^{2} \left[\left(\frac{732\,985}{2268} + \frac{140}{9}\eta \right) \left(\frac{m_i}{M} \right)^2 + \eta \left(\frac{13\,915}{84} - \frac{10}{3}\eta \right) \right] \left(\chi_i \cdot \hat{L}_N \right), \tag{A.17}$$

$$\xi = \pi \sum_{i=1}^{2} \left[\frac{75}{2} \left(\frac{m_i}{M} \right)^2 + \frac{151}{6}\eta \right] \left(\chi_i \cdot \hat{L}_N \right), \tag{A.18}$$

$$\zeta = \sum_{i=1}^{2} \left[\left(\frac{130\,325}{756} - \frac{796\,069}{2016}\eta + \frac{100\,019}{864}\eta^2 \right) \left(\frac{m_i}{M} \right)^2 + \eta \left(\frac{1\,195\,759}{18\,144} - \frac{257\,023}{1008}\eta + \frac{2903}{32}\eta^2 \right) \right] \left(\chi_i \cdot \hat{L}_N \right). \tag{A.19}$$

A.2.1 TaylorT4

$$\begin{aligned} \frac{dv}{dt} = \frac{32\eta}{5M} v^9 \Bigg\{ 1 \;&+\; \left(-\frac{743}{336} - \frac{11}{4}\eta \right) v^2 + (4\pi - \beta) v^3 + \left(\frac{34\,103}{18\,144} + \frac{13\,661}{2016}\eta + \frac{59}{18}\eta^2 + \sigma \right) v^4 \\ &+\; \left(-\frac{4159\pi}{672} - \frac{189\pi}{8}\eta - \frac{9}{40}\gamma + \left(\frac{743}{168} + \frac{11}{2}\eta \right)\beta \right) v^5 \\ &+\; \Bigg[\frac{16\,447\,322\,263}{139\,708\,800} - \frac{1712\gamma_E}{105} + \frac{16\pi^2}{3} - \frac{1712}{105}\log(4v) \\ &\qquad + \left(-\frac{56\,198\,689}{217\,728} + \frac{451\pi^2}{48} \right)\eta + \frac{541}{896}\eta^2 - \frac{5605}{2592}\eta^3 - \xi \Bigg] v^6 \\ &+\; \pi \left(-\frac{4415}{4032} + \frac{358\,675}{6048}\eta + \frac{91\,495}{1512}\eta^2 - \zeta \right) v^7 \Bigg\} \end{aligned} \tag{A.20}$$

A.2.2 TaylorT2

$$\begin{aligned}\frac{dt}{dv} = \frac{5M}{32\eta}v^{-9}\Bigg\{1 \;&+\; \left(\frac{743}{336}+\frac{11}{4}\eta\right)v^2 + (-4\pi+\beta)\,v^3 + \left(\frac{3\,058\,673}{1\,016\,064}+\frac{5429}{1008}\eta+\frac{617}{144}\eta^2-\sigma\right)v^4 \\ &+\; \left(-\frac{7729\pi}{672}+\frac{13\pi}{8}\eta+\frac{9}{40}\gamma\right)v^5 \\ &+\; \Bigg[-\frac{10\,817\,850\,546\,611}{93\,884\,313\,600}+\frac{32\pi^2}{3}+\frac{1712\gamma_E}{105}+\frac{1712}{105}\log(4v) \\ &\qquad +\Big(\frac{3\,147\,553\,127}{12\,192\,768}-\frac{451\pi^2}{48}\Big)\eta-\frac{15\,211}{6912}\eta^2+\frac{25\,565}{5184}\eta^3-8\pi\beta+\xi\Bigg]v^6 \\ &+\; \pi\Bigg(-\frac{15\,419\,335}{1\,016\,064}-\frac{75\,703}{6048}\eta+\frac{14\,809}{3024}\eta^2-\beta\left(\frac{8\,787\,977}{1\,016\,064}+\frac{51\,841}{2016}\eta+\frac{2033}{144}\eta^2\right) \\ +\gamma\left(\frac{2229}{2240}+\frac{99}{80}\eta\right)+\zeta\Bigg)v^7\Bigg\}\end{aligned} \tag{A.21}$$

A.2.3 TaylorF2

$$A_{(F2)}(f) \propto \frac{(\pi M f)^{2/3}}{\sqrt{\dot{F}(f)}} \tag{A.22}$$

$$
\begin{aligned}
\psi_{(F2)}(f) &= 2\pi f t_c - \phi_c + \frac{3}{128\eta} v^{-5} \Bigg\{ 1 + \left(\frac{3715}{756} + \frac{55}{9}\eta \right) v^2 + (4\beta - 16\pi) v^3 \\
&+ \left(\frac{15\,293\,365}{508\,032} + \frac{27\,145}{504}\eta + \frac{3085}{72}\eta^2 - 10\sigma \right) v^4 + \left(\frac{38\,645}{756}\pi - \frac{65}{9}\pi\eta - \gamma \right) (1 + 3\log(v))\, v^5 \\
&+ \Bigg[\frac{11\,583\,231\,236\,531}{4\,694\,215\,680} - \frac{640}{3}\pi^2 - \frac{6848\gamma_E}{21} - \frac{6848}{21}\log(4v) + \left(-\frac{15\,737\,765\,635}{3\,048\,192} + \frac{2255\pi^2}{12} \right) \eta \\
&+ \frac{76\,055}{1728}\eta^2 - \frac{127\,825}{1296}\eta^3 + 160\pi\beta - 20\xi \Bigg] v^6 + \pi \left(\frac{77\,096\,675}{254\,016} + \frac{378\,515}{1512}\eta - \frac{74\,045}{756}\eta^2 \right) \\
&+ \beta \left(\frac{43\,939\,885}{254\,016} + \frac{259\,205}{504}\eta + \frac{10\,165}{36}\eta^2 \right) - \gamma \left(\frac{2229}{112} - \frac{99}{4}\eta \right) - 20\zeta \Bigg) v^7 \Bigg\} \qquad \text{(A.23)}
\end{aligned}
$$

A.2.4 TaylorR2F4

In the equation below, the a_i are the PN coefficients of the TaylorT4 expansion

$$
\left(\frac{dv}{dt} \right)_{T4} = A_7(v) = a_0 \left(1 + \sum_{i=2}^{7} a_i v^i + a_{6\log} v^6 \log(4v) \right).
$$

which can be read off of Eq. (A.20).

$$
\begin{aligned}
\psi_{(R2F4)}(f) &= \psi_{(F2)}(f) + \frac{3}{128\eta}v^{-5}\Bigg\{\Bigg[-20\beta^2+\sigma\left(\frac{3715}{42}+100\eta\right)\Bigg]v^6+\Bigg[(40\beta-160\pi)\,\sigma\Bigg]v^7 \\
&+ \frac{40}{9}\Bigg[\left(3a_2^2a_4-a_2^4-a_4^2-2a_3a_5+3a_2a_3^2-2a_2a_6+\frac{2}{3}a_2a_{6\log}\right)(1-3\log(v)) \\
&+ 3a_2a_{6\log}\log(4v)^2\Bigg]v^8+5\Bigg[8a_2^2a_3-2a_3^3-12a_2a_3a_4-6a_2^2a_5+4a_4a_5+4a_3a_6-5a_3a_{6\log} \\
&+ 4a_2a_7+4a_3a_{6\log}\log(4v)\Bigg]v^9+4\Bigg[-a_2^5+6a_2^2a_3^2+4a_2^3a_4-3a_3^2a_4-3a_2a_4^2-6a_2a_3a_5 \\
&+ a_5^2-3a_2^2a_6+2a_4a_6+2a_3a_7+\left(\frac{21}{10}a_2^2-\frac{7}{5}a_4\right)a_{6\log}+\left(2a_4a_{6\log}-3a_2^2a_{6\log}\right)\log(4v)\Bigg]v^{10} \\
&+ \frac{20}{9}\Bigg[-5a_2^4a_3+4a_2a_3^3+4a_2^3a_5+12a_2^2a_3a_4-3a_3a_4^2-3a_3^2a_5-6a_2a_4a_5-6a_2a_3a_6 \\
&+ 2a_5a_6+3a_2a_3a_{6\log}-a_5a_{6\log}+2a_4a_7-3a_2^2a_7+(2a_5-6a_2a_3)\,a_{6\log}\log(4v)\Bigg]v^{11} \\
&+ \frac{10}{7}\Bigg[a_2^6-10a_2^3a_3^2+a_3^4-5a_2^4a_4+12a_2a_3^2a_4+6a_2^2a_4^2-a_4^3+12a_2^2a_3a_5-6a_3a_4a_5-3a_2a_5^2 \\
&+ 4a_2^3a_6-3a_3^2a_6-6a_2a_4a_6+a_6^2+\left(-\frac{11}{7}a_2^3+\frac{33}{28}a_3^2+\frac{33}{14}a_2a_4-\frac{11}{14}a_6+\frac{93}{392}a_{6\log}\right)a_{6\log}-6a_2a_3a_7 \\
&+ 2a_5a_7+\left(4a_2^3-3a_3^2-6a_2a_4+2a_6-\frac{11}{14}a_{6\log}\right)a_{6\log}\log(4v)+a_{6\log}^2\log(4v)^2\Bigg]v^{12}\Bigg\} \qquad \text{(A.24)}
\end{aligned}
$$

Bibliography

[1] A Einstein. Sb preuss. *Akad. Wise*, page 688, 1916.

[2] R. A. Hulse and J. H. Taylor. Discovery of a pulsar in a binary system. *Astrophys. J.*, 195:L51–L53, 1975.

[3] J. M. Weisberg, J. H. Taylor, and L. A. Fowler. GRAVITATIONAL WAVES FROM AN ORBITING PULSAR. *Sci. Am.*, 245:66–74, 1981.

[4] G. F. Moss, L. R. Miller, and Forward R. L. Photon-noise-limited laser tranducer for gravitational antenna. *Applied Optics*, 10:2495–2498, 1971.

[5] R Weiss. Electromagnetically coupled broadband gravitational wave antenna. *Quarterly Progress Report of the Research Laboratory of Electronics of the Massachsetts Institutue of Technology*, 105:54, April 1972.

[6] R. P. Drever et al. A gravity-wave detector using optical cavity sensing. In E. Schmutzer, editor, *Proceedings of the Ninth International Conference on General Relativity and Gravitation*, pages 265–267. Cambridge University Press, Cambridge, UK, 1983.

[7] B. Abbott et al. Analysis of LIGO data for gravitational waves from binary neutron stars. *Phys. Rev.*, D69:122001, 2004.

[8] B. Abbott et al. Search for gravitational waves from galactic and extra-galactic binary neutron stars. *Phys. Rev.*, D72:082001, 2005.

[9] B. Abbott et al. Search for gravitational waves from binary black hole inspirals in ligo data. *Phys. Rev.*, D73:062001, 2006.

[10] B. Abbott et al. Search for gravitational waves from binary inspirals in S3 and S4 LIGO data. *Phys.Rev.*, D77:062002, 2008.

[11] B. Abbott et al. Search of S3 LIGO data for gravitational wave signals from spinning black hole and neutron star binary inspirals. *Phys. Rev.*, D78:042002, 2008.

[12] B.P. Abbott et al. Search for Gravitational Waves from Low Mass Binary Coalescences in the First Year of LIGO's S5 Data. *Phys.Rev.*, D79:122001, 2009.

[13] B.P. Abbott et al. Search for Gravitational Waves from Low Mass Compact Binary Coalescence in 186 Days of LIGO's fifth Science Run. *Phys.Rev.*, D80:047101, 2009.

[14] J. Abadie et al. Search for Gravitational Waves from Compact Binary Coalescence in LIGO and Virgo Data from S5 and VSR1. *Phys. Rev.*, D82:102001, 2010.

[15] J. Abadie et al. Search for Gravitational Waves from Low Mass Compact Binary Coalescence in LIGO's Sixth Science Run and Virgo's Science Runs 2 and 3. *Phys.Rev.*, D85:082002, 2012.

[16] J. Aasi et al. Advanced LIGO. *Class. Quant. Grav.*, 32:074001, 2015.

[17] J. Aasi et al. Prospects for Localization of Gravitational Wave Transients by the Advanced LIGO and Advanced Virgo Observatories. 2013.

[18] F. Acernese. The Advanced Virgo detector. *J. Phys. Conf. Ser.*, 610(1):012014, 2015.

[19] Gregory M. Harry et al. Advanced LIGO: The next generation of gravitational wave detectors. *Class.Quant.Grav.*, 27:084006, 2010.

[20] F. Acernese et al. Advanced Virgo Baseline Design, 2009. [Virgo Techincal Document VIR-0027A-09].

[21] J. Abadie et al. Predictions for the Rates of Compact Binary Coalescences Observable by Ground-based Gravitational-wave Detectors. *Class.Quant.Grav.*, 27:173001, 2010.

[22] B.S. Sathyaprakash and Bernard F. Schutz. Physics, astrophysics and cosmology with gravitational waves. *Living Reviews in Relativity*, 12(2), 2009.

[23] David Eichler, Mario Livio, Tsvi Piran, and David N. Schramm. Nucleosynthesis, Neutrino Bursts and Gamma-Rays from Coalescing Neutron Stars. *Nature*, 340:126–128, 1989.

[24] Ramesh Narayan, Bohdan Paczynski, and Tsvi Piran. Gamma-ray bursts as the death throes of massive binary stars. *Astrophys.J.*, 395:L83–L86, 1992.

[25] Bohdan Paczynski. Cosmological gamma-ray bursts. *Acta Astron.*, 41:257–267, 1991.

[26] Edo Berger. The Environments of Short-Duration Gamma-Ray Bursts and Implications for their Progenitors. *New Astron.Rev.*, 55:1–22, 2011.

[27] Chris L. Fryer, Krzysztof Belczynski, Grzegorz Wiktorowicz, Michal Dominik, Vicky Kalogera, et al. Compact Remnant Mass Function: Dependence on the Explosion Mechanism and Metallicity. *Astrophys.J.*, 749:91, 2012.

[28] Mark Hannam, Duncan A. Brown, Stephen Fairhurst, Chris L. Fryer, and Ian W. Harry. When can gravitational-wave observations distinguish between black holes and neutron stars? *Astrophys.J.*, 766:L14, 2013.

[29] Alessandra Buonanno, Bala Iyer, Evan Ochsner, Yi Pan, and B.S. Sathyaprakash. Comparison of post-Newtonian templates for compact binary inspiral signals in gravitational-wave detectors. *Phys.Rev.*, D80:084043, 2009.

[30] Duncan A. Brown, Prayush Kumar, and Alexander H. Nitz. Template banks to search for low-mass binary black holes in advanced gravitational-wave detectors. *Phys. Rev. D*, 87:082004, Apr 2013.

[31] A. H. Nitz, A. Lundgren, D. A. Brown, E. Ochsner, et al. Accuracy of gravitational waveform models for observing neutron-star–black-hole binaries in Advanced LIGO. *ArXiv e-prints*, July 2013.

[32] Prayush Kumar, Kevin Barkett, Swetha Bhagwat, Nousha Afshari, Duncan A. Brown, Geoffrey Lovelace, Mark A. Scheel, and Bla Szilgyi. Accuracy and precision of gravitational-wave models of inspiraling neutron star – black hole binaries with spin: comparison with numerical relativity in the low-frequency regime. 2015.

[33] Luc Blanchet. Gravitational Radiation from Post-Newtonian Sources and Inspiralling Compact Binaries. *Living Rev.Rel.*, 17:2, 2014.

[34] A. Buonanno and T. Damour. Effective one-body approach to general relativistic two-body dynamics. *Phys. Rev.*, D59:084006, 1999.

[35] Yi Pan, Alessandra Buonanno, Luisa T. Buchman, Tony Chu, Lawrence E. Kidder, Harald P. Pfeiffer, and Mark A. Scheel. Effective-one-body waveforms calibrated to numerical relativity simulations: coalescence of non-precessing, spinning, equal-mass black holes. *Phys. Rev.*, D81:084041, 2010.

[36] Thibault Damour, Alessandro Nagar, and Sebastiano Bernuzzi. Improved effective-one-body description of coalescing nonspinning black-hole binaries and its numerical-relativity completion. *Phys.Rev.*, D87:084035, 2013.

[37] Andrea Taracchini et al. Effective-one-body model for black-hole binaries with generic mass ratios and spins. *Phys. Rev.*, D89(6):061502, 2014.

[38] Thibault Damour and Alessandro Nagar. New effective-one-body description of coalescing nonprecessing spinning black-hole binaries. *Phys. Rev.*, D90(4):044018, 2014.

[39] Luc Blanchet. Gravitational radiation from post-Newtonian sources and inspiralling compact binaries. *Living Rev.Rel.*, 9:4, 2006.

[40] P.C. Peters and J. Mathews. Gravitational radiation from point masses in a Keplerian orbit. *Phys.Rev.*, 131:435–439, 1963.

[41] Luc Blanchet, Thibault Damour, and Bala R. Iyer. Gravitational waves from inspiralling compact binaries: Energy loss and wave form to second postNewtonian order. *Phys. Rev.*, D51:5360, 1995.

[42] Luc Blanchet, Thibault Damour, Bala R. Iyer, Clifford M. Will, and Alan. G. Wiseman. Gravitational radiation damping of compact binary systems to second postNewtonian order. *Phys. Rev. Lett.*, 74:3515–3518, 1995.

[43] Luc Blanchet, Bala R. Iyer, Clifford M. Will, and Alan G. Wiseman. Gravitational wave forms from inspiralling compact binaries to second-post-newtonian order. *Class. Quantum Grav.*, 13:575–584, 1996.

[44] A. G. Wiseman. Coalescing binary-systems of compact objects to 5/2-post-newtonian order. iv. the gravitational-wave tail. *Phys. Rev. D*, 48:4757, 1993.

[45] Luc Blanchet, Guillaume Faye, Bala R. Iyer, and Benoit Joguet. Gravitational-wave inspiral of compact binary systems to 7/2 post-newtonian order. *Phys. Rev. D*, 65:061501(R), 2002. Erratum-ibid **71**, 129902(E) (2005).

[46] Luc Blanchet, Thibault Damour, Gilles Esposito-Farese, and Bala R. Iyer. Gravitational radiation from inspiralling compact binaries completed at the third post-Newtonian order. *Phys.Rev.Lett.*, 93:091101, 2004.

[47] J. Abadie et al. Calibration of the LIGO Gravitational Wave Detectors in the Fifth Science Run. *Nucl. Instrum. Meth.*, A624:223–240, 2010.

[48] Bruce Allen, Warren G. Anderson, Patrick R. Brady, Duncan A. Brown, and Jolien D.E. Creighton. FINDCHIRP: An Algorithm for detection of gravitational waves from inspiraling compact binaries. *Phys.Rev.*, D85:122006, 2012.

[49] B.S. Sathyaprakash and S.V. Dhurandhar. Choice of filters for the detection of gravitational waves from coalescing binaries. *Phys.Rev.*, D44:3819–3834, 1991.

[50] S. V. Dhurandhar and B. S. Sathyaprakash. Choice of filters for the detection of gravitational waves from coalescing binaries. 2. Detection in colored noise. *Phys. Rev.*, D49:1707–1722, 1994.

[51] Benjamin J. Owen. Search templates for gravitational waves from inspiraling binaries: Choice of template spacing. *Phys.Rev.*, D53:6749–6761, 1996.

[52] Benjamin J. Owen and B. S. Sathyaprakash. Matched filtering of gravitational waves from inspiraling compact binaries: Computational cost and template placement. *Phys.Rev.*, D60:022002, 1999.

[53] S. Babak, R. Balasubramanian, D. Churches, T. Cokelaer, and B.S. Sathyaprakash. A Template bank to search for gravitational waves from inspiralling compact binaries. I. Physical models. *Class.Quant.Grav.*, 23:5477–5504, 2006.

[54] Thomas Cokelaer. Gravitational waves from inspiralling compact binaries: Hexagonal template placement and its efficiency in detecting physical signals. *Phys.Rev.*, D76:102004, 2007.

[55] Duncan A. Brown, Ian Harry, Andrew Lundgren, and Alexander H. Nitz. Detecting binary neutron star systems with spin in advanced gravitational-wave detectors. *Phys.Rev.*, D86:084017, 2012.

[56] Drew Keppel. The balancing act of template bank construction: inspiral waveform template banks for gravitational-wave detectors and optimizations at fixed computational cost. 2013.

[57] Drew Keppel. Metrics for multi-detector template placement in searches for short-duration nonprecessing inspiral gravitational-wave signals. *ArXiv e-prints, 1307.4158*, 2013.

[58] Bruce Allen. A chi**2 time-frequency discriminator for gravitational wave detection. *Phys.Rev.*, D71:062001, 2005.

[59] S. Babak, R. Biswas, P.R. Brady, D.A. Brown, K. Cannon, et al. Searching for gravitational waves from binary coalescence. *Phys.Rev.*, D87:024033, 2013.

[60] Duncan A. Brown et al. Searching for Gravitational Waves from Binary Inspirals with LIGO. *Class. Quant. Grav.*, 21:S1625–S1633, 2004.

[61] Duncan A Brown. Using the INSPIRAL program to search for gravitational waves from low-mass binary inspiral. *Class. Quant. Grav.*, 22:S1097–S1108, 2005.

[62] J. Aasi et al. The characterization of Virgo data and its impact on gravitational-wave searches. *Class.Quant.Grav.*, 29:155002, 2012.

[63] J. Aasi et al. Characterization of the LIGO detectors during their sixth science run. *Class. Quant. Grav.*, 32(11):115012, 2015.

[64] D. A. Brown et al. A case study on the use of workflow technologies for scientific analysis: Gravitation al wave data analysis. In Ian J. Taylor, Ewa Deelman, Dennis Gannon, and Matthew S. Shields, editors, *Workflows for e-Science*, chapter 5, pages 41–61. Springer-Verlag, 2006.

[65] T. A. Apostolatos. Search templates for gravitational waves from precessing, inspiraling binaries. *Phys.Rev.*, D52:605–620, 1995.

[66] B. P. Abbott et al. Implementation and testing of the first prompt search for gravitational wave transients with electromagnetic counterparts. *Astron. Astrophys.*, 539:A124, 2012.

[67] T. Dal Canton, S. Bhagwat, S.V. Dhurandhar, and A. Lundgren. Effect of sine-Gaussian glitches on searches for binary coalescence. *Class.Quant.Grav.*, 31:015016, 2014.

[68] Bulent Kiziltan, Athanasios Kottas, and Stephen E. Thorsett. The Neutron Star Mass Distribution. 2010.

[69] Paulo Cesar Carvalho Freire, Scott M. Ransom, Steve Begin, Ingrid H. Stairs, Jason W.T. Hessels, et al. Eight New Millisecond Pulsars in NGC 6440 and NGC 6441. *Astrophys.J.*, 2007.

[70] Lawrence E. Kidder, Clifford M. Will, and Alan G. Wiseman. Spin effects in the inspiral of coalescing compact binaries. *Phys. Rev.*, D47:4183, 1993.

[71] Theocharis A. Apostolatos, C. Cutler, G. J. Sussman, and K. S. Thorne. Spin induced orbital precession and its modulation of the gravitational wave forms from merging binaries. *Phys. Rev.*, D49:6274–6297, 1994.

[72] Lawrence E. Kidder. Coalescing binary systems of compact objects to post-Newtonian 5/2 order. 5. Spin effects. *Phys. Rev.*, D52:821–847, 1995.

[73] Luc Blanchet, Alessandra Buonanno, and Guillaume Faye. Higher-order spin effects in the dynamics of compact binaries. II. Radiation field. *Phys. Rev.*

D, 74(10):104034, November 2006. Note the two associated errata; the arXiv version has been corrected.

[74] Ka-Wai Lo and Lap-Ming Lin. The spin parameter of uniformly rotating compact stars. *Astrophys.J.*, 728:12, 2011.

[75] D.R. Lorimer. Binary and Millisecond Pulsars. *Living Rev.Rel.*, 11:8, 2008.

[76] Ilya Mandel and Richard O'Shaughnessy. Compact Binary Coalescences in the Band of Ground-based Gravitational-Wave Detectors. *Class. Quant. Grav.*, 27:114007, 2010.

[77] Lars Bildsten et al. Observations of accreting pulsars. *Astrophys J. Supp.*, 113:367, 1997.

[78] D. Chakrabarty. *AIP Conference Series*, 1068:67–74, October 2008.

[79] Marta Burgay, N. D'Amico, A. Possenti, R.N. Manchester, A.G. Lyne, et al. An Increased estimate of the merger rate of double neutron stars from observations of a highly relativistic system. *Nature*, 426:531–533, 2003.

[80] Feryal Ozel, Dimitrios Psaltis, Ramesh Narayan, and Jeffrey E. McClintock. The Black Hole Mass Distribution in the Galaxy. *Astrophys.J.*, 725:1918–1927, 2010.

[81] Will M. Farr et al. The Mass Distribution of Stellar-Mass Black Holes. *Astrophys.J.*, 741:103, 2011.

[82] Laura Kreidberg, Charles D. Bailyn, Will M. Farr, and Vassiliki Kalogera. Mass Measurements of Black Holes in X-Ray Transients: Is There a Mass Gap? *Astrophys.J.*, 757:36, 2012.

[83] A.H. Prestwich, R. Kilgard, P.A. Crowther, S. Carpano, A.M.T. Pollock, et al. The Orbital Period of the Wolf-Rayet Binary IC 10 X-1: Dynamic Evidence that the Compact Object is a Black Hole. *Astrophys.J.*, 669:L21–L24, 2007.

[84] Jeffrey M. Silverman and Alexei V. Filippenko. On IC 10 X-1, the Most Massive Known Stellar-Mass Black Hole. *Astrophys.J.*, 678:L17–L20, 2008.

[85] J.M. Miller, C.S. Reynolds, A.C. Fabian, G. Miniutti, and L.C. Gallo. Stellar-mass Black Hole Spin Constraints from Disk Reflection and Continuum Modeling. *Astrophys.J.*, 697:900–912, 2009.

[86] P.C. Peters. Gravitational Radiation and the Motion of Two Point Masses. *Phys.Rev.*, 136:B1224–B1232, 1964.

[87] Alessandra Buonanno, Yan-bei Chen, and Michele Vallisneri. Detecting gravitational waves from precessing binaries of spinning compact objects: Adiabatic limit. *Phys.Rev.*, D67:104025, 2003.

[88] Serge Droz, Daniel J. Knapp, Eric Poisson, and Benjamin J. Owen. Gravitational waves from inspiraling compact binaries: Validity of the stationary phase approximation to the Fourier transform. *Phys.Rev.*, D59:124016, 1999.

[89] Luc Blanchet, Bala R. Iyer, Clifford M. Will, and Alan G. Wiseman. Gravitational wave forms from inspiralling compact binaries to second postNewtonian order. *Class.Quant.Grav.*, 13:575–584, 1996.

[90] B. Abbott et al. Search for gravitational waves from primordial black hole binary coalescences in the galactic halo. *Phys. Rev.*, D72:082002, 2005.

[91] B. Abbott et al. Joint LIGO and TAMA300 search for gravitational waves from inspiralling neutron star binaries. *Phys.Rev.*, D73:102002, 2006.

[92] B. P. Abbott et al. Search for gravitational-wave bursts in the first year of the fifth LIGO science run. *Phys. Rev.*, D80:102001, 2009.

[93] B. Abbott et al. Implications for the Origin of GRB 070201 from LIGO Observations. *Astrophys. J.*, 681:1419–1428, 2008.

[94] J. Abadie et al. Search for gravitational-wave inspiral signals associated with short Gamma-Ray Bursts during LIGO's fifth and Virgo's first science run. *Astrophys. J.*, 715:1453–1461, 2010.

[95] M.S. Briggs et al. Search for gravitational waves associated with gamma-ray bursts during LIGO science run 6 and Virgo science runs 2 and 3. *Astrophys.J.*, 760:12, 2012.

[96] Andrea Taracchini, Yi Pan, Alessandra Buonanno, Enrico Barausse, Michael Boyle, et al. Prototype effective-one-body model for nonprecessing spinning inspiral-merger-ringdown waveforms. *Phys.Rev.*, D86:024011, 2012.

[97] Theocharis A. Apostolatos. Construction of a template family for the detection of gravitational waves from coalescing binaries. *Phys.Rev.*, D54:2421–2437, 1996.

[98] P. Ajith. Addressing the spin question in gravitational-wave searches: Waveform templates for inspiralling compact binaries with nonprecessing spins. *Phys.Rev.*, D84:084037, 2011.

[99] S. Babak et al. A template bank to search for gravitational waves from inspiralling compact binaries. I: Physical models. *Class. Quant. Grav.*, 23:5477–5504, 2006.

[100] Ian W. Harry, Bruce Allen, and B.S. Sathyaprakash. A Stochastic template placement algorithm for gravitational wave data analysis. *Phys.Rev.*, D80:104014, 2009.

[101] Jonathan Grindlay, Simon Portegies Zwart, and Stephen McMillan. Short gamma-ray bursts from binary neutron star mergers in globular clusters. *Nature Physics*, 2:116, 2006.

[102] Will M. Farr et al. Spin Tilts in the Double Pulsar Reveal Supernova Spin Angular-Momentum Production. *Astrophys.J.*, 742:81, 2011.

[103] Curt Cutler et al. The last three minutes: issues in gravitational wave measurements of coalescing compact binaries. *Phys. Rev. Lett.*, 70:2984–2987, 1993.

[104] Serge Droz, Daniel J. Knapp, Eric Poisson, and Benjamin J. Owen. Gravitational waves from inspiraling compact binaries: Validity of the stationary-phase approximation to the fourier transform. *Phys. Rev. D*, 59(12):124016, May 1999.

[105] Benjamin J. Owen and B. S. Sathyaprakash. Matched filtering of gravitational waves from inspiraling compact binaries: Computational cost and template placement. *Phys. Rev.*, D60:022002, 1999.

[106] A. Buonanno, Y. Chen, and M. Vallisneri. Detection template families for precessing binaries of spinning compact binaries: Adiabatic limit. *Phys. Rev. D*, 67:104025, 2003. Erratum-ibid. **D** 74, 029904(E) (2006).

[107] LSC Algorithm Library Suite. https://www.lsc-group.phys.uwm.edu/daswg/projects/lalsuite.html.

[108] B. Abbott et al. Advanced ligo anticipated sensitivity curves. Technical Report LIGO-T0900288-v3, 2010.

[109] E. Poisson and C. M. Will. Gravitational waves from inspiralling compact binaries - parameter-estimation using second-post-newtonian wave-forms. *Phys. Rev. D*, 52:848, 1995.

[110] Balazs Mikoczi, Matyas Vasuth, and Laszlo A. Gergely. Self-interaction spin effects in inspiralling compact binaries. *Phys.Rev.*, D71:124043, 2005.

[111] K.G. Arun, Alessandra Buonanno, Guillaume Faye, and Evan Ochsner. Higher-order spin effects in the amplitude and phase of gravitational waveforms emitted by inspiraling compact binaries: Ready-to-use gravitational waveforms. *Phys.Rev.*, D79:104023, 2009.

[112] Stanislav Babak. Building a stochastic template bank for detecting massive black hole binaries. *Class. Quant. Grav.*, 25:195011, 2008.

[113] Gian Mario Manca and Michele Vallisneri. Cover art: Issues in the metric-guided and metric-less placement of random and stochastic template banks. *Phys.Rev.*, D81:024004, 2010.

[114] Duncan A. Brown, Andrew Lundgren, and R. O'Shaughnessy. Nonspinning searches for spinning binaries in ground-based detector data: Amplitude and mismatch predictions in the constant precession cone approximation. 2012.

[115] C. A. K. Robinson, B. S. Sathyaprakash, and Anand S. Sengupta. A geometric algorithm for efficient coincident detection of gravitational waves. *Phys. Rev.*, D78:062002, 2008.

[116] Liliana E. Simone, Stephen W. Leonard, Eric Poisson, and Clifford M. Will. Gravitational waves from binary systems in circular orbits: Does the postNewtonian expansion converge? *Class.Quant.Grav.*, 14:237–256, 1997.

[117] Alejandro Boh, Sylvain Marsat, and Luc Blanchet. Next-to-next-to-leading order spinorbit effects in the gravitational wave flux and orbital phasing of compact binaries. *Class.Quant.Grav.*, 30:135009, 2013.

[118] Luc Blanchet, Alessandra Buonanno, and Guillaume Faye. Tail-induced spin-orbit effect in the gravitational radiation of compact binaries. *Phys.Rev.*, D84:064041, 2011.

[119] A. G. Wiseman. Coalescing binary systems of compact objects to (post)Newtonian**5/2 order. 4V: The Gravitational wave tail. *Phys.Rev.*, D48:4757–4770, 1993.

[120] Luc Blanchet, Guillaume Faye, Bala R. Iyer, and Benoit Joguet. Gravitational wave inspiral of compact binary systems to 7/2 postNewtonian order. *Phys.Rev.*, D65:061501, 2002.

[121] Guillaume Faye, Luc Blanchet, and Alessandra Buonanno. Higher-order spin effects in the dynamics of compact binaries. I. Equations of motion. *Phys.Rev.*, D74:104033, 2006.

[122] Etienne Racine, Alessandra Buonanno, and Lawrence E. Kidder. Recoil velocity at 2PN order for spinning black hole binaries. *Phys.Rev.*, D80:044010, 2009.

[123] I.W. Harry, A.H. Nitz, Duncan A. Brown, A. Lundgren, Evan Ochsner, et al. Investigating the effect of precession on searches for neutron-star-black-hole binaries with Advanced LIGO. *Phys.Rev.*, D89:024010, 2014.

[124] R.J.E. Smith, I. Mandel, and A. Vechhio. Studies of waveform requirements for intermediate mass-ratio coalescence searches with advanced detectors. *Phys.Rev.*, D88:044010, 2013.

[125] L A Wainstein and V D Zubakov. *Extraction of Signals from Noise*. Prentice-Hall, Englewood Cliffs, 1962.

[126] Alejandro Bohe, Sylvain Marsat, Guillaume Faye, and Luc Blanchet. Next-to-next-to-leading order spin-orbit effects in the near-zone metric and precession equations of compact binaries. *Class.Quant.Grav.*, 30:075017, 2013.

[127] Luc Blanchet, Alessandra Buonanno, and Guillaume Faye. Third post-Newtonian spin-orbit effect in the gravitational radiation flux of compact binaries. 2012.

[128] Thibault Damour, Bala R. Iyer, and B. S. Sathyaprakash. Comparison of search templates for gravitational waves from binary inspiral. *Phys. Rev. D*, 63(4):044023, 2001.

[129] J. Aasi et al. Parameter estimation for compact binary coalescence signals with the first generation gravitational-wave detector network. *Phys.Rev.*, D88:062001, 2013.

[130] Eric Poisson. Gravitational waves from inspiraling compact binaries: The Quadrupole moment term. *Phys.Rev.*, D57:5287–5290, 1998.

[131] Kip S. Thorne. Gravitational radiation. In S.W. Hawking and W. Israel, editors, *Three hundred years of gravitation*, pages 330–458. Cambridge University Press, 1987.

[132] Philippe Grandclement, Vassiliki Kalogera, and Alberto Vecchio. Searching for gravitational waves from the inspiral of precessing binary systems. I: Reduction of detection efficiency. *Phys. Rev.*, D67:042003, 2003.

[133] Philippe Grandclement and Vassiliki Kalogera. Searching for gravitational waves from the inspiral of precessing binary systems: New hierarchical scheme using 'spiky' templates. *Phys.Rev.*, D67:082002, 2003.

[134] Philippe Grandclement, Mia Ihm, Vassiliki Kalogera, and Krystof Belczynski. Searching for gravitational waves from the inspiral of precessing binary systems: Astrophysical expectations and detection efficiency of 'spiky' templates. *Phys.Rev.*, D69:102002, 2004.

[135] Yi Pan, Alessandra Buonanno, Yan-bei Chen, and Michele Vallisneri. A Physical template family for gravitational waves from precessing binaries of spinning

compact objects: Application to single spin binaries. *Phys.Rev.*, D69:104017, 2004.

[136] Alessandra Buonanno, Yan-bei Chen, Yi Pan, and Michele Vallisneri. A Quasi-physical family of gravity-wave templates for precessing binaries of spinning compact objects. 2. Application to double-spin precessing binaries. *Phys.Rev.*, D70:104003, 2004.

[137] Alessandra Buonanno, Yanbei Chen, Yi Pan, Hideyuki Tagoshi, and Michele Vallisneri. Detecting gravitational waves from precessing binaries of spinning compact objects. II. Search implementation for low-mass binaries. *Phys.Rev.*, D72:084027, 2005.

[138] Chris Van Den Broeck, Duncan A. Brown, Thomas Cokelaer, Ian Harry, Gareth Jones, et al. Template banks to search for compact binaries with spinning components in gravitational wave data. *Phys.Rev.*, D80:024009, 2009.

[139] Diego Fazi. *Development of a physical-template search for gravitational waves from spinning compact-object binaries with LIGO*. PhD thesis, Università di Bologna, 2009.

[140] I.W. Harry and S. Fairhurst. A coherent triggered search for single spin compact binary coalescences in gravitational wave data. *Class.Quant.Grav.*, 28:134008, 2011.

[141] P. Ajith, N. Fotopoulos, S. Privitera, A. Neunzert, and A.J. Weinstein. An effectual template bank for the detection of gravitational waves from inspiralling compact binaries with generic spins. 2012.

[142] A. Lundgren and R. O'Shaughnessy. A single-spin precessing gravitational wave in closed form. 2013.

[143] Matthew D. Duez. Numerical relativity confronts compact neutron star binaries: a review and status report. *Class.Quant.Grav.*, 27:114002, 2010.

[144] Masaru Shibata and Keisuke Taniguchi. Coalescence of Black Hole-Neutron Star Binaries. *Living Rev.Rel.*, 14:6, 2011.

[145] Francesco Pannarale. The Black Hole Remnant of Black Hole-Neutron Star Coalescing Binaries. 2012.

[146] Benjamin D. Lackey, Koutarou Kyutoku, Masaru Shibata, Patrick R. Brady, and John L. Friedman. Extracting equation of state parameters from black hole-neutron star mergers: aligned-spin black holes and a preliminary waveform model. 2013.

[147] Francois Foucart, Luisa Buchman, Matthew D. Duez, Michael Grudich, Lawrence E. Kidder, et al. First direct comparison of non-disrupting neutron star-black hole and binary black hole merger simulations. 2013.

[148] Emily Baird, Stephen Fairhurst, Mark Hannam, and Patricia Murphy. Degeneracy between mass and spin in black-hole-binary waveforms. *Phys.Rev.*, D87:024035, 2013.

[149] Drew Keppel, Andrew P. Lundgren, Benjamin J. Owen, and Hanyuan Zhu. Parameter space metric for 3.5 post-Newtonian gravitational-waves from compact binary inspirals. *Phys.Rev.*, D88:063002, 2013.

[150] J. Abadie et al. Search for gravitational waves from binary black hole inspiral, merger and ringdown. *Phys.Rev.*, D83:122005, 2011.

[151] J. Aasi et al. Search for Gravitational Waves from Binary Black Hole Inspiral, Merger and Ringdown in LIGO-Virgo Data from 2009-2010. *Phys.Rev.*, D87:022002, 2013.

[152] Stephen Privitera, Satyanarayan R.P. Mohapatra, Parameswaran Ajith, Kipp Cannon, Nickolas Fotopoulos, et al. Improving the sensitivity of a search for coalescing binary black holes with nonprecessing spins in gravitational wave data. *Phys.Rev.*, D89(2):024003, 2014.

[153] Tito Dal Canton, Alexander H. Nitz, Andrew P. Lundgren, Alex B. Nielsen, Duncan A. Brown, et al. Implementing a search for aligned-spin neutron star – black hole systems with advanced ground based gravitational wave detectors. *Phys.Rev.*, D90(8):082004, 2014.

[154] C.A.K. Robinson, B.S. Sathyaprakash, and Anand S. Sengupta. A Geometric algorithm for efficient coincident detection of gravitational waves. *Phys.Rev.*, D78:062002, 2008.

[155] Thomas Adams. Low latency search for compact binary coalescences using MBTA. 2015. Submitted to proceedings of Rencontres de Moriond 2015.

[156] Kipp Cannon, Romain Cariou, Adrian Chapman, Mireia Crispin-Ortuzar, Nickolas Fotopoulos, et al. Toward Early-Warning Detection of Gravitational Waves from Compact Binary Coalescence. *Astrophys.J.*, 748:136, 2012.

[157] Eric Jones, Travis Oliphant, Pearu Peterson, et al. SciPy: Open source scientific tools for Python, 2001–. [Online; accessed 2015-04-01].

[158] Markus Billeter, Ola Olsson, and Ulf Assarsson. Efficient stream compaction on wide SIMD many-core architectures. In *Proceedings of High Performance Graphics 2009*, pages 159–166, August 2009.

[159] John D. McCalpin. Memory bandwidth and machine balance in current high performance computers. *IEEE Computer Society Technical Committee on Computer Architecture (TCCA) Newsletter*, pages 19–25, December 1995.

[160] Intel Corporation. *Intel® 64 and IA-32 Architectures Optimization Reference Manual*. Number 248966-030. September 2014.

[161] Thibault Damour, Piotr Jaranowski, and Gerhard Schaefer. Dynamical invariants for general relativistic two-body systems at the third postNewtonian approximation. *Phys.Rev.*, D62:044024, 2000.

[162] Luc Blanchet and Guillaume Faye. Equations of motion of point particle binaries at the third postNewtonian order. *Phys.Lett.*, A271:58, 2000.

[163] Luc Blanchet, Bala R. Iyer, and Benoit Joguet. Gravitational waves from inspiralling compact binaries: Energy flux to third postNewtonian order. *Phys.Rev.*, D65:064005, 2002.

[164] Sylvain Marsat, Alejandro Bohe, Guillaume Faye, and Luc Blanchet. Next-to-next-to-leading order spin-orbit effects in the equations of motion of compact binary systems. *Class.Quant.Grav.*, 30:055007, 2013.

[165] William G. Laarakkers and Eric Poisson. Quadrupole moments of rotating neutron stars. *Astrophys.J.*, 512:282–287, 1999.

VITA

AUTHOR: Alexander Harvey Nitz
NATIONALITY: American
DATE OF BIRTH: December 10, 1987
DEGREES AWARDED:

- B.A., Physics, University of Michigan, 2010

PROFESSIONAL EMPLOYMENT:

Graduate Teaching/Research Assistant, Department of Physics, Syracuse University (2010-2015).

PUBLICATIONS:

- *Accuracy of gravitational waveform models for observing neutron-starblack-hole binaries in Advanced LIGO*, **Alexander H. Nitz**, Andrew Lundgren, Duncan A. Brown, Evan Ochsner, Drew Keppel, and Ian W. Harry, Phys. Rev. D 88, 124039 (2013)

- *Template banks to search for low-mass binary black holes in advanced gravitational-wave detectors*, Duncan A. Brown, Prayush Kumar, and **Alexander H. Nitz**, Phys. Rev. D 87, 082004 (2013)

- *Detecting binary neutron star systems with spin in advanced gravitational-wave detectors*, Duncan A. Brown, Ian Harry, Andrew Lundgren, and **Alexander H. Nitz**, Phys. Rev. D 86, 084017 (2012)

- *Investigating the effect of precession on searches for neutron-starblack-hole binaries with Advanced LIGO*, Ian W. Harry, **Alexander H. Nitz**, Duncan A. Brown, Andrew P. Lundgren, Evan Ochsner, and Drew Keppel
, Phys. Rev. D 89, 024010 (2014)

- *Implementing a search for aligned-spin neutron star-black hole systems with advanced ground based gravitational wave detectors*, Dal Canton, et al., Phys. Rev. D 90, 082004 (2014)

- *An improved pipeline to search for gravitational waves from compact binary coalescence*, Usman, et al., (2015)

AWARDS:

- 2015 Levinstein Fellowship for Outstanding Graduate Student
- Graduate Assistantship, Department of Physics, Syracuse University (2010-2015).
- Dean's Merit Scholarship, University of Michigan, USA (2006).

TEACHING:

- ASTRO 101 (Fall 2010/2011).

PRESENTATIONS:

- Searching for Gravitational Waves from Spinning Binary Neutron Star Sources, Eastern Gravity Meeting, Syracuse University, Nov 2012
- Faithfulness of Gravitational Wave Models for Spinning NSBH Sources, Eastern Gravity Meeting, University of Toronto, June 2013
- Constructing CBC Searches with PyCBC, LSC-Virgo Meeting, Stanford University, September 2014